HIGH-FREQUENCY ULTRASOUND BEAMFORMING FOR A MINIMALLY INVASIVE ENDOSCOPIC PROBE

By

Christopher Samson

Submitted in partial fulfillment of the requirements
for the degree of Doctor of Philosophy

at

Dalhousie University
Halifax, Nova Scotia
August, 2020

DEDICATION

This work is dedicated to my parents, Amédée & Edna, my sister, Stephanie, and Mémé and Pépé, Claire and Adelard. With each passing year, I discover new ways in which you have influenced who I am.

Thank you.

TABLE OF CONTENTS

iv

LIST OF TABLES

LIST OF FIGURES

ABSTRACT

Many surgeries are trending toward minimally-invasive procedures to reduce patient recovery times and produce fewer complications. These procedures are characterized by having small surgical openings, making it difficult to use medical imaging equipment not specifically designed to fit into small openings. Clinicians use laparoscopes or other optical microscopes as the primary tools for endoscopic surgeries, but these tools only provide imaging at the surface and lack depth-resolved information that would be of utmost value. Recently, a high-frequency endoscopic phased-array imaging probe has been developed which provides an unprecedented combination of depth-resolved imaging resolution with a minimally-invasive form factor (2.5 x 3.0 mm). This technology has the potential to provide enhanced image guidance capabilities to a wide array of surgical applications. To be suitable for medical imaging applications we developed a suitable electronic imaging system, commonly referred to as a beamformer, to support this imaging probe. This system was the world's first real-time beamformer for high-frequency phased array imaging and uses a newly developed variable sampling scheme termed the 'One Sample per Pixel' technique for image formation. This hardware and imaging technique generate high-quality ultrasonic images in real-time. We improved on the system's capabilities by implementing ultrafast imaging techniques that greatly increased the system's usefulness while simultaneously developing a new ultrafast imaging technique for sector imaging called sparse orthogonal diverging wave imaging (SODWI), which offers a variety of advantages over similar techniques. These capabilities were applied to functional ultrasound imaging in a preclinical setting where we were able to detect the neurological activation of auditory structures in rats, in particular, the inferior colliculus. This functional ultrasound experiment was performed through a 3.5 x 6.0 mm opening, which is smaller than any previous functional ultrasound experiments in the literature. Future directions for developing the system and new applications of these technologies are described.

LIST OF ABBREVIATIONS AND SYMBOLS USED

Abbreviation/Symbol	Description
α	Attenuation coefficient
α_o	Temperature-dependent attenuation coefficient
θ	Steering angle
θ_i	Incident angle
θ_r	Reflected angle
θ_t	Transmission angle
λ	Wavelength
$\xi(x,y)$	Spatially varying apodization function
ρ	Density
σ_w	Standard deviation
$\Phi(r,t)$	Scalar velocity potential
φ	Plane wave emission angle
Ψ	Field transfer function
$\%BW$	Percent bandwidth
a_f	Geometric focus of a concave transducer
CT	Computer tomography
c	Longitudinal speed of sound
C	Contrast
C_{MI}	Mechanical index unit conversion factor
DFT	Discrete Fourier transform
DNLL	Dorsal nucleus of the lateral lemniscus

Abbreviation/Symbol	Description
DOF	Depth of field
DWI	Diverging-wave imaging
d_i	Distance to the ith element
ESM	Electrocortical stimulation mapping
E	Doppler ensemble length
el_p	Element pitch
env	Beamformed envelope amplitude
fMRI	Functional magnetic resonance imaging
F	F-number
FPGA	Field programmable gate array
FSM	Finite state machine
f	Frequency
f_c	Center frequency
f_D	Doppler frequency
f_s	Sampling frequency
$FWHM_{con}$	Lateral full-width half maximum of a concave transducer
$FWHM_{lat}$	Lateral full-width half maximum
$g(t)$	Ultrasound pulse
$G(jw)$	Fourier transform of an ultrasound pulse
HMSTA	Hadamard encoded multi-element synthetic transmit aperture
$h(\boldsymbol{r},t)$	Spatial impulse response
H	Hadamard matrix
H_s	Sparse Hadamard matrix

Abbreviation/Symbol	Description
IC	Inferior colliculus
IEEE	Institute of electrical and electronic engineers
IP	Intellectual property
I-Q	In phase and quadrature phase
I	Identity matrix
$I(x,y)$	Power doppler signal
k	Tissue-dependent frequency attenuation coefficient
LSF	Line spread function
L	Length of the aperture
MLA	Multi-line acquisition
MRI	Magnetic resonance imaging
MSTA	Multi-element synthetic transmit aperture
MI	Mechanical index
n	Number of transmissions
n_{vp}	Number of virtual point sources
N	Number of elements in the array
N_{angles}	Number of plane wave angles
N_{CF}	Number of pulses per color flow sequence
N_{FZ}	Number of focal zones
N_{lines}	Number of lines per image
N_{UCD}	Number of pulses ultrafast compound doppler sequence
OCT	Optical coherence tomography
PC	Personal Computer
PET	Positron Emission Tomography

Abbreviation/Symbol	Description
PRF	Pulse repetition frequency
PRI	Pulse repetition interval
PSF	Point spread function
PWI	Plane-wave imaging
p-value	Probability value
p_i	Incident pressure
p_r	Reflected pressure
p_t	Transmitted pressure
p_-	Peak negative pressure
RSLL	Range sidelobe level
r	Radius
$\boldsymbol{r}$	Position in space
R	Hadamard encoded receive data
R_c	Reflection coefficient
R_d	Distance between a transducer and a position in space
r_p	Radius at pixel p
r_o	Position of a transducer element
R_s	Synthetic aperture receive data
SA	Synthetic aperture
SNR	Signal-to-noise ratio
SODWI	Sparse orthogonal diverging-wave imaging
STEDI	Synthetic transmit-element delay insertion
S	Transducer surface
S_i	Average signal energy inside a region of interest

Abbreviation/Symbol	Description
S_n	Average noise energy
S_o	Average signal energy outside a region of interest
S_{sig}	Average signal energy
TOF	Time-of-flight
t	Time
T	Transmit delay matrix
T_c	Transmission coefficient
T_d	Element delay
$T_{DW}(v,p,\theta)$	Transmit delays for diverging wave imaging
TI	Thermal index
T_{PRI}	Pulse repetition interval
$T_{PW}(x_f,z_f,\alpha)$	Transmit delays for plane wave transmission
$T_{RX}(n,p,\theta)$	Receive delays in polar coordinates
$T_{SA}(n,p,\theta)$	Transmit delays for synthetic aperture imaging
$T_T(n,p,r,\theta)$	Two-way time-of-flight delay
$T_{TXC}(n,f)$	Transmit delays for focused transmission in cartesian coordinates
$T_{TXP}(n,r,\theta)$	Transmit delays for focused transmission in polar coordinates
VGA	Variable-gain amplifier
v	Virtual point source
$v_n(x,y,0,t)$	Spatially varying normal particle velocity
$v_{no}(t)$	Electrically applied normal particle velocity
v_y	Projected velocity in the ultrasound beam

Abbreviation/Symbol	Description
w	Angular frequency
w_c	Angular center frequency
W_{deg}	Power required to increase a given tissue by 1°C
W_p	Attenuated output power
x	Lateral position
x_f	Lateral position of the focus
x_n	Lateral position of the nth element
x_v	Lateral position of the virtual point source
y	Longitudinal position
z	Depth position
Z	Characteristic acoustic impedance
z_f	Depth position of the focus
$z_F(x,y,t_i)$	Filtered and beamformed IQ data
$Z_F(x,y,w)$	Frequency spectrum of the filtered and beamformed IQ data
z_v	Depth position of the virtual point source

ACKNOWLEDGEMENTS

1 INTRODUCTION

In the sphere of medical imaging, ultrasound is considered one of the primary imaging modalities along with the likes of X-ray imaging, Computed Tomography (CT), Positron Emission Tomography (PET), Magnetic Resonance Imaging (MRI), and Optical Coherence Tomography (OCT). Each by their characteristics, exhibit strengths, and weaknesses. These strengths and weaknesses ultimately decide which applications use each imaging modality. Ultrasound imaging at conventional frequencies, between 3-10MHz, has resolution similar to that of MRI and CT, lower than OCT, and higher than X-Ray and PET. Ultrasound is also non-destructive (unless it's purposefully intended to be), giving it a clear advantage over imaging modalities using ionizing radiation such as X-ray, CT, and PET. MRI acquisitions can take seconds or minutes, whereas ultrasound frame acquisition rates can reach thousands of frames per second. Furthermore, MRI systems require controlled environments rendering them relatively unusable in the operating room. MRI systems are particularly difficult to access given limited hospital resources and excessive wait times. Given this limitation, other imaging modalities are preferred to MRI if the diagnostic outcomes are equivalent.

High-frequency ultrasound is a sub-category of ultrasound with increased resolution. Its operating frequency is an order of magnitude greater than conventional ultrasound frequencies, roughly 30-70 MHz, compared to 3-10 MHz for conventional frequencies, and therefore its resolution is also increased by an order of magnitude. The major trade-off between ultrasound and OCT is concerning resolution and depth of penetration. Due to optical absorption and scattering, OCT suffers from reduced penetration depth compared to ultrasound, but typically

exceeds the resolution of high-frequency ultrasound systems. The resolution and penetration depth trade-off decides which of the two modalities is more suitable for a given application. However, high-frequency ultrasound also has the advantage of array-based imaging transducers, which can provide a more uniform focus distributed throughout the image. High-frequency ultrasound's utility as an imaging modality is thus positioned for applications where: damaging tissue is undesirable, real-time frame rates are required, and the depth of penetration is larger than what can be attained with OCT.

1.1 Project Motivation

For the most part, the clinical use of high-frequency ultrasound has been small in comparison to other imaging modalities, and currently, most high-frequency ultrasound is focused on pre-clinical small animal imaging. The one exception to this is catheter-based intravascular ultrasound (IVUS), which has been widely adopted by interventional cardiologists. Apart from IVUS, the reason for limited clinical adoption is due to the relative newness of the modality. High-frequency ultrasound is still only a couple of decades old, and due to the complexity of the transducers and electronics, it has only just recently reached the point of clinical acceptability. These human applications are primarily limited to topical applications including the eyes [1]–[3] and skin [4]–[6] with again the one widely used application of intravascular imaging [7]–[9]. IVUS imaging catheters typically have poor resolution and/or suffer from poor SNR due to their limited number of elements and small size. The development of high-quality high-frequency array transducers dating back to the 1990s was critical to unlocking the potential of these new clinical applications

2

[10]–[21]. This disrupting technology replaced the previous generation of fixed focus transducers which had limited depth of field and frame rates. These were severely limited by the mechanical scanners needed to physically translate the transducers to construct an image.

The work in this dissertation makes use of a recently developed 64-channel high-frequency array transducer in an endoscopic form factor (2.5 mm x 3.0 mm) [10], [12]. This transducer has the potential to open new applications for high-frequency ultrasound, specifically, in guiding minimally invasive surgeries. In these types of surgeries, commercially available high-frequency probes are much too large and are prohibited from fitting down the surgical pathway.

The trend towards minimally invasive surgeries is powered by quicker patient recovery times and fewer complications. This shift in patient care requires that modern technology rise to meet its needs. Performing procedures through small incisions introduces a fundamental problem. The small opening combined with using a variety of tools through the opening drastically limits a surgeon's field of view, and often the tips of the probes are even out of sight. For endoscopic procedures such as those seen in the digestive tract, illuminated laparoscopes are used with much success as a guidance tool [22], [23]. This approach is perfectly suitable for conditions where surgeons are interested in what lies on the surface. When depth information beyond the surface becomes invaluable, low-resolution ultrasound is sometimes used as a guidance tool when conventional laparoscopic techniques are no longer sufficient. Many studies have reported the potential value that even low-resolution ultrasound can provide in guiding various surgical applications. These include but are not limited to: neurosurgery [24]–[26], testicular resections [27], breast cancer [28], [29], orthopedics [30], prostate cancer [31], and gastrointestinal surgeries [32]. However, if

3

the depth of penetration and resolution trade-off prevent an external ultrasound probe from being used, i.e. the size of the structures to be imaged are so small that the depth of penetration needed to reach that area is impossible, then a high-frequency endoscopic 'phased array' probe is the ideal solution. The endoscopic form factor allows it to be inserted through small incisions, and the 'phased array' design produces a field-of-view that is very large compared to the size of the probe. These types of applications are ideal for the high-frequency phased array endoscopes developed by Bezanson et al. [10], [12], and this probe is used throughout this dissertation.

To unlock this endoscopic probe's full potential a high-quality electronic beamforming platform is needed. High-frequency beamforming requires higher sampling rates and timing accuracy in comparison to conventional ultrasound frequencies. When this project had started, there was no off-the-shelf commercial system capable of supporting such an array. Research in this area was and is of paramount importance to maximize performance and enable the most cutting-edge imaging technologies for high-frequency endoscopic phased arrays. Developments in this area will increase the likelihood that the medical market will adopt high-frequency endoscopic ultrasound probes as a guidance tool for minimally invasive procedures. The primary motivation of this thesis was the development of a first-of-its-kind high-frequency electronic beamformer to support the previously developed high-resolution endoscope for the application of guided neurosurgery.

1.2 Research Objectives

The overarching goal of this dissertation was to develop a specialized beamforming platform for high-frequency phased array imaging and leverage the minimally invasive endoscopic probe for applications not possible for other existing probes. Three core studies were performed to meet this goal. The author is the primary contributor to these studies which are: development and evaluation of a 64-channel high-frequency phased array beamformer using a novel variable sampling technique, the evaluation of a new ultrafast imaging technique for phased array imaging, and detecting the auditory response in rats using functional ultrasound imaging of the brain through a minimally invasive burr hole.

1.2.1 Development and Evaluation of a 64-channel High-Frequency Phased Array Beamformer Using a Variable Sampling Technique

The objective of this study was to develop a beamforming platform capable of supporting real-time imaging for a 64-element high-frequency phased array while simultaneously evaluating a novel $3/4\lambda$ variable sampling technique. The hypothesis for this study was that the data capture rate, which is typically prohibitively high for high-frequency ultrasound imaging, could be substantially reduced by combining variable sampling concepts with a $3/4\lambda$ demodulation scheme. This approach was modeled and experimentally evaluated on a custom system designed specifically for this application.

1.2.2 Evaluation of a Novel Ultrafast Imaging Technique for High-Frequency Phased Arrays

This study evaluated the use of a novel Hadamard based encoding technique for ultrafast phased array imaging on the high-frequency phased array beamforming platform. The technique, named sparse orthogonal diverging wave imaging (SODWI), was developed with the hypothesis that Hadamard based encoding techniques could be used for phased array applications to extract synthetic aperture equivalent data by applying a diverging wave delay profile to the array elements to preserve directivity. This study also evaluated a second hypothesis that the aggravation of the grating lobe level from using larger affective apertures from sparse encoding could be reduced by using a new synthetic transmit element delay insertion (STEDI) technique. Both simulations and experimental data support these hypotheses, and it was also found that image quality can be improved using these techniques.

1.2.3 Detecting the Auditory Response in Rats Using Functional Ultrasound Imaging of the Brain Through a Minimally Invasive Burr Hole

This goal of this third study was to show that the combination of the minimally invasive endoscopic phased array, the high-frequency beamformer, and the newly developed ultrafast imaging implementations could be combined for minimally

invasive pre-clinical functional ultrasound investigations. The hypothesis was that the system could be used to detect functional brain activation in the inferior colliculus of anaesthetized rats in the presence of auditory stimuli. Early experimental results proved the feasibility of this approach with only needing a 3.5 × 6.0 mm craniotomy.

1.3 Document Structure

The objectives of this project were: to develop a 64-channel beamformer implementing a novel 'One Sample per Pixel' variable sampling technique (Chapter 3), to implement ultrafast imaging using novel emission schemes (Chapter 4), and demonstrate the feasibility of high-resolution ultrafast imaging for functional ultrasound imaging of the brain (Chapter 5).

Chapter 2 will provide a concise background pertinent to high-frequency ultrasound beamforming. This includes some history into the development of high-frequency transducers and transducer arrays, various beamforming concepts, imaging performance parameters, encoding methods, Doppler methods, and various high-frequency applications.

Chapter 3 will introduce the 'One Sample per Pixel' variable sampling technique and the 64-channel beamformer that was developed as a platform for its evaluation. Theoretical background for the sampling scheme is provided, the system design and architecture are explained in detail, and the experimental and simulated results are compared as well as a discussion of the results.

Chapter 4 is focused on the implementation of novel ultrafast imaging algorithms on the beamforming platform. It highlights the beamformer modifications

necessary to implement ultrafast imaging. The theoretical concepts used to optimize compounding performance are described. Experimental and simulated results are provided and discussed before future experiments are outlined.

Chapter 5 presents a preclinical functional ultrasound imaging study. The study leverages the ultrafast imaging capabilities used in Chapter 4 to detect the brain response of anaesthetized rodents to auditory stimuli.

Lastly, Chapter 6 summarizes the work in this document and discusses future directions of study. System improvements and modifications to the preclinical study are suggested. New applications for sparse orthogonal diverging wave imaging (SODWI) and the synthetic transmit element delay insertion (STEDI) techniques are proposed and preliminary data supporting some of these applications are provided. Next potential improvements and future directions for the functional study are detailed and closing remarks are provided.

1.4 Contributions

In study 1, I was responsible for designing the digital electronic system architecture for the 64-channel beamforming platform to support real-time high-frequency ultrasound imaging for phased array imaging. This was done in two phases: the first being a system that multiplexed 8 channels at a time, and the second was a fully parallel 64-channel beamforming platform. I wrote all the FPGA firmware for this system from scratch and was heavily involved in the Python software development for this project. I modeled the Field II impulse response simulations used in this work and performed the mathematical analysis of the impact of the

$3/4\lambda$ demodulation scheme implemented in this study. I performed all the system integration and conducted all the experimental work. This work was published as a conference proceeding at the International Ultrasonics Symposium 2015 in Taipei, Taiwan [33]. I was the first and presenting author for this work. This work was later expanded upon and published as a journal article [34], for which I was also the first author. This work also led to a patent and I am a co-inventor.

In study 2, I redesigned the system firmware to capture and output channel data and wrote a new Python interface for extracting and analyzing channel data from the beamforming platform developed in study 1. I wrote a library of MATLAB scripts and functions to implement a wide range of beamforming techniques related to ultrafast imaging for phased arrays and developed a new imaging technique presented herein named SODWI, as well as the synthetic transmit element delay insertion (STEDI) technique. I performed the theoretical and experimental work for this study. This work was first presented at the International Ultrasonics Symposium 2018 in Kobe, Japan [35]. I was the first and presenting author for this work. I subsequently expanded on this work and it was published in journal format where I was the first author [36]. This work was also patented, and I am a co-inventor.

In study 3, I made the necessary Python modifications needed to capture large Doppler ensembles used for functional ultrasound imaging. I designed the experimental system architecture that synchronized the auditory stimuli with the image acquisition. I developed the post-processing software used for Doppler processing and statistical analysis of the data. This work was presented at the International Ultrasonics Symposium 2019 in Glasgow, Scotland [37].

Despite not being presented throughout this dissertation, I contributed to many other research projects throughout this time. I implemented a hardware-based sign coherence grating lobe suppression techniques on the beamforming platform that was presented at the International Ultrasonics Symposium 2016 in Tours, France [38], I was the first and presenting author of this work. This work included major firmware changes to enable this technique to be applied in parallel with the variable sampling beamforming scheme discussed in Study 1 and required that I modify the software to apply the apodization.

The system and channel data firmware/software configuration have been used by many in the lab and as such, I have provided system support and custom configurations for a variety of applications. Most notably, I was heavily involved in the work by Katherine Latham related to 3D imaging using a crossed-electrode array based on electrostrictive material, where I developed much of the firmware necessary to support the beamforming strategies used in those studies. For this work, I was a supporting author for four conference proceedings to the International Ultrasonics Symposium from 2016-2019 [39]–[42] and was the presenting author for the work in 2017 [40]. This work was expanded upon and published in journal format for which I was also a supporting author [43]. This work also led to a patent and I am a co-inventor as I helped develop the idea of simultaneously compounding in both elevation and azimuthal planes. I similarly provided firmware, software, and field modeling support for a single-channel Hadamard encoded endoscope published as a conference proceeding at the International Ultrasonics Symposium 2019 in Glasgow, Scotland [44], for which I was a supporting author. Lastly, I provided firmware, system, and beamforming support for an FPGA based ultrafast beamformer which

was published as a conference proceeding at the International Ultrasonics Symposium 2019 in Glasgow, Scotland [45], for which I was a supporting author.

2 BACKGROUND

The following chapter will provide basic background knowledge relevant to high-frequency ultrasound imaging. The topics include the basic concepts for pulse-echo ultrasound imaging, transducer arrays, acoustic modeling, beamforming concepts, image quality, coded excitation, Doppler and its application to functional ultrasound, and high-frequency ultrasound applications.

2.1 Pulse-Echo Ultrasound Imaging: Reflection, Refraction, and Scattering

As compressional waves propagate through a medium, they are subjected to scattering, absorption, diffraction, and dispersion. Scattering is the key phenomenon that leads to pulse-echoes and ultimately, ultrasound imaging. At boundaries between different media, waves are transmitted and reflected at the boundary interface. The physics governing the properties of transmitted and reflected waves can be predicted by the angle and pressure of the incident wave as well as the characteristic acoustic impedance of the media surrounding the boundary. Fig 2.1 depicts a wavefront propagating towards a boundary between two mediums with different acoustic impedance, as well as the reflected, and transmitted, or refracted, pressure waves. Characteristic acoustic impedance, Z, is defined as a product of a material's density, ρ, and its speed of sound, c.

$$Z = \rho c \qquad\qquad (2.1)$$
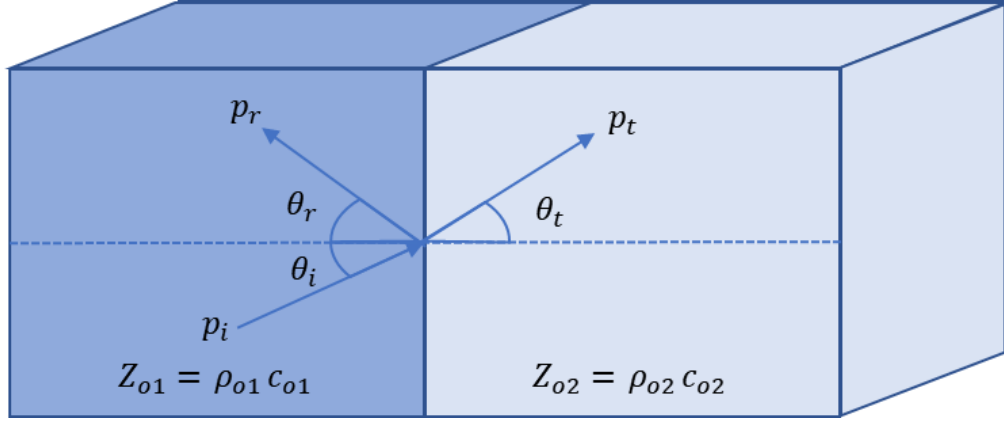
Fig 2.1 Transmission, p_t, and reflection, p_r, across a heterogeneous boundary of acoustic impedances, Z_{o1} and Z_{o2}, from an incident pressure wave, p_i.

The relationship between an incident plane wave reflected, and transmitted waves are governed by Snell's law, (2.2). The angles relating these wavefronts as well as the characteristic acoustic impedance of adjacent media can be used to calculate the reflection, (2.3), and transmission coefficients, (2.4). The reflection coefficients define the ratio of the reflected pressure 'p_r' relative to the incident pressure 'p_i' amplitude: $R_c = \frac{p_r}{p_i}$. The transmission coefficient defines the ratio of incident pressure to transmitted pressure 'p_t': $T_c = \frac{p_t}{p_i}$.

$$\frac{\sin \theta_i}{c_{o1}} = \frac{\sin \theta_r}{c_{o1}} = \frac{\sin \theta_t}{c_{o2}} \tag{2.2}$$

$$R_c = \frac{Z_{o2} \cos \theta_i - Z_{o1} \cos \theta_t}{Z_{o2} \cos \theta_i + Z_{o1} \cos \theta_t} \tag{2.3}$$

$$T_c = \frac{2Z_{o1} \cos \theta_i}{Z_{o2} \cos \theta_i + Z_{o1} \cos \theta_t} \tag{2.4}$$

Consider a simplified case where the incident wave, p_i, is normal to the acoustic boundary. The reflection and transmission coefficients simply to (2.5) and (2.6).

$$R = \frac{Z_{o2} - Z_{o1}}{Z_{o2} + Z_{o1}}$$

(2.5)

$$T = \frac{2Z_{o1}}{Z_{o2} + Z_{o1}}$$

(2.6)

This phenomenon is the basis for pulse-echo imaging. After transmitting a pressure wave into tissue, the receive echoes are recorded as shown in Fig 2.2. This illustration shows an ultrasound probe imaging a heterogeneous medium with 3 distinct homogeneous media, each having a different characteristic acoustic impedance. The receive echoes occur at the boundaries where the acoustic impedance changes. In this example, attenuation is ignored, as such, the intensity of the receive echoes is a product of the incident pressure and the two-way transmission and reflection coefficients. Envelope detection is performed on the receive echoes to provide an amplitude line (A-line), and this information is typically log compressed and mapped to grayscale to generate a brightness-mode line (B-mode). Combining adjacent B-mode lines produces a 2D or 3D B-mode image, which is the gold standard in ultrasound imaging.
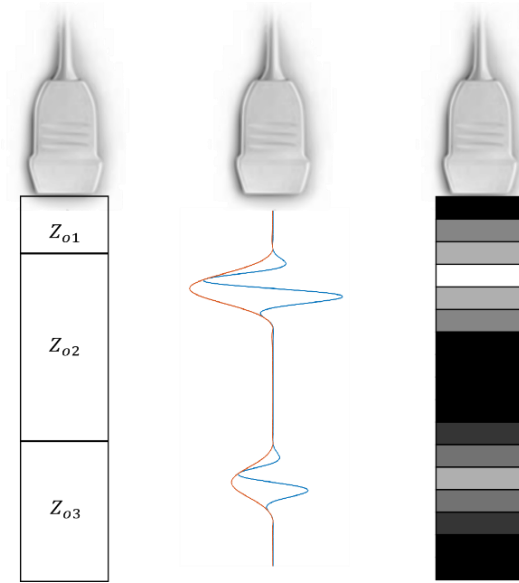
Fig 2.2 A simple heterogeneous medium with 3 homogeneous zones with characteristic acoustic impedances, Z_{o1}, Z_{o2}, and Z_{o3}. The receive echoes measured at the tranducers are plotted with the associated envelope. On the right, a B-mode grayscale mapping shows how the receive echoes are used to construct an image line.

In complex media such as tissue, boundaries are not always well defined as was shown in Fig 2.2, and scattering is the fundamental phenomenon needed to understand the receive dynamics for this complex media. Tissue consists of many scatterers per unit volume which can vary in acoustic impedance and density. The receive echoes from this common media, is the superposition of the interactions between the incident ultrasound wave and its interference with the scatterers within the beam's path. Scattering is categorized into three sub-types based on the scatterer size relative to the ultrasound wavelength: specular, diffractive, and diffusive. Specular scattering occurs when the size of the scatterers are much larger than a wavelength, such as large cysts. Diffusive scattering occurs when the scatterers are much smaller than a wavelength such as the background tissue matrix. Finally,

diffractive scattering is used to define the scatterers that fall between specular and diffusive scattering, such as small cysts. Under specular scattering, the effects of reflection and refraction are more pronounced since the acoustic impedances defining the boundary between the scattering cluster and the incident angle of the pressure wave play a larger role. This scattering phenomenon typically leads to undesired artefacts since the incident angle of the pressure wave can not always be normal to the scattering surface in practice. Diffusive scattering, where the wavelength is large relative to the scatterers, produces the opposite effect. The incident angle of the pressure wave relative to the scatterer is irrelevant and can be ignored. A diffusive scatterer emission after it is excited from an incident pressure wave will produce a point source emission characterized by a spherical wave being emitted from its location. Diffusive scattering is primarily used to model biological media and blood [46] since the tissue and blood aggregate is a superposition of cells that are much smaller than the ultrasound wavelength. Diffractive scattering falls between these two extremes where the interference of the incident wave with the primary and secondary side of the scatterer produce an interference pattern that is recorded.

2.2 Transducers and Arrays

The transducer is at the heart of any ultrasound system. It provides the necessary transduction from electrical to acoustic energy by exploiting the piezoelectric effect. In the presence of an electric field, a piezoelectric material will undergo strain. The reverse is also true, the stress-induced strain on a piezoelectric material will induce a proportional electric field across the substrate. These properties are essential for ultrasound imaging as the transducer is responsible for

delivering acoustic energy into tissue, as well as converting acoustic echoes into electrical energy, which is monitored by the system. This effect has been exploited for over 100 years beginning with sonar technology. Sonar was originally developed to detect submarines and was deployed as early as 1918 [47].

Piezoelectric transducers can be made from a single element or an array of elements. Single element transducers are typically curved or lensed to laterally focus the ultrasound beam. Acoustic reflections along the central axis of a focused transducer that are captured and converted to an electrical signal, are referred to as amplitude mode lines or A-scan lines. The lateral resolution is commonly defined as the full-width at half maximum ($FWHM_{con}$) of the acoustic beam. For a single element concave circular transducer, the $FWHM_{con}$, is defined by (2.7) where λ defines the wavelength, L defines the extent of the transducer aperture, and a_f defines the geometric focus of the transducer.

$$FWHM_{con} = 1.4\lambda\frac{a_f}{L} \qquad (\,2.7\,)$$

It is similarly useful to define the axial depth of field of a transducer, DOF. Using (2.8), the depth of field defines the 3 dB axial beam width for which the transducer provides good focusing and is a function of wavelength, λ, and f-number, F.

$$DOF = 7.2\lambda F^2 \qquad (\,2.8\,)$$

To create an image, several adjacent A-scan lines can be recorded and stitched together. The amplitudes are converted into grayscale values and mapped to a brightness level, referred to as a B-mode image. When using a single element transducer, the transducer is mechanically translated with a positioning or motor stage to capture adjacent A-scan lines which are used to construct a B-mode image as shown in Fig 2.3. Fig 2.3 also shows how array-based technology removes the need

for mechanical translation to capture 2-D images since the array can be electrically focused anywhere in front of the array. For 1D arrays, the imaging plane is commonly referred to as the azimuthal plane, and 2D arrays are capable of focusing on the azimuthal plane as well as the orthogonal elevation plane. 1D arrays typically rely on fixed acoustic lenses to provide elevation focusing. Array focusing is discussed in detail in the subsequent chapters.
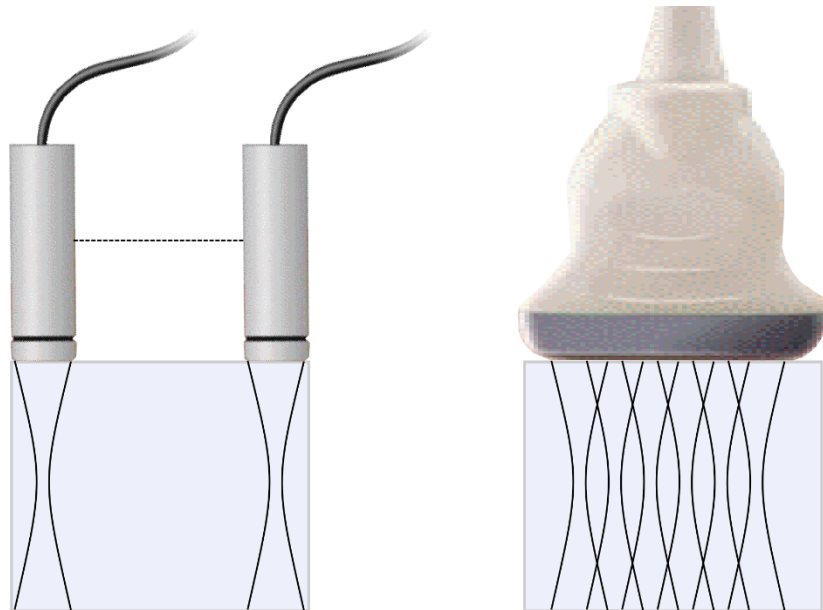
Fig 2.3 To create a 2-D B-mode image with a single element transducer, it must be mechanically translated to capture each image line making up the entire B-mode image. When array technology is used, sub-segments of the array can be used to spatially focus, translate, and even steer the ultrasound beam.

With array technologies, the superposition of the electromechanical responses from each element in the array can mimic a focused transducer if appropriate time delays are applied to the acoustic waves. Fig 2.4 illustrates how a geometrically focused transducer with a fixed focus can be mimicked using numerous smaller elements spatially separated along a curvature matched to the curvature of a focused

18

transducer. By exciting each of these elements of the array, the array will provide the same focusing as the geometrically focused transducer. In this case, the time delays are created by physically arranging the elements in a curved geometry. This notion can be modified slightly such that the elements in the array are arranged in a flat line, but the electrical excitation of each element is temporally delayed to produce the same focal point as the previous examples. To do so, the delays applied to each element, T_d, are calculated using (2.9) which simply divides the distance between the ith element and the focus, d_i, by the speed of sound in the medium, c. This concept allows for an electrically controllable focus and eliminates the trade off between depth-of-field and resolution for geometrically focused transducers predicted by (2.7) and (2.8). The acoustic beam can be electronically translated laterally across a long array aperture and focused to varying depths. In phased array transducers, the acoustic beam can be focused and steered out to wide angles that extend beyond the array aperture. The act of steering and focusing is referred to as beamforming, and is discussed in greater detail in chapter 2.4.

$$T_d = \frac{d_i}{c} \qquad\qquad (\,2.9\,)$$
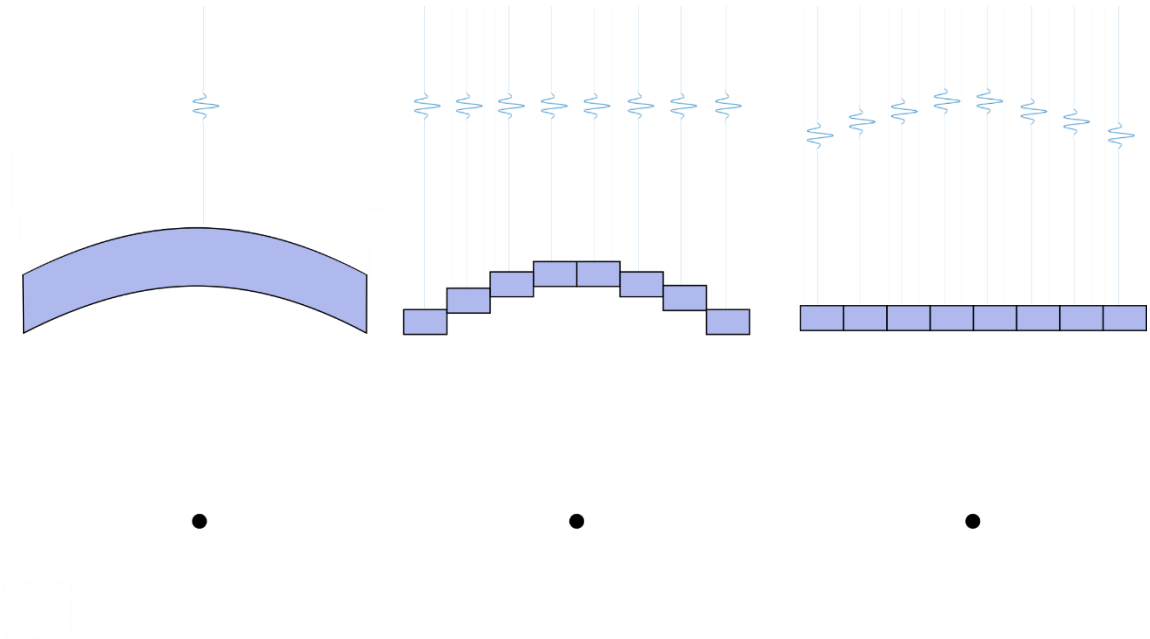
Fig 2.4 A curved transducer with a fixed focus can be approximated by using several smaller elements. Similarly, instead of placing the array element along a curvature, the elements can be electrically excited at different times instead of adjusting their positions.

2.3 Modeling Acoustic Fields with the Spatial-Impulse Response

Modeling acoustic fields is necessary for understanding pressure distributions from transducer excitation. The impulse response method is a common approach taken to calculate field distributions from several elements/transducer geometries, using various excitation waveforms, and beamforming strategies. To understand this methodology, the ability for any point in the field to move, or the scalar velocity potential, $\Phi(\boldsymbol{r}, t)$, must be related to the particle velocity at the surface of the transducer, v_n, as shown in (2.10). This equation was first presented by Lord Rayleigh in 1897 [48] and is known as the Rayleigh integral.

$$\Phi(\boldsymbol{r},t) = \frac{1}{2\pi} \iint_S \frac{v_n\left(t - \frac{|\boldsymbol{r} - r_o|}{c_o}\right)}{|\boldsymbol{r} - \boldsymbol{r_o}|} dS \qquad (2.10)$$

The field at position $\boldsymbol{r}$, can thus be calculated by integrating across the transducer surface, S, with r_o and c denoting the position of the transducer and the speed of sound in the medium. To convert the Rayleigh integral into a practical impulse response function, a few simple assumptions can be made. The transducer surface is assumed to be entirely located on a plane at $z = 0$, and the particle velocity at the surface, $v_n(x, y, 0, t)$, is the product of the normal particle velocity applied to the transducer via electromechanical coupling, $v_{no}(t)$, and a spatially-varying-apodization function, $\xi(x, y)$.

$$v_n(x, y, 0, t) = \xi(x, y)v_{no}(t) \qquad (2.11)$$

The normal particle velocity can be expanded as a convolution integral and substituted into (2.10) using $R_d = |\boldsymbol{r} - r_o|$ to yield (2.12).

$$\Phi(\boldsymbol{r},t) = \int_{-\infty}^{+\infty} v_{no}(\tau) \iint_S \frac{\xi(x,y)\delta\left(t - \frac{R_d}{c} - \tau\right)}{2\pi R_d} dS\, d\tau \qquad (2.12)$$

For convenience, the surface integral can be written as (2.13), which defines the spatial surface velocity apodization function in response to a Dirac-delta function, or spatial-impulse response. The closed-form spatial-impulse response function for many geometries have been solved including: rectangles [49], disks [50], concave surfaces [51], convex surfaces [52], and triangles [53].

$$h(\boldsymbol{r},t) = \iint_S \frac{\xi(x,y)\delta\left(t - \frac{R_d}{c}\right)}{2\pi R_d} dS \qquad (2.13)$$

In its most practical form, the pressure field can be modeled as (2.14), which is the convolution of the spatial-impulse response of the transducer surface with the temporally varying normal surface velocity.

$$\Phi(\boldsymbol{r}, t) = v_{no}(t) * h(\boldsymbol{r}, t) \qquad (\,2.14\,)$$

Using linear systems theory, the impulse response at a point in space can be calculated from the superposition of spatial impulse responses from each transducer element from an array of elements. The receive response from point reflectors in the field is equivalent to the spatial impulse response from the point reflector to the receiving element. Similarly, the receive echoes from all the point reflectors in the field are the superposition of each of the spatial impulse responses from each of the point reflectors to the receive element. The transmit and receive responses can be combined to model a two-way impulse response by convolving the excitation waveform with the electromechanical response of the transmit aperture, the spatial impulse response of the transmit aperture, the spatial impulse response of the receive aperture, and the electromechanical response of the receive aperture. This method has been described in detail by Stepanishen [54] and was later repeated by Jensen [55], which led to the development of the widely used Field II software for field calculations [46]. This flexible approach, which is regularly used in the ultrasound research community, enables rapid calculation of complex acoustic fields, and is used throughout this dissertation.

2.4 Ultrasound Beamforming

A key step in ultrasound imaging is focusing the ultrasonic beam. Referred to as beamforming, the primary concept is to coherently overlap ultrasonic signals onto or from a point in space so that the reflected signal energy from this focusing point, is significantly stronger than signals from other points in the field. Similarly, the echoes received can be delayed to selectively focus on a point in space. The beamforming process can, therefore, be broadly separated into two subprocesses: transmit and receive beamforming. In this chapter other key concepts are presented, including apodization and ultrafast imaging techniques.

2.4.1 Transmit Beamforming

Focusing on a point in space is easily understood when analyzing transmit beamforming. For transducer arrays, focusing the ultrasound beam to any point in space in front of the transducer requires that group delays be applied to the individual transducer elements to compensate for differences in the times-of-flight (TOF) between the array elements and the spatial focus, see Fig 2.6. By doing so, the signals from each element constructively interfere at a focus. This process is repeated multiple times per line to extend the depth of field (i.e. focal zones). The process is then repeated across a suitable number of adjacent image lines until the desired field of view has been insonified. The TOF delays can be calculated with (2.15) when using cartesian coordinates, or (2.16) when using polar coordinates.

$$T_{TXC}(n,f) = \frac{1}{c}\sqrt{\left(x_n - x_f\right)^2 + \left(z_f\right)^2} \qquad (\,2.15\,)$$

$$T_{TXP}(n,r,\theta) = \frac{1}{c}\sqrt{(x_n - r\sin\theta)^2 + (r\cos\theta)^2} \qquad (\text{ 2.16 })$$

For linear arrays, the acoustic beam emitted from the aperture is perpendicular to the array aperture, whereas for phased arrays the acoustic beam is steered at various angles away from the array aperture. For linear arrays, the image window is rectangular because the acoustic beam emitted from the array is perpendicular to the aperture. To beamform adjacent lines, the active sub-aperture is translated along the extent of the array as shown in Fig 2.5. Given this imaging scheme, it is convenient to use the cartesian coordinate system use in (2.15). In (2.15), the TOF for element n is calculated using the speed of sound in the medium, c, the lateral position of the array element, x_n, and the lateral and depth position of the focal point, x_f and z_f. Alternatively the polar coordinates used in (2.16) appropriately suit the sector-image window created with phased arrays, as shown in Fig 2.6. Using polar coordinates, the focal position coordinates are defined using a focal depth at radius, r, and steering angle, θ. As this thesis is focused on phased-array imaging, polar coordinates will primarily be used from this point on. One of the primary differences between the construction of linear and phased arrays is that linear arrays are typically much larger so that a large field of view is collected, whereas phased arrays achieve a large field of view from a smaller aperture by steering the beam to wide angles. The element pitch is different for linear and phased arrays. Linear arrays typically use λ pitch spacing whereas phased arrays commonly use $\lambda/2$ pitch. This difference in element pitch is chosen because the angle of grating lobe artifacts, which degrade image quality, is a function of steering angle and element pitch. As such, the element spacing for phased array applications is smaller. Grating lobes are described in more detail in section 2.5.3.
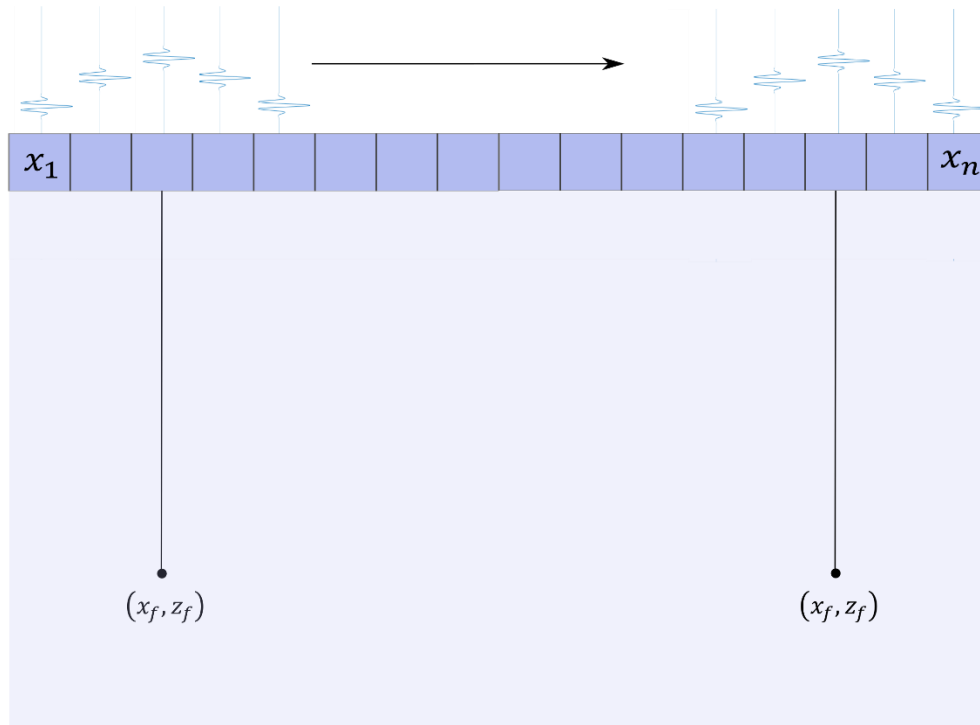
Fig 2.5 Transmit beamforming for a linear array. Transmit focusing to the point (x_f, z_f) from an array of elements using a sub-aperture of the array. Images are formed by translating the active sub-aperture along the extent of the array.
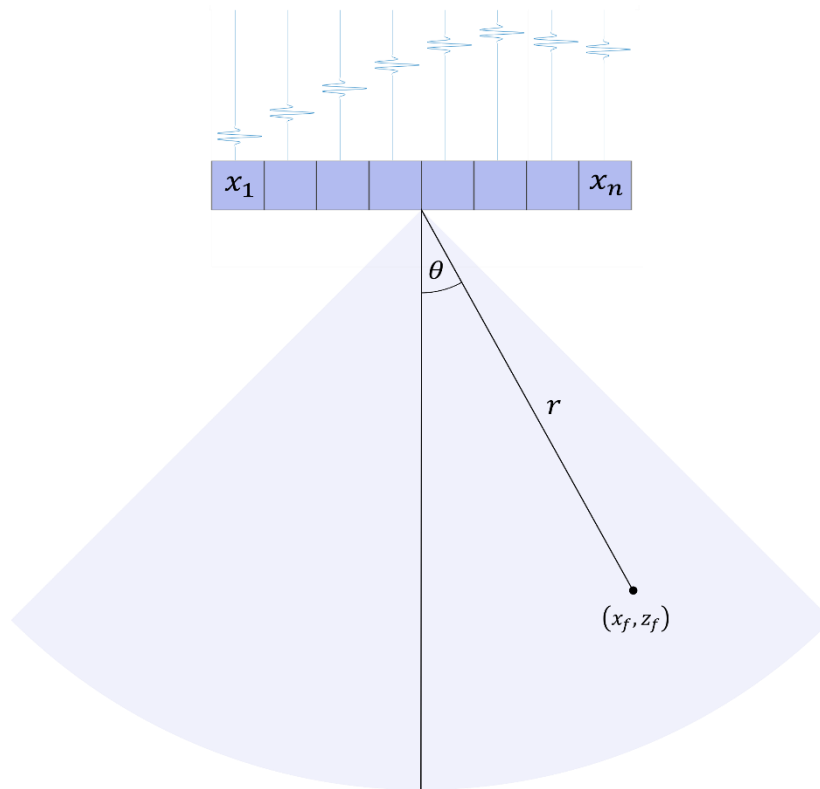
Fig 2.6 Transmit beamforming for a phased array generates a sector shaped image. Transmit focusing to the point (x_f, z_f) from an array of elements is typically calculated using polar coordinates (r, θ).

A single transmit focus has a limited depth of field. The depth of field is measured as the range of imaging depths at which the pressure is within 3 dB of the peak transmitted pressure for that focal zone. A simulation using a 64-element 30 MHz phased array with an aperture width of 3.5 mm is used to illustrate this trade-off. This array is focused to various f-numbers (1.0, 1.5… 4.0), where f-number $= \frac{depth}{aperture}$, and the one-way pressure distribution as a function of depth is plotted in Fig 2.7 (a). For lower f-numbers, the depth of field is shorter than higher f-numbers. By transmit beamforming to various focal positions, the image quality can be improved across a wider range of depths as shown in Fig 2.7 (b) where the focal positions from Fig 2.7 (a) are spliced together, providing a much better focus than

any single transmit focus alone. Due to the shallow depth of field when focusing to low f-numbers such as 1.0, these low f-numbers are seldomly used in practice.
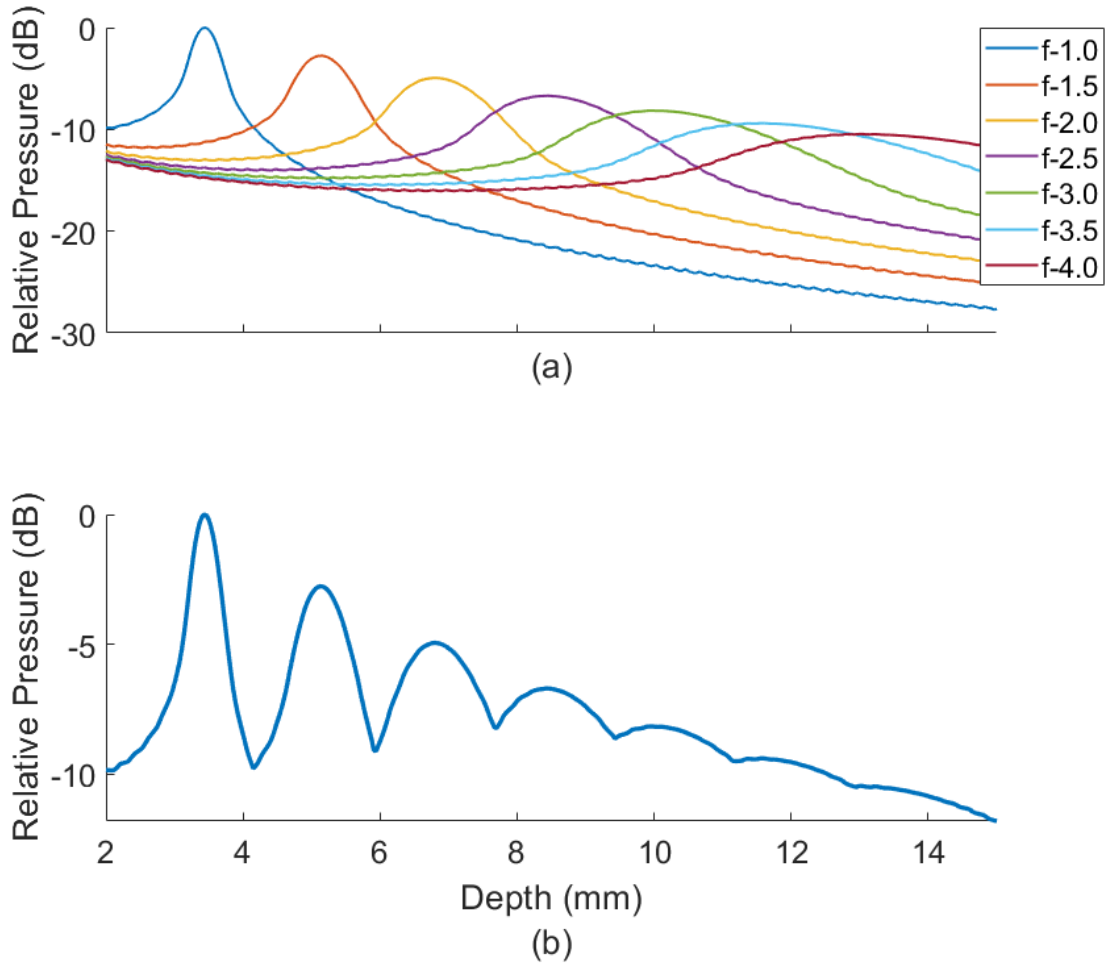
Fig 2.7 One-way signal pressure when transmitting to various focal zone positions (f-number = 1.0, 1.5 … 4.0) along an image line is shown in (a). The signal from a multi-focus line whereby the individual focal zones are spliced together to create an optimal focus is plotted in (b) showing the improvements in transmit pressure and improved overall depth of field.

2.4.2 Receive Beamforming

Once the array elements are pulsed for a given focal zone and image line, energy from the propagating beam begins to reflect from scatterers in the medium, sending receive echoes that have spherical wavefronts back to the transducer array. Focusing on reception requires that for each transmission, the receive echoes be dynamically focused (i.e. focal point changes) to every point along the image line of interest. In polar coordinates, the return TOF delays, $T_{RX}(n, p, \theta)$, are calculated using (2.17) from each radial position, r_p, at steering angle θ, and back to any element position, x_n, for the given speed of sound in the medium, c. Pulse echoes from a reflector are modeled as a spherical wave. This is shown in Fig 2.8, whereby the beam traces from the reflector to the array elements are shown. Normally hundreds of radial positions per line are used to ensure that the pixel spacing in a beamformed image appropriately captures the axial resolution of the imaging system. Spacing the pixels by half of the axial resolution is adequate.

$$T_{RX}(n, p, \theta) = \frac{1}{c}\sqrt{\left(x_n - r_p \sin\theta\right)^2 + \left(r_p \cos\theta\right)^2} \qquad (\,2.17\,)$$

Two-way TOF is calculated by summing the transmit and receive beamforming delays, as shown in (2.18).

$$T_T(n, p, r, \theta) = T_{RX}(n, p, \theta) + T_{RX}(n, r, \theta) \qquad (\,2.18\,)$$
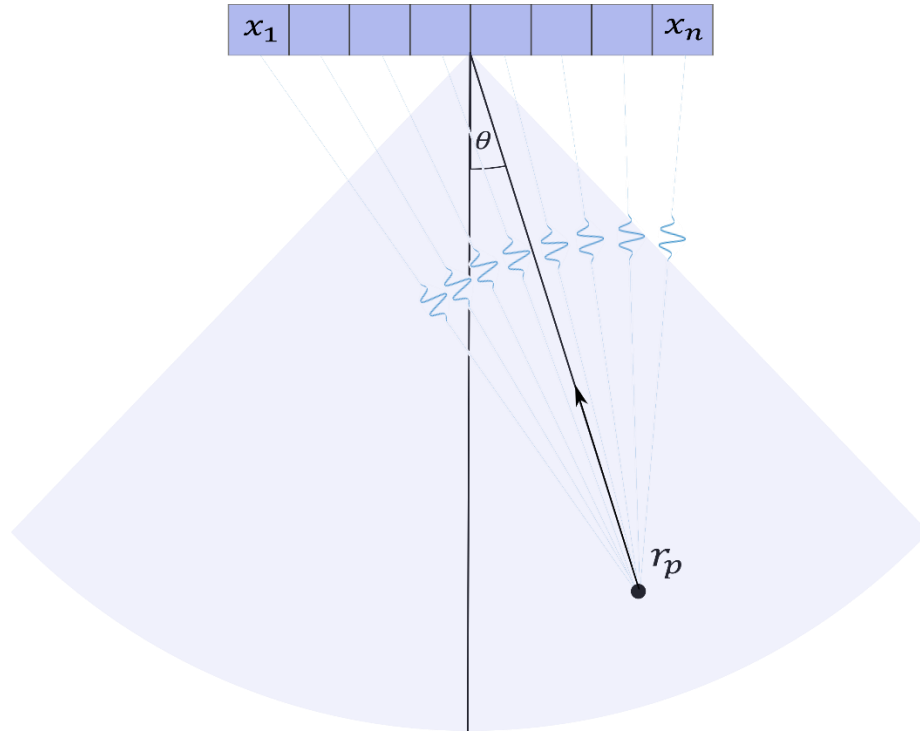
Fig 2.8 Receive beamforming for a sector image. Receive focusing must compensate for the difference in TOF from a point of interest in the field of view, (r_p, θ), back to the array elements.

2.4.3 Apodization

Apodization is the act of applying aperture weights to both the transmit and receive apertures. Apodization can lower sidelobes and improve the depth of field at the expense of the mainlobe width and SNR [56]. Sidelobes are characterized by the level of signal energy located adjacent to the main ultrasonic beam. Many weighting functions have been studied including, but not limited to, Chebyshev polynomials [57], Blackman-Harris window [58], least-squares fitting [59], Hamming windows [58], and Hanning windows [58]. In recent works, more sophisticated adaptive apodization techniques such as minimum-variance beamforming [60], and coherence weighting [61]–[63] have been developed.

The improved depth of field can be seen by comparing Fig 2.9 to Fig 2.7. Fig 2.9 shows an improved depth of field at shallower focal depths of that presented in Fig 2.7. In this example the 64-element 30 MHz simulations were repeated using a constant f-number of 2.5 instead of f-1.0, f-1.5, and f-2.0. This was achieved by expanding the aperture as the focal point moves away from the array, keeping the f-number constant until the full aperture is used, at which point the f-number begins to increase.
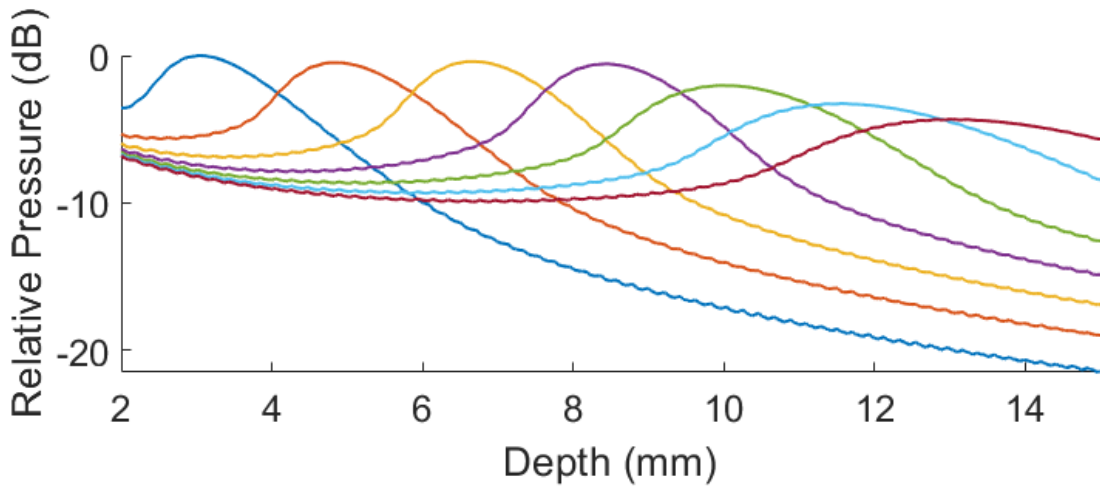
Fig 2.9 One-way signal pressure when transmitting to various focal zone positions using a constant f-number of 2.5, followed by f-3.0, f-3.5, and f-4.0.

2.4.4 Ultrafast Imaging

Ultrafast imaging is a relatively new method of ultrasound imaging that has certain advantages over conventional line-by-line focused imaging. As the name suggests, ultrafast imaging is an imaging technique that has very fast frame rates as compared to line-by-line imaging. This has allowed for new complementary imaging

30

modes where frame rates >1000 fps are required to be implemented. Some of these modes can resolve various phenomena such as shear wave propagation for elastography [64]–[66], precision blood volume changes for functional imaging [67]–[76], and propagation of individual contrast bubbles for super-resolution imaging [77]–[79]. The measurement and analysis of these waves and signals offer clinically significant insight into the physiology of tissue that cannot be obtained from conventional B-mode images. Ultrafast imaging techniques such as plane-wave imaging, diverging-wave imaging, and synthetic-aperture imaging, transmit unfocused ultrasound waves into a medium. These emissions weakly insonify the entire field-of-view, allowing images to be created from a single emission. This contrasts with conventional B-mode imaging methods implementing transmit focusing techniques, typically requiring 100s of insonifications to create a complete B-mode image dataset. As one would expect, a single emission from an ultrafast imaging technique will not yield the same quality image as the transmit focusing case.

To improve image quality, a transmit focus is generated synthetically by coherently compounding multiple unfocused insonifications, whereby successive insonifications are effectively emitted from distinct positions or orientations. There are three main methods for generating the unfocused wavefronts: plane-wave imaging, diverging-wave imaging, and synthetic-aperture imaging.

2.4.4.1 Plane-Wave Imaging

For plane-wave imaging, the emission angle, φ, is adjusted with each insonification, as shown in Fig 2.10 (a) [80]. With this approach there is no true

31

transmit focusing but rather a transmit focus is synthetically generated on the received data sets. Following the illustration from Fig 2.10, the 3 wavefronts presented can be temporarily delayed on receive such that the receive data from each emission constructively interfere at any location in the field of view, (x_f, z_f). The transmit delay from any plane wave to any position, (x_f, z_f), can be calculated using (2.19). Each emitted plane wave has a distinct interference pattern from the point scatterers in the field of view when focusing on any given point, as shown in Fig 2.10 (b) and (c), which highlights the aligned wavefronts when realigned to focus different positions in the field of view. When plane waves are compounded, they produce constructive interference at the focus, and interference from point scatterers outside of the focus is noncoherent and thus suppressed relative to the focus.

$$T_{PW}(x_f, z_f, \varphi) = \frac{1}{c}(z_f \cos\varphi + x_f \sin\varphi) \qquad (\,2.19\,)$$
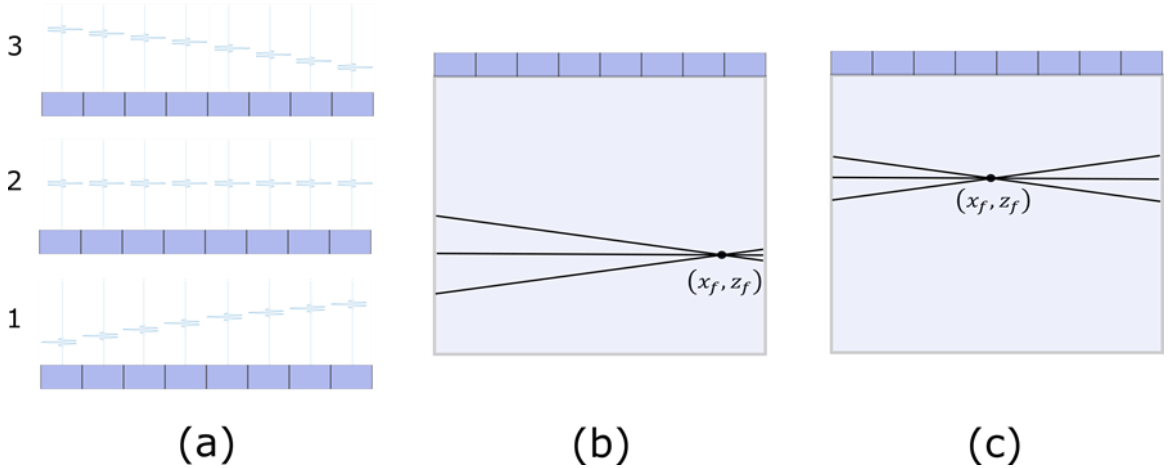
Fig 2.10 Plane-wave imaging whereby 3 tilted plane waves are used. Focusing to any point in the field of view, (x_f, z_f), is achieved by providing the appropriate delay corresponding to the plane-wave inclination angle to each of the emitted plane waves (a) to any position in the field of view, as shown in (b) and (c).

2.4.4.2 Diverging-Wave Imaging

For phased arrays that steer the ultrasound beam to wide angles, diverging waves are preferred over plane waves due to their ability to distribute energy beyond the extent of the aperture. In diverging-wave imaging, virtual point sources are synthetically created behind the array aperture with the corresponding transmit delays applied to the elements as shown in Fig 2.11. As a result, the wavefront emitted from the aperture is now spherical instead of planar in the azimuth plane. Using (2.20) the transmit delays from each virtual point source, v, to any point in space, (r_p, θ), can be calculated. Several diverging wave techniques have recently been developed. Some techniques adjust the lateral position of the virtual point source and the size of the transmit aperture [81], whereas some techniques utilize the full aperture and adjust both the lateral and depth position of each virtual point source [82]–[85]. By adjusting the position of the virtual point source, each wavefront insonifies the medium from a different point of view with various angular spectra. The receive-beamformed frames from each of these transmits can then be coherently compounded together to synthetically improve the transmit focus. Since the transmit delays are different for every transmit event, the spherical nature of the transmitted waves allows the compounded waves from each transmission to be coherently summed together at any focus in the field of view while simultaneously suppressing sidelobes since the constructive interference only occurs at the focus, as shown in Fig 2.11.

$$T_{DW}(v, p, \theta) = \frac{1}{c}\sqrt{\left(x_v - r_p \sin\theta\right)^2 + \left(z_v - r_p \cos\theta\right)^2} \qquad (2.20)$$
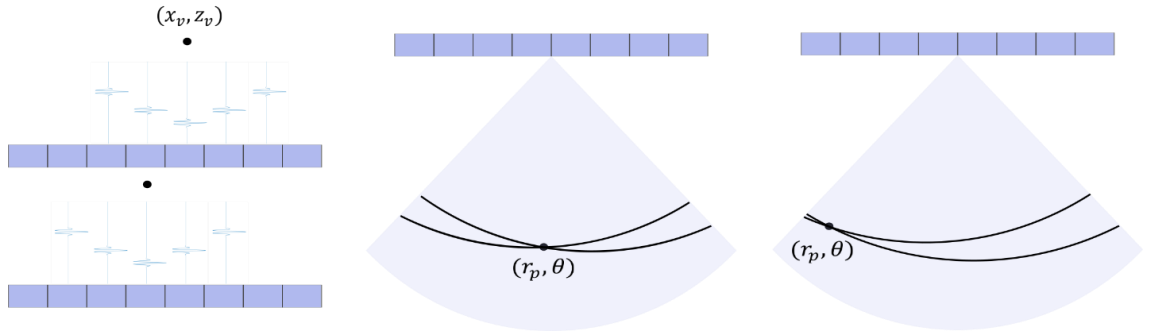
Fig 2.11 Diverging wave imaging with coherent compounding from various virtual point sources.

2.4.4.3 Synthetic-Aperture Imaging

Synthetic-aperture techniques pulse each element individually on transmit and receive data from the full aperture (all elements), as shown in Fig 2.12. Like the previously described approaches, the spherical waves emitted from each element excite the field of view from a different origin and with different angular spectra, which, when compounded together, improve transmit focusing and image quality. Each element, at position x_e in the aperture, is excited individually or the array elements can be sparsely excited to approximate the point spread function of the array [86]. The transmit delay from each transmitted pulse to any point in the field, (r_p, θ), can be calculated using (2.21). By sparsely exciting elements from the array, frame rates can be increased at the expense of SNR, a property common to all ultrafast imaging techniques. To deliver more energy into tissue while using fewer pulses than there are elements in the aperture, multi-element synthetic transmit aperture techniques have been investigated in the literature whereby several elements

are excited simultaneously, this improves SNR but the elements become effectively larger, which negatively affects lateral resolution and directivity [87], [88].

$$T_{SA}(n, p, \theta) = \frac{1}{c}\sqrt{\left(x_n - r_p \sin\theta\right)^2 + \left(r_p \cos\theta\right)^2} \qquad (\ 2.21\ )$$
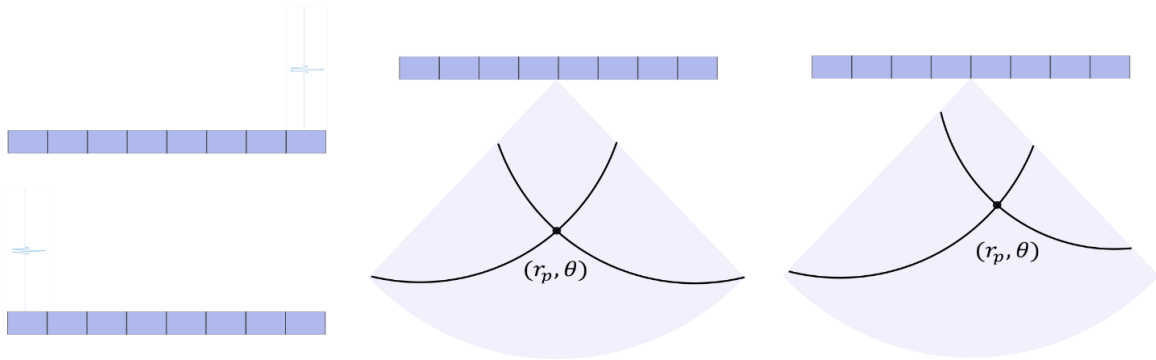
Fig 2.12 Synthetic transmit aperture beamforming. On the left, the transmission from each element on the extent of the array is shown. The emitted wavefronts from each element can be coherently compounded together for each position in space by adjusting the beamformed delay for each respective element.

2.5 Quantifying Image Quality

For high-resolution medical imaging, image quality is of paramount importance. For phased-array ultrasound, the primary metrics for evaluating and predicting overall image quality are point spread functions, resolution, grating lobes, contrast, and signal-to-noise ratio.

2.5.1 Point Spread Functions

Point spread functions are useful for characterizing a variety of imaging metrics including resolution, and dynamic range. They can be measured experimentally, but in the design phase are used to evaluate beamforming strategies and array performance. Point spread functions are modeled by estimating the field response when point targets are sparsely placed in the field of view, or when a single point target is in the field of view, in response to some array excitation. The receive echoes are simulated and images can be reconstructed using an appropriate beamforming strategy for the transmit and receive beamforming scheme applied to the array. Fig 2.13 (a) shows the 2-D point spread function of a single point target placed 6 mm directly in front of a 40 MHz 64 element array with $\lambda/2$ element spacing modeled using Field II. Fig 2.13 (a) is plotted with 70 dB of dynamic range and illustrates the extent to which the signal from the point target spreads both axially and laterally into the imaging field of view. This spreading of energy limits the useable dynamic range of the system. If a weak reflector is situated adjacent to a strong point reflector and produces a receive echo below the overlapping portion of the point spread function from the strong reflector, it will be buried in the energy spread from the stronger reflector, concealing it in the image. The sidelobes are faintly visible in Fig 2.13 (a) but are clearly visible in Fig 2.13 (c). They are characterized by the off-axis energy and are the limiting factor for useable dynamic range in the absence of system noise. Sidelobes also play an important role in contrast, as sidelobes from soft tissue or other reflectors spread into adjacent anechoic voids, or more weakly reflective tissue.
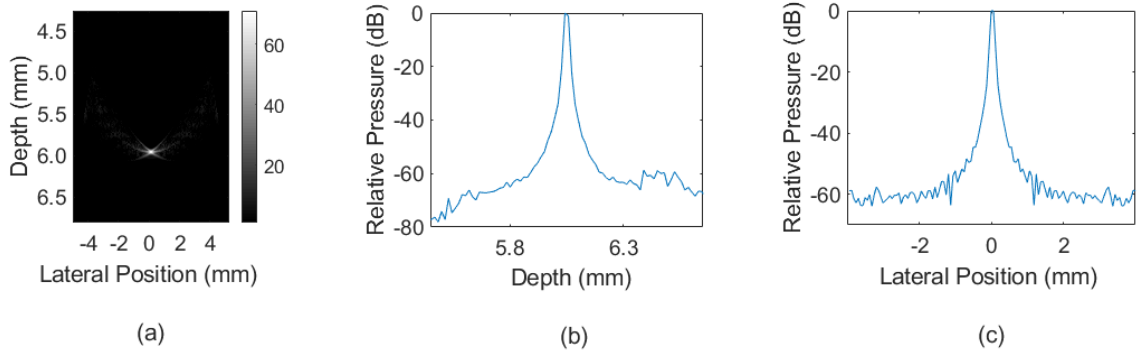
Fig 2.13 (a) 2D point spread function of a single point target. (b) and (c) are the axial and lateral projection of the 2D point spread function from (a).

Lateral and axial resolution are accurately modeled with the lateral and axial projections of point spread functions, as shown in Fig 2.13 (b) and (c) respectively. Analyzing these curves determines the effectiveness of any beamforming strategy with regards to resolution. For a two-way point spread function, the axial and lateral resolutions are objectively quantified by calculating the full-width half maximum (-6 dB point) of these field profiles.

2.5.2 Spatial Resolution

Spatial resolution defines an imaging system's ability to discern neighboring scatterers in space. For pulse-echo imaging, axial resolution is limited by the duration of the excitation pulse, which is dependent on the number of cycles used during excitation, the center frequency, and transducer bandwidth (electromechanical response). As the spacing between scatterers decreases, the temporal length of the excitation pulse propagating through the medium must be sufficiently short so that

37

the reflected echoes from these scatterers be distinguished. Axial resolution is generally measured as the FWHM of the axial projection of the point spread function. Similarly, the lateral resolution is typically defined as the $FWHM_{lat}$ of the lateral projection of a point spread function from a point target. The modeling from [56] has shown that the lateral resolution in the far-field can be calculated using (2.22), where L is the extent of the aperture, and z is the focal depth. The size of the transducer aperture plays a large role in lateral resolution. Larger transducer apertures allow for tighter focusing and hence better lateral resolution. It is also convenient, and common practice, to represent the ratio of the transducer focal depth and array aperture as the F#, where $F\# = z/L$.

$$FWHM_{lat} = 1.206\lambda z/L \qquad\qquad (\ 2.22\ )$$

2.5.3 Grating Lobes

Beam steering and focusing transducer arrays create regions of coherent off-axis interference called 'grating lobes'. These occur at symmetric locations around the main lobe. The grating lobe position is defined by the periodic and geometric nature of the array. Their existence is related to the periodic inter-element spacing and is analogous to undersampling time-varying signals. To completely avoid grating lobes in a full field of view spanning $\pm\pi/2$, when focusing normal to the array, the inter-element spacing must be less than or equal to 1λ of the shortest wavelength in the transmitted pulse bandwidth [89]. For phased arrays that steer and focus away from the central axis, the inter-element spacing must be sub-wavelength to avoid grating lobes in the same field of view. In conventional phased arrays, the range of steering angles is limited to approximately $\pm\pi/4$ or less. Under these conditions, the inter-

element spacing is set to be approximately $\lambda/2$ of the center frequency. Fig 2.14 shows the effects of spatially undersampling reflected pulse echoes from a point target. The element spacing in this simulated data is λ and the point target is positioned at 30°, which produces a very pronounced grating lobe. Fig 2.14 (a) shows how strong the artifact can be in the image, and (b) shows the lateral field profile to help quantify the signal level of the grating lobe (~40 dB). This is an extremely undesirable feature for medical imaging as it severely limits the system's dynamic range. To remove the grating lobe artifacts from being visible in the image, it would need to be plotted with only 40 dB of dynamic range, whereas if smaller element spacing were used, the dynamic the image could have over 60 dB dynamic range. A larger dynamic range in the image allows for better tissue contrast or differentiation of neighboring tissues and structures. When a system is vulnerable to grating lobe artifacts, strong scatterers can produce grating lobe signals of higher energy than the tissue that is in focus. To address this issue, several signal processing methods of grating lobe suppression have been developed [38], [62], [90]–[92].
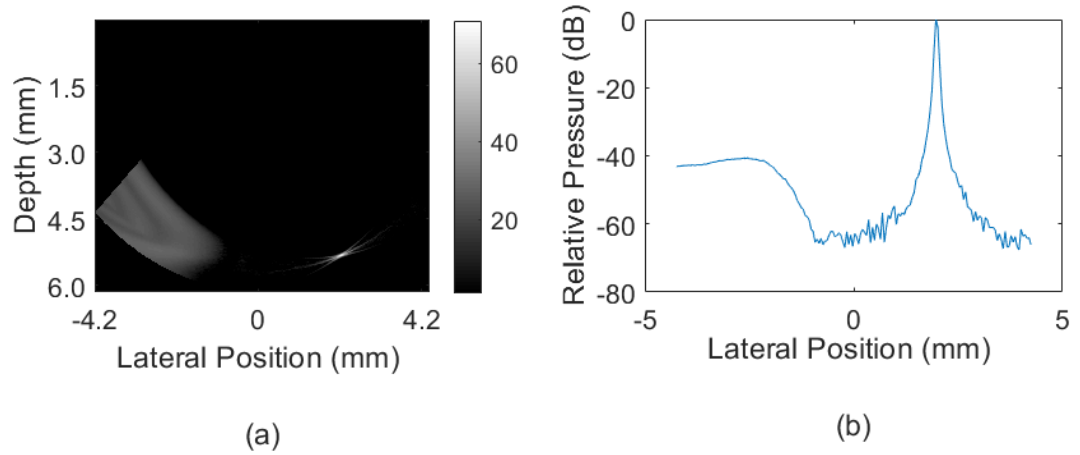
Fig 2.14 (a) a point spread function of a point target placed at a 30° steering angle from a λ pitch imaging array. (b) the lateral projection of the point spread function highlights the dynamic range loss due to the grating lobe.

2.5.4 Contrast

The ability to differentiate neighboring tissue of different scattering intensity is important for visualizing physiologically different tissue in ultrasound images. It can be calculated using (2.23) where S_i is the average signal energy inside a region of interest, and S_o is the average signal energy outside of the region of interest of equal size.

$$C = \frac{S_i}{S_o}$$

(2.23)

The contrast between tissue and anechoic voids are also of significant importance as it is a measure of sidelobe energy that appears in the anechoic void from neighboring tissue. In an ideal situation, the sidelobe levels would be below the noise floor of the system and would therefore not insert any measurable signal energy into the anechoic regions, rendering them black in the image. Fig 2.15 (a) is an

example of good contrast in a simulated tissue phantom where the sidelobe energy from adjacent tissue does not corrupt the anechoic void centered in the image. The difference in signal energy from the anechoic voids and the surrounding scatterers is significant and is quantified more clearly in Fig 2.15 (b). The anechoic voids are characterized by a significant drop in signal energy in these regions.
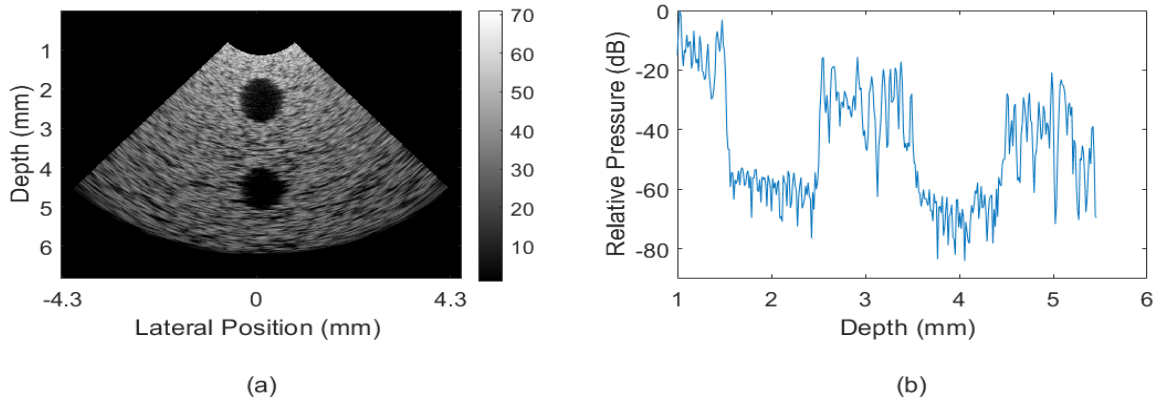
Fig 2.15 A simulated ultrasound image of a homogenous media with two anechoic voids embedded. (a) shows the 2D image and (b) shows the central image line plotted as a function of depth.

2.5.5 Signal-to-Noise Ratio

A system's signal-to-noise ratio (SNR) is calculated from (2.24) where S_{sig} denotes the receive signal voltage, and S_n denotes the RMS noise level. System noise is heavily dependent on the transducer and cable shielding, preamplifier performance, and other methods of electrical noise rejection.

$$SNR = 20 \log_{10} \frac{S_{sig}}{S_n} \qquad (2.24)$$

Receive signal strength is dependent on a multitude of factors including transmit pulse amplitude, beamformer performance, electromechanical coupling, and tissue

attenuation. The gains from increasing the transmit pulse amplitude are obvious, stronger incident waves will produce larger pulse echoes. Beamforming provides an electrically focused profile, providing an antenna gain at the focal spot, thereby increasing signal pressure at the focus, and through iteratively repositioning the focus in the field of view, SNR across the entire field of view can be improved. Lastly, SNR is heavily dependent on signal attenuation, α, which decreases the receive signal amplitude for point scatterers at depth in the image. Furthermore, attenuation is frequency dependent and higher frequencies exhibit higher rates of attenuation. (2.25) approximately describes the frequency dependency of the attenuation constant, where α_o is a temperature-dependent coefficient with units, dB/(cm · MHz), and k is a tissue-dependent coefficient typically ranging between 1-2 [93]. Due to this frequency-dependent penalty, high-frequency transducers will yield lower SNR than low-frequency analogs at the same depth within the tissue.

$$\alpha = \alpha_o f^k \qquad\qquad (2.25)$$

2.6 Coded Excitation

Safety guidelines limit the peak negative pressure and time-averaged power delivered to tissue from diagnostic imaging systems. Peak negative pressure is limited to prevent harmful cavitation effects, and limiting the time-average power prevents thermal damage. Medical systems must adhere to the mechanical index and thermal index requirements [94]. The mechanical index is defined by (2.26) where p_- defines the peak negative pressure in the media in MPa, frequency, f, is defined in MHz and C_{MI} is 1.0MPa/MHz$^{1/2}$. Health Canada guidelines set an upper limit of 1.9 for the MI [95] for most tissues.

$$MI = \frac{p_-}{C_{MI}\sqrt{f}} \qquad\qquad (2.26)$$

Similarly, Health Canada guidelines suggest that for most diagnostic B-mode imaging systems, limiting the thermal index to below 1.0 presents no risk of thermal damage, including pregnant mothers [95]. Other applications where bones are within 1cm of the transducer, such as for transcranial imaging, other restrictions apply. Calculating the thermal index can be done using (2.27) from [94], where W_p is the attenuated output power and W_{deg} is the power required to increase the tissue of interest by 1°C.

$$TI = \frac{W_p}{W_{deg}} \qquad\qquad (2.27)$$

In most cases, the mechanical index is the limiting factor for diagnostic imaging systems. It limits the transmit voltage that can be applied to the transducers, ultimately limiting the peak ultrasonic signal that can be delivered into tissue, and subsequently received at the transducer. Since the receive signal is limited by the MI, SNR and penetration depth can no longer be increased by simply increasing the transmitted signal pressure. To circumvent this limitation, much research has been done to increase SNR without the need for higher output pressure. Coded transmission systems have been broadly used to address this by coding the pulse phase or frequency without necessarily decreasing pulse bandwidth (axial resolution). Coding can be done across a single transmit event, or coding/decoding can be performed across several transmits. In short, increasing the total energy delivered into tissue without increasing the transmitted pressure, increases the signal level that can be retrieved on reception. The following sub-chapters describe common methods of coded excitation.

43

2.6.1 Single Transmit Coding

To increase the signal energy delivered into tissue without increasing the peak signal pressure, longer pulse durations are used. The simplest approach would be to increase the number of cycles transmitted into the media, as shown in Fig 2.16 (a). This simple approach will increase SNR at the expense of axial resolution. The receive signal from this waveform is then typically decoded using a matched filter, which produces the highest receive SNR. The matched filter output for a simple multi-cycle waveform is shown in Fig 2.16 (d). The most obvious drawback to this output is that it will exhibit very poor axial resolution since the duration of the filter output is quite long. Appropriately selecting a coded waveform with desirable autocorrelation properties elegantly solves this problem. Take for example Fig 2.16 (b), where a frequency chirp is transmitted into a media. The output from its matched filter, Fig 2.16 (e), produces much better axial resolution in comparison to the multi-cycle example. A downside to this approach is that it produces strong range sidelobe levels (RSLL). RSLL is characterized by the ratio between the main lobe and the sidelobes for coded excitations. The ripple found at the output of the matched filter from Fig 2.16 (e) corrupts the sidelobe levels and negatively affects imaging performance [96]. An optimal code will thus have an autocorrelation function with both high resolution, and low RSLL. Fig 2.16 (c) and (f) show a chirp weighted with a Hanning window and the output of its matched filter. In this case, the resolution is not as high as the non-weighted chirp, but the autocorrelation energy is almost completely confined at the main pulse, which results in improved RSLL compared to a non-weighted chirp.
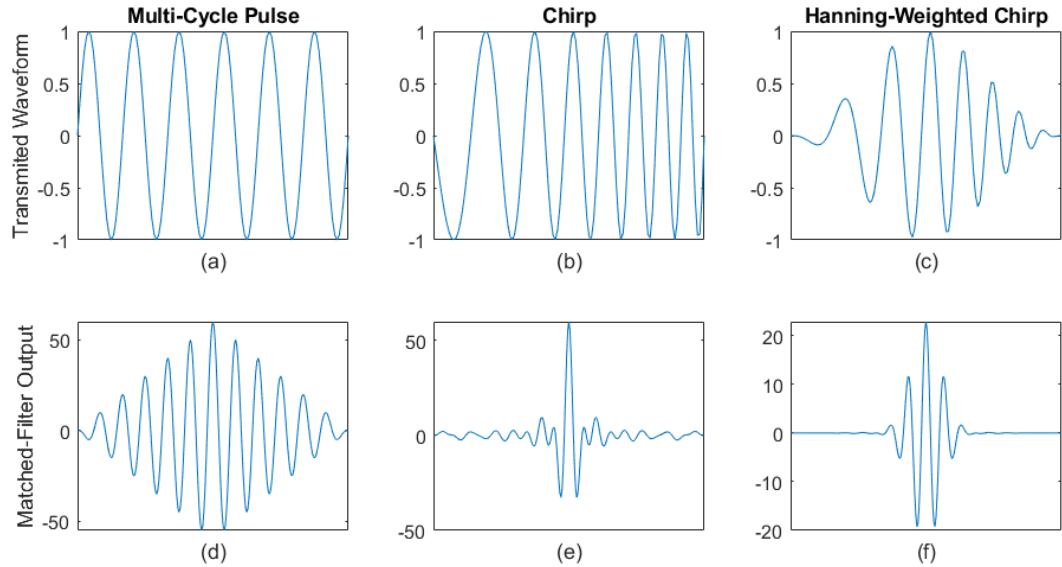
Fig 2.16 Coded excitation for a multi-cycle pulse (a), chirped excitation (b), and a Hanning-weighted chirp (c). (d)-(f) shown their associated matched filter outputs.

Optimizing the performance of a coded excitation imaging system requires a careful tradeoff between SNR, axial resolution, and RSLLs. As such, this field has been rigorously explored in the literature. For chirp excitations, Gaussian and cosine weighted chirps have been shown to produce -100dB RSLL [97] and work from Missaridis et al. have shown that the use of mismatched filters, which had first been developed in radar literature, produces -86dB RSLL performance and are insensitive to distortions from the transducer impulse response [98]. Barker codes have also been used extensively. Barker codes are biphasic codes where the polarity of the pulses in the multi-cycle excitation are coded with a ±1 symbol. Similarly to chirps, biphasic codes produce low autocorrelation RRSL and Barker codes have been shown to produce the lowest RRSL of all biphasic codes for a single transmit event [99].

2.6.2 Multi-Transmit Coding

Coding across multiple transmit events allows for excellent cancellation of range sidelobes. Golay codes produce better SNR gain per pulse length than chirps but are more sensitive to non-linear effects and motion [96]. Golay codes with two transmits are biphasic codes with symbols of ± 1 satisfying the complimentary condition from (2.28) where $A = (a(1), \dots a(n))$ and $B = (b(1), \dots b(n))$, define the complimentary codes [100]. Since two transmit codes are required for Golay coding, the system frame rate is reduced by a factor of two.

$$a(n)a(-n) + b(n)b(-n) = 2N\delta(n) \qquad (\text{ 2.28 })$$

Another popular method of coding ultrasonic signals is Hadamard coding. Hadamard matrices are symmetrical with an $n \times n$ shape where n is typically a power of two. Each row in the matrix is an orthogonal Hadamard code. Similarly, to the Golay and Barker codes, a Hadamard code or basis is a vector of ± 1 symbols. This coding scheme, therefore, encodes transmitted waves with $\pm 90°$ phase shifts. It allows for multiple waves to be in the field of view simultaneously, which can then be subsequently separated after decoding. Instead of convolving the receive data with the appropriate matched filter, as is the case for chirps, Barker codes, and Golay codes, Hadamard encoded data is decoded by multiplying the receive vectors by the transpose of the original Hadamard matrix. The transpose is closely related to the inverse of the Hadamard matrix such that $HH^T = nI$, where I is the identity matrix. Therefore, Hadamard encoding produces a signal gain of n and an SNR gain of $\sqrt{n}$. Concerning ultrasound imaging, the application of Hadamard encoding has been broadly used in two categories: spatially encoding wavefronts emitted from an array [101]–[103], and temporally encoding wavefronts from individual elements or sub-

apertures [35], [43], [104], [105]. Fig 2.17 (a) shows two plane waves sequentially emitted from an aperture with each wavefront's phase encoded according to a row of a Hadamard matrix. The wavefront from the next insonification contains the second orthogonal Hadamard code. Decoding the receive data from this emission provides two datasets representative of having emitted each of the angled plane waves individually with a signal gain of two. Alternatively, the illustration from Fig 2.17 (b) encodes the individual pulses emitted from each element from the array. By pulsing the elements with the phases from each row of a 4x4 Hadamard matrix, the data collected from the array can be decoded to produce datasets representative of having pulsed each element individually, identical to a synthetic aperture approach, only with a signal gain of four. The use of Hadamard codes and the encoding and decoding process is described thoroughly in Chapter 4.
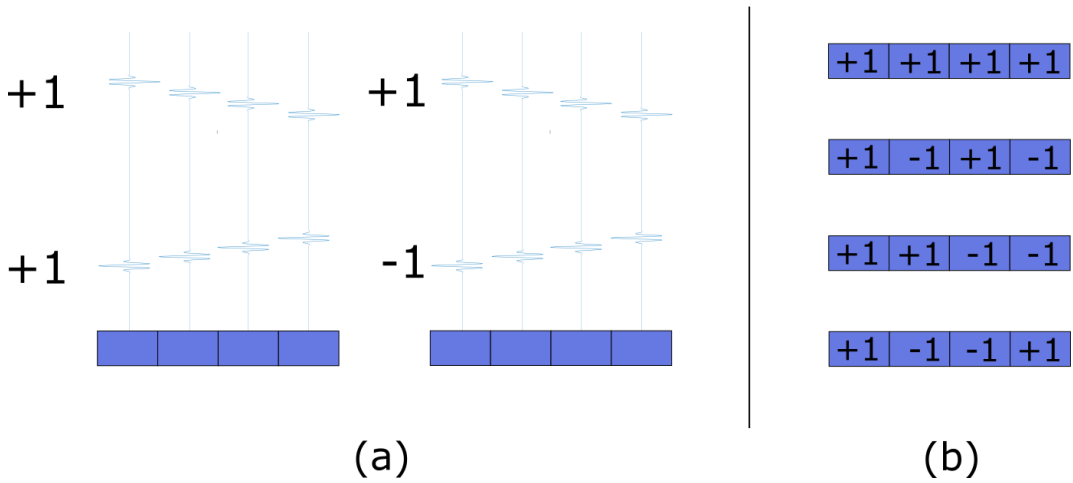
Fig 2.17 Multiplane-wave imaging (a) and Hadamard encoding array elements (b).

2.7 Blood Flow and Functional Ultrasound

Measuring blood flow is central to Chapter 5 where functional ultrasound is used to monitor neural activation in rodents. This experiment uses Doppler measurements as a surrogate for blood volume, which is then correlated with stimuli to identify functionally active neurological tissue. This section covers the historical progression of Doppler ultrasound up to the state-of-the-art techniques used today. The most recent developments in this area have dramatically improved its effectiveness, enabling new applications such as functional ultrasound imaging of the brain. Details on tissue clutter filtering and functional ultrasound imaging are also provided.

2.7.1 Doppler

Historically, characterizing blood flow and the cardiac cycle has been a key area of ultrasound research. Continuous-wave Doppler experiments were reported as early as 1957 by Satomura [106]. When ultrasound waves are incident on a moving object or particles, there is an inherent frequency shift in the detectable signal proportional to the velocity of the moving object. This phenomenon, otherwise known as the Doppler effect has been exploited to characterize blood velocities in most ultrasound systems. The Doppler frequency, f_D, is characterized by (2.29) where f_c is the excitation frequency, v_y is the projected velocity in the beam, and c is the longitudinal speed of sound.

$$f_D = 2f_c \frac{v_y}{c} \qquad (\ 2.29\ )$$

The examination region for continuous wave Doppler is limited to the region of overlap between the transmit and receive beams. For many applications, it is desirable to adjust the Doppler focus so that it coincides with a blood vessel or artery of interest. Electronic focusing was a natural step forward in estimating blood velocities which coincided with the development of electronically steerable array-based technologies. Coined pulse wave Doppler, pulses of finite length are repeatedly directed to a focal region. Unlike continuous wave Doppler, pulsed wave Doppler incorporates changes in echo arrival times to calculate velocity. The change in arrival time from (2.30) is proportional to the change in distance travelled, Δz, which can be related to the projected velocity inside the ultrasonic beam.

$$t_d = \frac{2\Delta z}{c} = \frac{2T_{PRI}v_y}{c} \qquad (2.30)$$

The next breakthrough for ultrasonic blood flow imaging was the development of color flow imaging. Color flow imaging measures blood velocity over a large area as opposed to using a single focal zone location like continuous and pulsed-wave Doppler. In clinical systems, it is common to interleave the Doppler mode with a high-quality B-mode scan. This limits the time allocated for Doppler or color flow processing, which means that for color flow imaging, tracking blood velocity over a much larger area limits the number of samples that can be acquired at any given location so that systems can operate in real-time. Instead of having hundreds of samples per location, as can be the case for pulsed-wave Doppler, color flow imaging will have between 3-12 tracking pulses per focal region/steering angle or line. FFT based frequency shift estimators, therefore, became much less reliable since the frequency resolution of the FFT is very low with so few samples. The development of phase-based frequency estimators and time-domain based cross-correlation

methods were therefore of paramount importance for color flow imaging as they removed the necessity of FFT algorithms from blood velocity estimation [107], [108].

The most recent technical development which has benefitted ultrasonic blood velocity estimation is ultrafast imaging. By using plane-wave imaging or diverging-wave imaging it is possible to capture high-quality B-mode images with only a few insonifications in comparison to conventional B-mode imaging techniques. Furthermore, reducing the number of compounded frames can further increase frame rates by sacrificing image quality [80]. Frame rates can therefore be selected to optimize image quality for collecting blood flow data throughout the entire field of view. Bercoff et al. were the first to report and quantify the advantages of ultrafast compound Doppler [109]. Fig 2.18 helps illustrate the temporal advantage of ultrafast compound Doppler over conventional color flow imaging methods. In Fig 2.18 a) a color flow pulse sequence is shown where the number of pulses (N_{CF}), defined by (2.31), are spread across the number of lines (N_{lines}) examined in the field of view, the number of focal zones (N_{FZ}), and the ensemble length, E.

$$N_{CF} = N_{lines} \cdot N_{FZ} \cdot E \qquad\qquad (\,2.31\,)$$

For the ultrafast compound Doppler method shown in Fig 2.18 b), the number of pulses needed (N_{UCD}) are defined by (2.32) and is only spread across the ensemble length and the number of compounded plane wave angles (N_{angles}). Note that other ultrafast imaging techniques such as diverging wave imaging and synthetic aperture are also possible.

$$N_{UCD} = N_{angles} \cdot E \qquad\qquad (\,2.32\,)$$

50
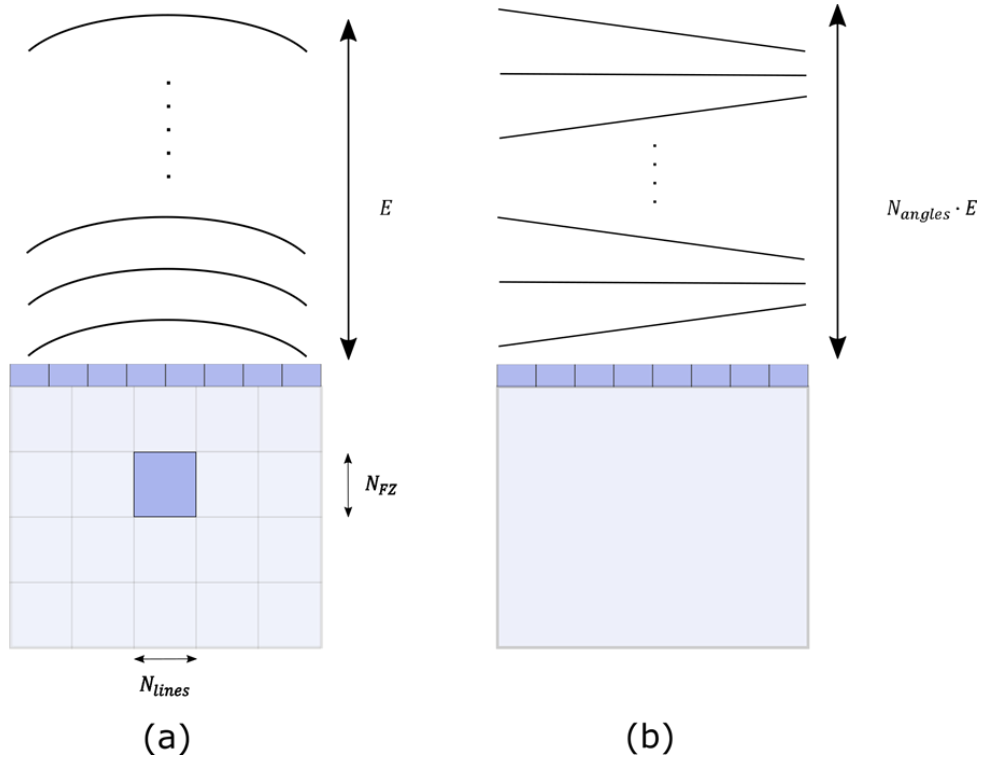
Fig 2.18 a) color flow pulse sequence shown for a single line and focal zone, this sequence is repeated across the necessary blocks in the grid to produce a color flow image of an area of interest. b) an ultrafast compound Doppler pulse sequence whereby a series of tilted plane waves are compounded together to insonify the entire field of view at once.

The overall number of insonifications necessary for ultrafast compound Doppler methods will therefore be much lower than for color flow imaging. This spare time is used to acquire additional samples that improve sensitivity and reduce the variance in blood flow estimates. For example, using the same acquisition time, Bercoff et al. were able to capture 176 frames using ultrafast compound Doppler, whereas an ensemble length of only 11 could be captured using color flow. The blood images for both methods are shown in Fig 2.19 a) and b) with the ultrafast compound Doppler image having 14 times less variance [109]. The improvement in the blood flow image is striking and even when acquisition time is reduced by a factor of 2, 4, 8 and 14 as

is the case in Fig 2.19 c) through f), the variance between blood estimates is still noticeably improved for the ultrafast compound Doppler method over the conventional focused color flow case. Furthermore, ultrafast compound Doppler can capture blood flow for the full field of view simultaneously, whereas, for color flow, the acquisition is slow enough that blood flow measurements from different areas of the image are acquired during different portions of the cardiac cycle. This can also lead to velocity measurement variability since blood velocity is not constant across the entire cardiac cycle.
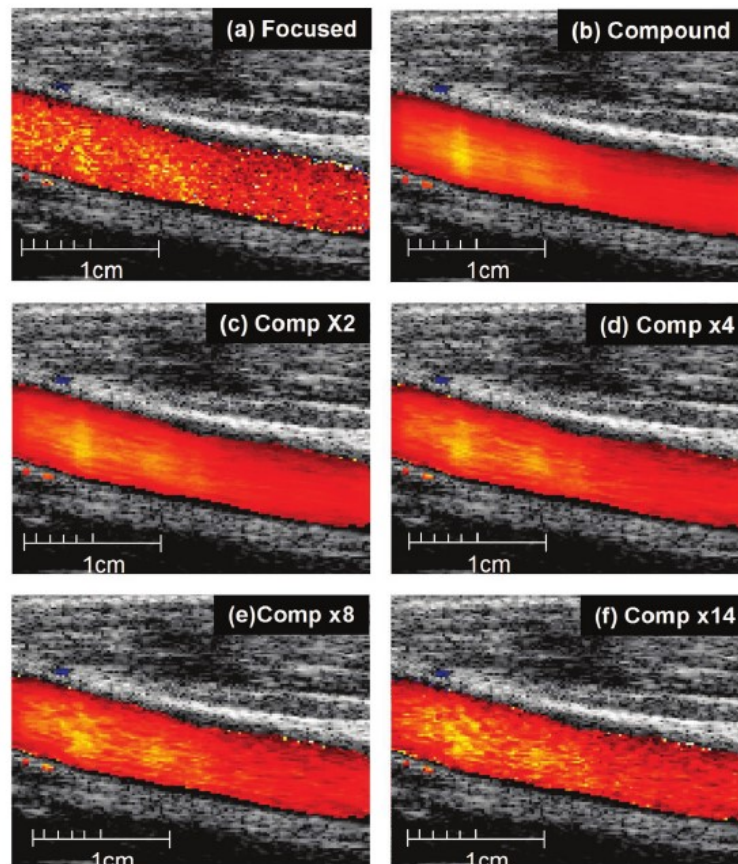
Fig 2.19 A comparison of conventional focused color flow (a) to ultrafast compound Doppler (b) using the same acquisition time. (c) - (f) have reduced acquisition times ranging between 2 to 14 times faster than the color flow example from (a). Adapted from [70], © 2011 IEEE.

Fig 2.19 is displaying what is specifically called the power Doppler signal. Power Doppler is equal to the average intensity of the non-stationary data in the ultrasound image. Equation (2.33) describes the power Doppler signal from a filtered dataset $z_F(x, y, t_i)$, where i represents each successive B-mode image. It has been shown that the power Doppler signal strength is proportional to the blood volume when hematocrit and blood shear rates are constant [110].

$$I(x, y) = \frac{1}{E} \sum_{i=1}^{E} |z_F(x, y, t_i)|^2 \qquad (2.33)$$

By separately integrating the energy for positive and negative frequencies independently, the blood energy moving to and from the probe can be displayed individually using (2.34) and (2.35).

$$I_D^+(x, y) = \int_0^{+\infty} |Z_F(x, y, w)|^2 dw \qquad (2.34)$$

$$I_D^-(x, y) = \int_{-\infty}^{0} |Z_F(x, y, w)|^2 dw \qquad (2.35)$$

In the literature, it is common for both positive and negative velocities to be presented in separate figures since some pixels or voxels can have blood flowing in both directions. Similarly, the projected velocities can be extracted from the spectrogram of Z_F and (2.29). This contrasts color flow techniques where phase-based frequency estimators and time-domain based cross-correlation methods are needed due to the limited number of available samples per location. With ultrafast compound Doppler, it is possible to acquire hundreds of frames that will produce adequate frequency resolution in the spectrogram.

2.7.2 Clutter Filtering

To distinguish blood from tissue clutter, the ultrasonic data is filtered so that the stationary tissue clutter is removed. Early approaches for solving this problem used finite impulse response (FIR), and infinite impulse response (IIR) filters to separate the slow-moving tissue signal from the higher velocity Doppler shift from blood flow via high-pass filtering [108], [111]. These approaches assume that the Doppler shift from the blood flow is significantly greater than that of the tissue signal. For high velocity blood flow this is a reasonable assumption but for slow velocity signals such as that of arterioles in the brain, there can be considerable overlap between the Doppler shift of the slow moving tissue and the Doppler shift from the blood velocity [112]. To circumvent this problem, clutter filters using Singular Value Decomposition (SVD) have been used [112]. SVD filtering is a spatiotemporal filter separating a set of ultrasound images into spatially correlated signals which can be modulated by temporally varying signals. Under this framework the most spatially correlated signal corresponds to tissue signal, whereas the blood flow signal exhibits low spatial coherence. To perform the decomposition, a Doppler ensemble of ultrasound data is first reshaped into a Casorati matrix, S_C. After applying the singular value decomposition, 3 matrices are produced: a spatial eigenvector matrix, U, a temporal eigenvector matrix, V, and a diagonal matrix of ordered singular values, Δ. The original Casorati matrix can be reconstructed from the decomposition using (2.36), where V^* is the complex transpose of V.

$$S_C = U\Delta V^* \qquad\qquad (\,2.36\,)$$

Setting the first few singular values to zero eliminates the most spatially coherent signals from the Doppler ensembles, leaving only the blood signal remaining.

The Casorati matrix is then reconstructed using a filtered singular value matrix, Δ_f. The reconstructed data now contains the blood signal with excellent tissue clutter rejection. The SVD filtering method is used exclusively in Chapter 5.

2.7.3 Functional Ultrasound Imaging

Hemodynamic changes in the brain are a latent response to neural activity and are used as a substitute for directly measuring neural activation. Ultrasound tracking of blood flow can therefore be used to monitor neural activation in response to some stimuli. Periods of stimulus followed by baseline measurements where no stimulus is applied are monitored by capturing power Doppler ultrasound images, as shown in Fig 2.20. Changes in the cerebral blood volume, or the power Doppler signal, are then correlated on a per-pixel basis with the applied stimulus waveform to identify hemodynamic changes which are highly correlated with input stimulus. This approach can be used to generate 2-D and 3-D functional ultrasound mapping of the brain in response to a variety of stimuli ranging from visual stimuli [72], auditory [74], somatosensory [69], and more.
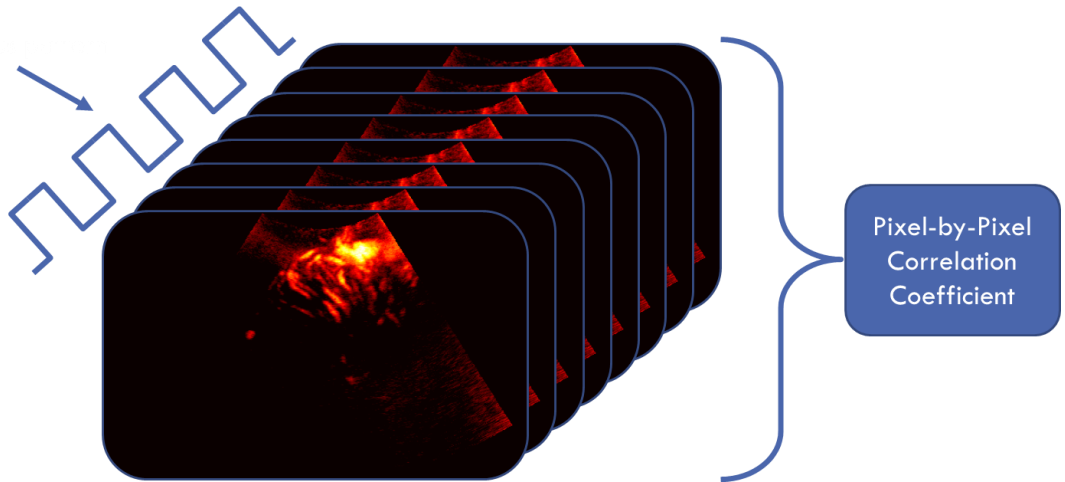
Fig 2.20 Functional ultrasound power Doppler imaging sequence.

Generally, power Doppler is preferred for functional ultrasound imaging of small vessels since it is less susceptible to noise and aliasing than its color Doppler counterpart [71]. Ultrafast compound Doppler is the method of choice for functional imaging since it exhibits significantly higher sensitivity than conventional color flow methods when applied to a large field of view. SNR and sensitivity can be improved by one of two means: increasing the number of frames N, or improving the SNR of the frame data. Functional ultrasound pulse sequences are optimized with these criteria in mind. To maximize sensitivity, the Doppler images must be of the highest possible quality and the number of frames analyzed should be maximized. The first step in this process is to identify the maximum blood velocities that will be detected so that the frame PRF can be identified. For rat brains, blood velocity in arterioles can reach as high as 8.6 mm/s [113]. Many studies on rat brains have used 15 MHz transducers [70], [72], [74], therefore by using (2.29), the Doppler frequency shift would be ~167 Hz. A PRF of 335 Hz would thereby satisfy the Nyquist criterion, ensuring that all arteriole blood flow is captured without aliasing. Not only does this

maximize the number of frames for which the power Doppler signal can be averaged for a given acquisition time, but it also helps define the number of ultrafast compounded frames that can be used to form an image.

2.7.3.1 Functional Ultrasound Applications

A study run by Gesnik et al. successfully monitored the cerebral visual system of rodents [72]. They performed a craniotomy to expose the visual cortex and placed the rodent in a stereotaxic apparatus for the experiment. The rodents were exposed to visual flickering from a monitor covering most of their field of view. Amazingly, Gesnik et al. successfully showed that it is possible to study visual spatialization in the brain by controlling the location of flickering on the stimulus screen [72]. The neuro-activation or cerebral blood volume changes measured using functional ultrasound were spatially correlated based on the position of the stimulus on the screen. They also measured the delay between visual stimulation and hemodynamic variations in the brain to estimate the order in which various regions of the brain are activated, but since the measured delays are much slower than the true neural electrophysiology it is unclear if the delays are confounded by complex vascular dynamics [72].

The auditory response of ferret brains has been studied using functional ultrasound [74]. Neural structures such as the auditory cortex, auditory thalamus, inferior colliculus, and dorsal nucleus of the lateral lemniscus (DNLL) showed a high correlation with auditory stimulus. Impressively, the high spatial-temporal resolution of functional ultrasound allowed the investigators to frequency map the auditory structures to different frequency stimuli. A classifying algorithm used in this study

was trained and used to decode functional ultrasound data, allowing the investigators to estimate the frequency of the sound stimulus applied to the ferrets through functional mapping.

Non-invasive neonatal functional imaging has also been demonstrated through the anterior fontanel window [75], [76]. Quiet and active sleep states can be distinguished by analyzing the intensity of the power spectral density of the recorded ultrafast Doppler data. Neonatal seizures in clinical cases of congenital abnormal cortical development were studied using functional ultrasound and the propagation of neural activation from ictal events was recorded and visualized [75].

As functional ultrasound matured it eventually found itself in a clinical application. It has been used to intraoperatively detect and map functional brain activity in 43 patients [69]. 16 different sensory and motor tasks were mapped to corresponding functional areas of the brain which was corroborated by electrocortical stimulation mapping (ESM). ESM is limited to topical mapping at the surface of the brain whereas functional ultrasound was able to replicate the detection of neural activation in these areas and provided evidence of neural activation at depth which is not possible using ESM.

With so much yet to be discovered regarding the brain, functional ultrasound is a powerful and relatively new tool for studying the brain. It has the potential to improve targeted patient care and study the neural pathways that are activated during neonatal seizures and could potentially help surgeons intraoperatively by distinguishing between malignant and functional brain tissue.

2.8 Applications of High-Frequency Ultrasound

High-frequency ultrasound, typically reserved for ultrasound frequencies between 30-70 MHz, offers an order of magnitude higher resolution compared to conventional ultrasound frequencies (3-10MHz). High-frequencies are subject to small wavelengths leading to improved lateral and axial resolution however the depth of penetration is limited to roughly 1-2cm due to the increased attenuation with frequency. Given these benefits and drawbacks, high-frequency ultrasound lends itself to specific applications where resolution is paramount to resolve structures of interest, and where the depth of penetration is not critical to performance. Applications previously explored include: ophthalmology [1]–[3], [114], dermatology [4], [5], intravascular [8], [9], intra-articular [115], [116], the middle ear [117]–[119], and small animal imaging [119]–[126].

In the field of ophthalmology, ultrasound has been useful in visualizing the anterior segment of the eye, various manifestations of glaucoma, and corneal pachymetry and topologies [1]–[3], [114]. For glaucoma, it is useful to understand the extent to which the tumor has infiltrated important structures such as the sclera, iris, ciliary muscle, and lens of the eye [3], [114].

Visualization of the dermis and epidermis layers of skins are of critical importance in the field of dermatology. Doing so provides clear boundaries for various physiological conditions such as inflammatory skin diseases, wound healing, and tumors. For melanomas, tumor depth and the presence of tumor satellites is of importance for clinical prognoses. High-resolution ultrasound can potentially provide clinicians with the necessary information to make strategic resections with safe margins [4], [5].

High-frequency ultrasound provides a method for imaging calcification and plague on arterial walls which cannot be imaged with other imaging modalities. During intravascular procedures, blockages or narrowed vessels can be opened by puncturing obstructions, or expanded with balloons and or wire meshes, referred to as angioplasty and stenting. Studies have shown that understanding the morphology of arterial plaque can reduce the number of re-stenosis or revisions necessary [127], [128]. Damage-induced to the arterial wall during these procedures has also been shown to strongly predict the likelihood of revision [129], [130]. Many high-frequency systems have been developed to address this market opportunity [8], [9].

Ultrasound guidance of intra-articular knee injections makes use of high-frequency ultrasound to drastically improve the accuracy of articular injections over anatomical guidance [115]. It has also been used in the early detection of osteoarthritis as it can visualize subsurface structure and morphology of cartilage [115], [116], [131].

Ex-vivo and in-vitro studies have been conducted on imaging the middle ear to examine the utility of high-frequency ultrasound as a diagnostic tool [117]–[119]. The middle ear ossicles and tympanic membrane which form a mechanical chain coupling sound to the cochlea have been visualized. The resolution achieved in these studies far exceeds what is possible with CT or MRI which are used clinically. Furthermore Landry et al. have implemented vibrometry on the middle ear, showing great potential for monitoring pathologies in this field [117].

Small animals are used as preclinical models for studying diseases and treatment options. High-frequency ultrasound provides a method for non-invasively imaging small animals in-vivo. This allows researchers to monitor disease progression without

the need to prematurely euthanize animals. Some applications include embryonic brain development [132], tumor models[121]–[124], and cardiac imaging [125].

2.8.1 Current State of High-Frequency Ultrasound

The development of high-frequency transducers and imaging systems has lagged that of clinical ultrasound frequencies due to difficulties associated with micromachining and developing electronics to support these transducers. Early transducer studies such as that undertaken by Foster et al. used small planar transducers [133]. Next came the need to geometrically focus or curve the transducer to improve the depth of field and lateral resolution [133], [134]. At low frequencies, this step can be done through basic machining whereas the $\lambda/2$ transducer thickness at high frequencies is too small for these techniques to be feasible. Solving this problem by shaping the transducer led to a considerable step forward for B-mode applications at high frequencies. The next logical step in the progression of high-frequency transducers was to control the focal depth of the transducer and this was achieved with annular array technologies [15], [17], [21], [135]. Again, at low frequencies, the kerfs between array elements can easily be cut using a diamond cutter, but this was not feasible at high frequencies. This problem was solved using laser micromachining techniques [135], and by placing annular electrodes onto a kerfless substrate [15], [17]. Linear array-based imaging arrays were developed around the same time, eliminating the need for a mechanical translation stage to render B-mode images and greatly increasing imaging speed [11], [14], [16], [18], [19], [136]. These arrays were fabricated with λ pitch using laser micromachining [19], [137], and micro dicing [11], [18], [136]. Lastly came the development of linear phased arrays

61

[10], [12]. Normally phased arrays are the most difficult array technology to manufacture since the element pitch much be kept to $< \lambda/2$ to push grating lobes outside of a 90° imaging window. At high frequencies this is prohibitive. An approach that has been taken by Bezanson et al. is to sacrifice image quality at wide angles by keeping approximately λ pitch element-to-element spacing and packaging the array into a 2.5 x 3.1 mm endoscopic package [10], [12]. This narrows the field of view compared to a conventional 90° field of view, to roughly 64°. To compensate for this drawback, grating lobe suppression techniques can be used to relax the element pitch requirements of phased arrays [38], [62], [90]–[92].

To support high-frequency transducer arrays the electronics used for beamforming needed to be redesigned. Early on, the limitations of A/D sampling rates led to clever sampling schemes reducing the excessive data rates needed for adequately sampling high-frequency RF signals. These approaches involve variable dual-A/D in-phase and quadrature sampling [138], and phased adjusted time-multiplexed sampling [139], [140]. After the development of very high sampling rate A/Ds, researchers have also used brute force sampling techniques to acquire high-frequency ultrasonic data [13].

3 DESIGN OF A REAL-TIME 64-CHANNEL VARIABLE SAMPLING HIGH-FREQUENCY PHASED-ARRAY BEAMFORMER

3.1 Preamble

The work from this chapter has been published in the IEEE Transactions on Ultrasonics, Ferroelectrics, and Frequency Control as "A Sub-Nyquist, Variable Sampling, High-Frequency Phased Array Beamformer", © 2016 IEEE. Reprinted, with permission, from [34], its contents remain largely unchanged with minor modifications made throughout. At the time of publication, this system multiplexed between 8 of the 64 channels on the phased array used in this work. Since then the system has been updated substantially so that data from 64 channels can be captured in parallel. The updated system, which was designed after the time of publication, is described in this chapter as it is the system used throughout the remaining chapters.

3.2 Introduction

Recent developments have led to the manufacturability of miniaturized (<3 mm) high-frequency phased-array endoscopes [10], [12]. These endoscopes operate at 45 MHz using 64 elements and facilitate imaging inside the body with resolution comparable to linear-array technologies, which are limited to topical applications only

[11], [14], [18]. This technology has been noted for its potential to improve medical diagnostics and guided surgical procedures. Surgical procedures performed under image guidance have become the standard of care for procedures of the colon, pancreas, uterus, kidneys, liver, esophagus, bile duct, spleen, brain, and bowel. These procedures typically rely on optical images and would benefit from depth-resolved images with tissue contrast that can be provided by high-frequency ultrasound. Furthermore, previous work has demonstrated potential applications for miniature forward-looking ultrasound endoscopes for guided laparoscopic, auditory, intracardiac, and neural procedures [7], [118], [141], [142].

To maximize the potential of this technology, a robust low-cost high-frequency beamformer is required to support the high-frequency phased array endoscope. Conventional beamforming methods require prohibitively high sampling rates, typically between 4-10 times higher than the center frequency [13], [143] before additional upsampling is required to achieve sufficient delay resolution. At high frequencies, effective sampling rates after upsampling can be as high as 1.5 GHz to achieve sufficient beamforming quality. Given a system using 12-bit analog-to-digital (A/D) converters and 64 channels, the effective data capture rate for a brute force beamformer could be as high as 1.1 Tb/s. This prohibitively high data rate certainly discourages attempting high sampling and data rate approaches. Previous beamforming techniques that have used lower sampling rates and data rates include: shifting the A/D clocks for subsequent transmit events [140], variable sampling [138], [144], and compressed sensing [145]–[147]. The clock-shifting method requiring multiple transmit events effectively reduces the requirements on the A/D sampling rate but results in a decreased frame rate and no reduction in the total size of the oversampled data sets. Compressed sensing is formulated on the underlying

64

assumption that received signals can be modeled using the superposition of a small series of pulses with some known pulse shape [145], [146]. For ultrasound imaging, it has been shown that the reconstruction of the pulse-echo signals can be completed by extracting the phase delay and amplitude of each of these known pulses, all of which can be determined in the frequency domain from signals captured with sampling rates much less than the Nyquist rate [145], [146]. However, this method requires that a discrete Fourier transform (DFT) be completed on each channel, imposing significant processing overhead and complexity. Alternatively, variable sampling techniques offer low sampling rates with very simple signal processing [138], [144]. Unlike conventional beamforming methods where the samples are digitized at a constant rate and then selected from an oversampled buffer, the variable sampling technique adjusts the rising edge of the A/D converters' sampling clocks so that only the precise samples required for beamforming are collected. This is accomplished by pre-calculating the exact return TOF between each of the elements and each of the pixel locations. By collecting the data in this manner, beamforming can be completed by simply adding the collected data from each element without needing to digitally realign samples in hardware or software. Finally, envelope extraction is facilitated by simple in-phase (I), and quadrature-phase (Q), demodulation. Despite having been implemented on annular and linear arrays, the variable sampling method has not previously been implemented on a phased array transducer due to the added complexity of the sampling patterns changing with the steering angle.

Furthermore, despite reducing the amount of data collected, previous variable sampling techniques relied on I-Q samples separated by one-quarter wavelength to demodulate and envelope detect the ultrasonic signal [138], [144]. To achieve quarter wavelength sampling, the upper end of the sampling rate must be four times greater

than the center frequency. For example, at an ultrasound center frequency of 50 MHz, a 200 MHz sampling rate would be required to capture the in-phase and quadrature samples. Such sampling rates impose high design costs and troublesome data rates.

In this chapter, a newly developed variation of the variable sampling method is described. The proposed method approximates the signal envelope by spacing in-phase and quadrature samples at ¾ λ instead of the conventional ¼ λ, reducing the required sampling rate by a factor of 3. By exploiting the moderate pulse bandwidths used in high-frequency ultrasound transducers, demodulating at ¾ λ has a negligible effect on the accuracy of envelope detection, given that the temporal length of the pulse envelope is significantly longer than ¾ λ. This sampling method was implemented on a field-programmable gate array (FPGA) and the timing accuracy of the variable sampling was quantified. The system data is subsequently acquired through 8 receive daughter cards where each card captures 8 channels of data through parallel A/D converters. Once sampled, the data is beamformed across 9 FPGAs and sent to a PC for display on a custom graphical user interface written in Python 2.7 [148].

3.3   Sampling Methodology

Conventional variable sampling relies on ¼ λ spacing between samples to reduce the amount of data that is collected for image construction, Fig 3.1 (a). When implementing this sampling scheme, the timing of the rising edges of the A/D clocks is typically controlled by an FPGA. This control has previously been facilitated by manually adjusting the rising edges driven to multiple A/D converters [138]. To

properly embed beamforming into the sampling scheme each sampling time is precisely controlled, creating a varying clock frequency.

The variable sampling technique requires that two samples be acquired by each element for every pixel. The presented sampling technique reduces this data rate, which is referred to as the 'one sample per pixel' technique. It is a ¾ λ I-Q sampling/demodulation simplification of the ¼ λ variable sampling demodulation technique. In this method, each successive sample in the image is temporally spaced by ¾ λ (see Fig 3.1 (b)) which results in a spatial spacing of 3/8 λ. The round trip TOFs for each element to each pixel are calculated almost identically to that of previous variable sampling technology. The key difference lies in the demodulation of the signal envelope and the spacing of the image pixels. Each sample corresponds to one pixel and each pixel is temporally separated by ¾ λ. It first acts as the quadrature (Q) sample for the previous pixel, and subsequently serves as the in-phase (I) sample for the current pixel. IQ demodulation is thus applied to the current and previous samples. This differs from previous ¼ λ variable sampling techniques, which require at least two samples per pixel [144]. The effectiveness of this technique is dependent on the relative bandwidth of the transducer. Given that the pulse bandwidth is moderate in most high-frequency array-based systems, the temporal length of the pulse will be adequate for its envelope to be approximated with ¾ λ sampling. In doing so, the effective sampling rates are reduced by a factor of three, and the data rate is halved. Only one sample is thus required for each pixel for each element. At 45 MHz, the highest sampling rate is reduced from 180 MHz for the ¼ λ variable sampling technique, to 60 MHz for the 'one sample per pixel' technique.
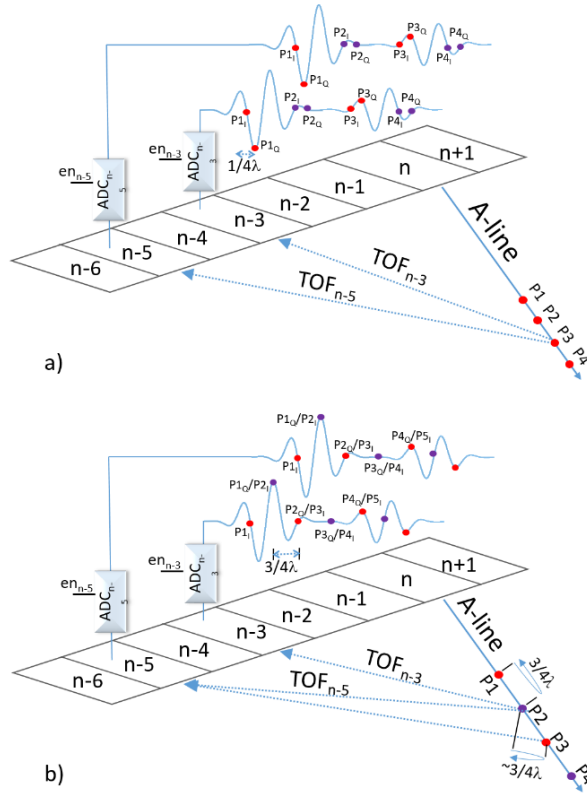
Fig 3.1 A comparison of variable sampling techniques. (a) ¼ λ sampling whereby each pixel is sampled twice for each element with its independent I and Q samples. (b) ¾ λ sampling whereby each pixel is sampled once for each element and its respective I and Q samples are shared amongst neighboring pixels.

The reduced sampling rate produced with this method only works if adjacent pixels are temporally spaced by ¾ λ, which means they are spatially separated by 3/8λ. The temporal spacing accounts for the round trip TOF to and from a pixel. Thus, the pixel pitch Δr can be calculated by using (3.1) where c is the speed of sound and f_c is the center frequency of the ultrasound pulse. This is a reasonable pixel spacing since the spacing is much less than the width for most transducer bandwidths. The time of flight (TOF) for each sampling time is calculated with (3.2

) for each pixel depth r_i, steering angle θ_k, and array element N, given an array element pitch of el_p.

$$\Delta r = \frac{3c}{8f_c} \qquad (3.1)$$

$$TOF = \frac{r_i + \sqrt{(r_i \cdot \cos(\theta_k))^2 + \left(r_i \cdot \sin(-\theta_k) - (0.5 - N/2) \cdot el_p\right)^2}}{c} \qquad (3.2)$$

To theoretically evaluate the effectiveness of the 'one sample per pixel' technique, the relationship between bandwidth and maximum possible error in envelope amplitude is derived. First, consider the ideal case where an in-phase sample falls on the peak of the Gaussian modulated pulse. The quadrature sample will then fall on a zero crossing, and in this instance, the peak envelope will be perfectly estimated. Now consider a non-ideal case where the in-phase and quadrature samples are located symmetrically around the peak of the RF pulse. The ultrasound pulse is defined by

$$g(t) = \cos(w_c t) \cdot e^{\frac{-t^2}{2\sigma_w^2}}. \qquad (3.3)$$

The Fourier transform of (3.3) is expressed as

$$G(jw) = \sigma_w{}^2 \sqrt{\frac{\pi}{2}} \cdot \left(e^{\frac{-(w-w_c)\cdot\sigma_w{}^2}{2}} + e^{\frac{-(w+w_c)\cdot\sigma_w{}^2}{2}} \right). \qquad (3.4)$$

In order to extract the signal bandwidth, the positive frequencies of (3.4) are isolated. Bandwidth is defined as the full-width half maximum of the frequency spectrum. Solving for the range of w around w_c, to which the Gaussian component of the frequency spectrum is equal to ½ produces the bandwidth in angular frequency.

$$w = w_c \pm \frac{\sqrt{2 \cdot \ln 2}}{\sigma_w}, \qquad (3.5)$$

$$BW = w_+ - w_- = 2 \cdot \frac{\sqrt{2 \cdot \ln 2}}{\sigma_w}, \qquad (3.6)$$

69

For convenience, the bandwidth may subsequently be normalized to the center frequency by dividing by w_c, as shown by (3.7).

$$\%BW = \frac{2}{w_c \sigma_w} \sqrt{2 \cdot \ln 2} \qquad (3.7)$$

Next, the envelope amplitude decay between successive samples is defined

$$a_d = e^{\frac{-t^2}{2 \cdot \sigma_w^2}}. \qquad (3.8)$$

To calculate the maximum envelope estimation error the Gaussian component of the ultrasound pulse is rearranged to solve for t as follows:

$$t = \pm \sigma_w \sqrt{-2 \cdot \ln a_d}. \qquad (3.9)$$

The time between sequential samples Δt is then inferred by taking the difference between two points centered on the pulse peak at a reduced envelope amplitude r,

$$\Delta t = t_2 - t_1 = 2\sigma_w \sqrt{-2 \cdot \ln a_d}. \qquad (3.10)$$

The above expression is manipulated to describe the effective sampling rate,

$$f_s = \frac{1}{\Delta t} = \frac{1}{2\sigma_w \sqrt{-2 \cdot \ln a_d}}. \qquad (3.11)$$

Next (3.10) is rearranged to express the attenuation a_d in terms of standard deviation σ_w and sampling rate.

$$a_d = e^{\frac{-1}{8 \cdot \sigma_w^2 \cdot f_s^2}}. \qquad (3.12)$$

For convenience, the expression is positively referenced and converted into dB before (3.7) is rearranged for σ_w and substituted into (3.12)

$$a_{d\,dB} = -20 \log \left(e^{\frac{-\pi^2}{16 \cdot \ln 2} \left(\frac{f_c \cdot \%BW}{f_s} \right)^2} \right). \qquad (3.13)$$

Using (3.13), the maximum possible envelope amplitude loss can be plotted across a range of sampling frequencies. Fig 3.2 highlights the envelope amplitude loss between samples for integer multiples of ¼ λ sampling as a function of bandwidth. Naturally, as bandwidth increases, the temporal duration of the pulse shortens, and the signal begins to decay before it's sampled.

The curves in Fig 3.2 are useful for understanding the limitations of sparsely sampling the ultrasound signal for estimating the signal envelope. For instance, if it is desired that the maximum error on envelope detection be less than 3 dB, the maximum pulse bandwidth for 3/4 and 5/4 λ schemes are 83.0 and 49.8% respectively. Thus the 'one sample per pixel' variable sampling technique provides an accurate approximation to conventional variable sampling methods provided that the pulse bandwidth is below 83%. It should be noted that the worst-case scenario for sampling the ultrasound pulse is not necessarily when the samples are centered on the maximum of the RF pulse, however, this is a near worst case that is simple to derive. Numerical simulations were conducted of all cases of in-phase and quadrature sampling, and for bandwidths up to 80%, the derivation for the envelope estimation error remains valid within 2.5 dB.
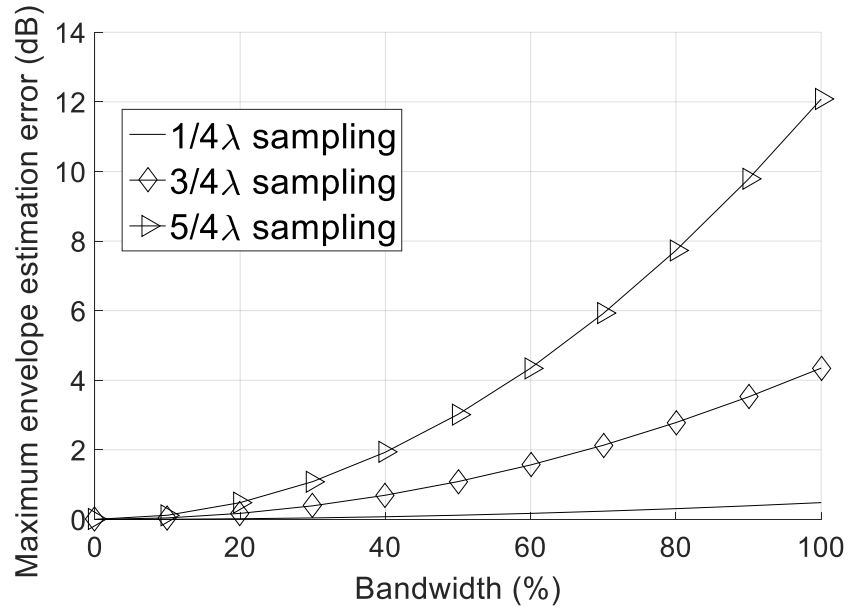
Fig 3.2 Maximum envelope estimation error in (dB) compared for integer multiples of 1/4 wavelength sampling techniques as a function of percent bandwidth.

Fig 3.3 highlights the qualitative similarities between ¼ and ¾ λ demodulation from an oversampled data set generated from a 45 MHz phased array probe [10], [12]. Images were generated from a custom tissue phantom with 50 µm nylon wires embedded (Gammex, Middleton, WI). Virtually no noticeable difference in image quality results when demodulating with ¾ λ.
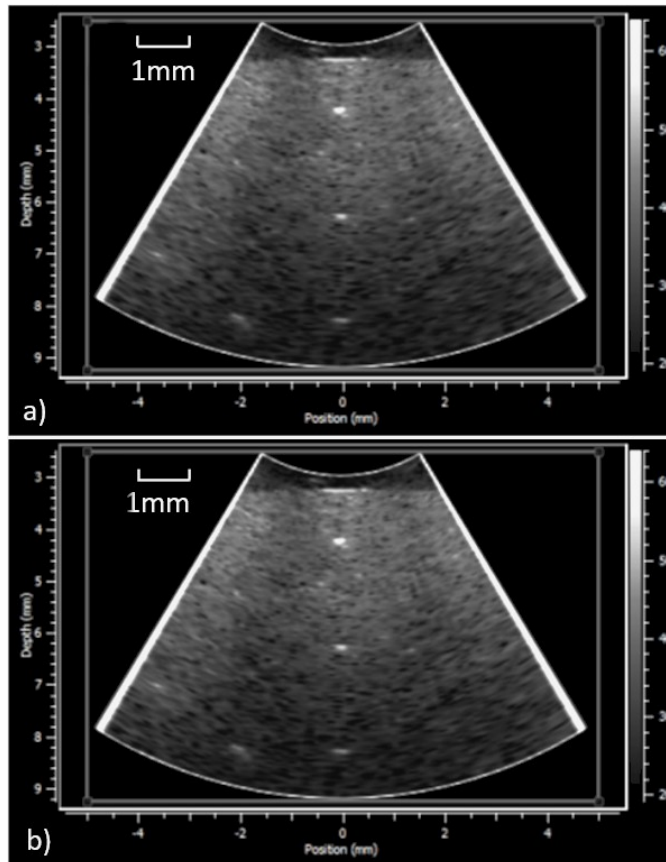
Fig 3.3 Comparison of ¼ and ¾ wavelength demodulation on simulated oversampled data. (a) ¼ wavelength sampling, and (b) ¾ wavelength sampling.

In addition to comparing ¼ λ and ¾ λ demodulated images with a phased array endoscope that has approximately 60% bandwidth, images generated using a commercially available 85% bandwidth 50 MHz linear array transducer manufactured by Visualsonics Inc. (VisualSonics MS70, Toronto, Ontario) were also compared. The IQ data was exported, upsampled, and demodulated at both ¼ λ and ¾ λ. Fig 3.4 shows an image of a guinea pig inner ear cochlea containing several fine membranes and ducts. The ex-vivo small animal imaging was conducted under an approved ethics protocol (15-026: Imaging of Ear using micro-ultrasound and OCT). Although details of these structures are not relevant to this concept, layered tissue structures such as

this will be the most susceptible to any noticeable decrease in axial resolution due to an error in envelope estimation, particularly with a relatively high-bandwidth transducer such as the MS70. The signals were captured using the VisualSonics, Vevo 2100 imaging system. The RF data was saved, upsampled, and then demodulated using ¼ λ and ¾ λ one sample per pixel quadrature sampling offline in MATLAB. When comparing these images, there is no significant loss in image quality or axial resolution between the two demodulation schemes.
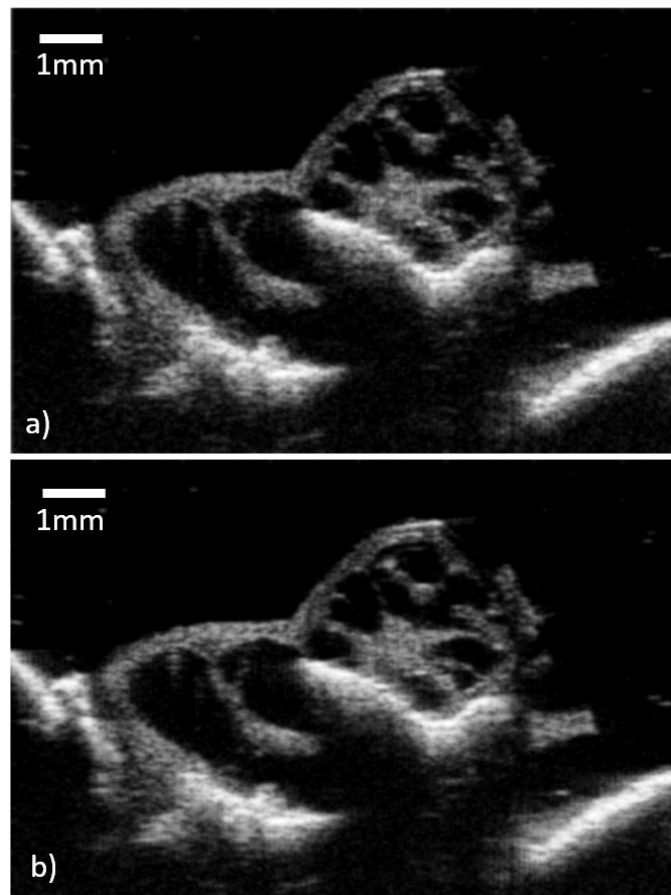
Fig 3.4 Comparison of ¼ and ¾ λ demodulation on an ultrasound image of a guinea pig inner ear and cochlea. The data was collected using an 85% bandwidth 50 MHz linear array manufactured by Visualsonics Inc. (a) ¼ wavelength sampling, and (b) ¾ wavelength sampling.

3.4 System Design

A receive beamformer implementing the 'one sample per pixel' sampling method has been developed using 9 FPGAs (XC7K160TFBG484-2, Xilinx, San Jose, CA). The variable sampling for each channel is generated by combining a pipelined high-frequency counter and a high-speed finite state machine (FSM). The variable sampling timing logic operates at 625 MHz where the sampling times are theoretically limited to ± 0.8 ns or half of the clock period. Fig 3.5 shows the variable sampling architecture implemented on the FPGA. Coarse and fine delays are controlled by preconfigured ROM modules stored internally to the FPGA. Coarse delays are used to control the beginning of each line acquisition and are calculated based on the TOF between the array elements and the first sample for each line. Transmit pulse sequencing is initialized as the coarse delay counter rolls over, therefore its length controls the system's pulse repetition interval (PRI). Once the coarse delay matches the counter value from the coarse delay ROM, the FSM is enabled. Subsequently, fine delay control dynamically adjusts the timing for each successive sample generated by the FSM.
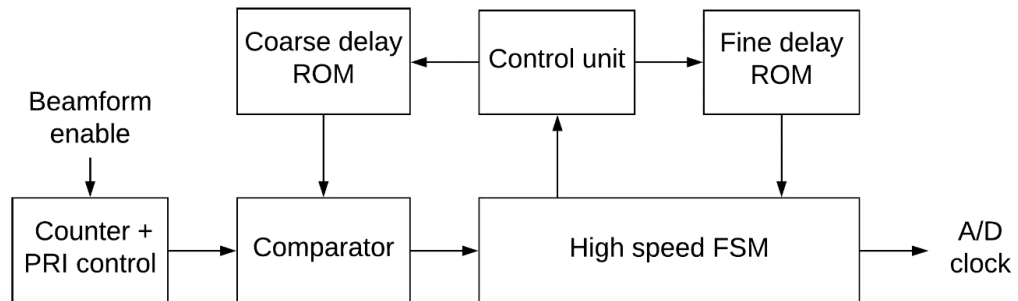
Fig 3.5 A block diagram of the FPGA variable sampling architecture.

As the FSM generates the A/D clocks or 'pulse trains', the fine and coarse delay ROMs are updated for the subsequent samples and lines. For optimal FPGA performance, the fine delays are controlled with one bit for each sample. The delay between samples is controlled to be as close to ¾ λ as possible by alternating between delay periods above and below ¾ λ. Given a system center frequency of 45 MHz, the FPGA must sample roughly every 16.7 ns. Due to the influence of geometry and digital quantization this number varies slightly for each sample, however, the calculated ideal sampling time is approximated sufficiently well (<1 ns) by sampling at intervals of either 16 or 17.6 ns. These sampling intervals correspond to 10 and 11 high-frequency clock cycles for this system and is controlled with a single bit from the fine delay ROM from Fig 3.5. Fig 3.6 describes the flow through the FSM. With every clock cycle, the state machine advances to the next state, once the FSM reaches the second last state a decision is made based on the ROM input to assert the A/D clock and return to state S0 or to advance to the last state. This decision provides a 1.6 ns or 1 clock cycle variation that is needed to implement variable sampling. For this system if the FSM advances to the last state, the effective delay from the previous rising edge of the clock will be 17.6 ns, alternatively, if the FSM returns to S0 at the second last state, the clock edge delay will be 16 ns. The duty cycle of the pulse is also controlled by the state machine, its output remains high for 5 clock cycles or states before being released.
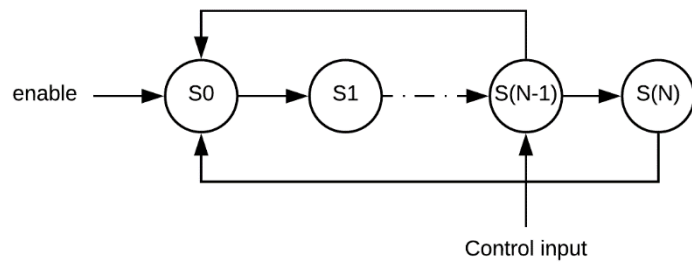
Fig 3.6 Finite state machine flow diagram. The output is asserted at S(N-1) or S(N) based on the control input to the FSM.

The receive beamformer described above has been integrated into a complete ultrasound system. The hardware architecture for the full system is shown in Fig 3.7. The system consists of 1 receive motherboard, 8 receive daughter cards, 1 transmit motherboard, 8 transmit daughter cards, 1 interposer, and a PC. A second transmit daughter card and 8 biasing boards are included in the system but are not pertinent to this dissertation as they are used for 3D imaging which is not covered under this project.
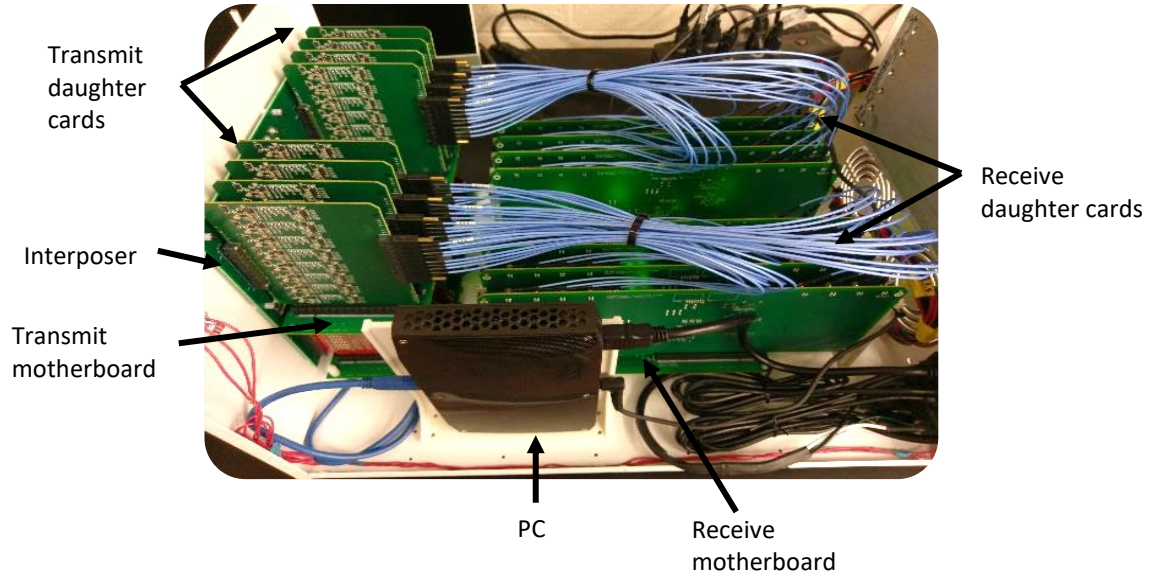
Fig 3.7 Beamforming system hardware configuration.

The FPGA on the receive motherboard has been configured to generate the variable sampling encode clocks used to trigger 64 A/D converters. The A/D clocks are thereafter routed through the 8 receive daughter card FPGAs before they are distributed to the A/D converters. The average sampling rate is approximately 60 MHz and therefore the data capture rate is 60MHz x 64 channels x 12 bits, which roughly equals 46 Gbps. The receive daughter card FPGAs provide buffering and skew control. Skew control is implemented by referencing the delay paths to a virtual clock, allowing for input and output constraints resulting in improved user control. The receive daughter card FPGAs also perform initial data acquisition from 8 parallel A/Ds, store data into memory, provide preliminary beamforming, and transfer data to the receive motherboard. The receive motherboard initiates data transfer after the complete dataset for an image frame has been captured. Four of the eight daughter cards transfer data simultaneously. Once data transfer has completed from the first

78

set of daughter cards the next set of cards is enabled for data transfer. Transferring data from only four cards at a time is due to IO resource limitations on the receive motherboard, the FPGA does not have enough IOs to support transferring data from each of the eight cards in parallel. The data transfer interface between each daughter card and the motherboard is 18 bits wide and runs at 100 MHz for a data transfer rate of 7.2 Gbps. Fig 3.8 describes an overview of the system connectivity. The transmit beamformer is synchronized to the receive beamformer. Since the receive beamformer controls the standoff and sampling times for each channel it must provide a reference trigger to the transmit beamformer so that the time delay between transmission and reception is as accurate as possible. Once a trigger is received, the transmit beamformer initiates high-speed counters and pulse control modules similar to what is used to control the variable sampling A/D clocks. After each transmit event the delay addresses are updated to read the next delay values from FPGA ROM corresponding to the next transmit event required for imaging. Pulse focusing is steered to 128 lines with 4 focal zones per line. Steering spans $\pm32°$ from the center of the image and the focal zones are located at 3.8, 4.7, 6.3, and 7.8 mm. For each imaging cycle, the system sweeps through each focal position and dynamically receives the pulse echoes. As data is transferred to the receive motherboard it beamforms the data by summing the samples transferred from the receive daughter cards, splices the focal zone data, and stores the beamformed frames. The beamforming system now becomes idle until the PC requests an image frame through a USB3.0 interface. After transferring the frame data to the PC, the system will automatically initiate a new imaging sequence.
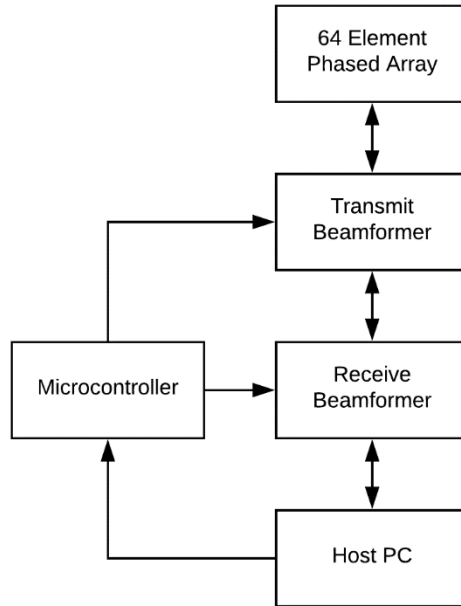
Fig 3.8 High-level system architecture of high frequency phased array beamformer.

Envelope detection, log compression, and scan conversion are facilitated on the host PC. Scan conversion uses bilinear interpolation on the beamformed data and upsamples by a factor of 4. A Hilbert transform is used for envelope detection and bandpass filtering is controllable through a GUI. The user interface is connected to an Arduino Uno which serves as a serial interface between the PC and an I2C bus connected to DACs on the imaging hardware. Two different DACs are located on the system (LTC2627CDE, and LTC2633CTS8) which control the variable-gain amplifiers (VGA) and the pulse voltage.

3.5   Experimental Results

The FPGA architecture and timing accuracy for the one sample per pixel ¾ λ variable sampling technique was experimentally validated using a 4GS/s oscilloscope (MSO-X 3052A, Agilent Technologies, Sata Clara, CA). The FPGA was designed to receive 64 elements simultaneously over 128 angles, and 512 pixels per angle. This means that the FPGA-based receive beamformer generates approximately 4.2 million precisely timed triggering events directed to the A/Ds. To measure how accurately the architecture could generate these 4.2M precisely timed samples, an oscilloscope was synchronized with the beginning of each imaging sequence from a reference signal generated by the receive motherboard's FPGA. The oscilloscope was directly connected to the A/D clocks on each of the 8-channel receive daughter cards. Data were retrieved from the oscilloscope via an automated script written in Python for timing analysis. The script controls the time position and reading of data from the oscilloscope. The rising edge time for each encode clock is measured, stored into memory, and the time position of the oscilloscope is advanced for the next clock edge. This process is continued until all rising edges for a given line have been recorded, then the script advances to the subsequent beamforming pattern or line. Once all the data has been collected the beamforming times are referenced to the transmit events for each respective line and are compared to the theoretically ideal sampling times. This process is repeated for each channel.

The rising edges of the variable sampling clocks from the FPGA were within ±1.0 ns of the theoretical ideal sampling times. Fig 3.9 highlights a typical sampling accuracy distribution for the rising edges of the variable sampling clocks. The clock jitter was measured to be less than 100 ps. Theoretically, the timing accuracy should

be confined to the digital quantization error of ±0.8 ns, however, variations in clock trace lengths, superposition of clock jitter, variations in analog propagation delays, and the digital quantization error from the oscilloscope introduce increased timing errors. At 45 MHz ±1.0 ns corresponds to less than $1/20^{th}$ of a wavelength and is adequate for high-quality beamforming. The receive delay errors follow a uniform distribution. Further improvements may be obtained through tighter control of printed circuit board trace impedances and propagation delays, as well as utilizing a higher bandwidth oscilloscope.
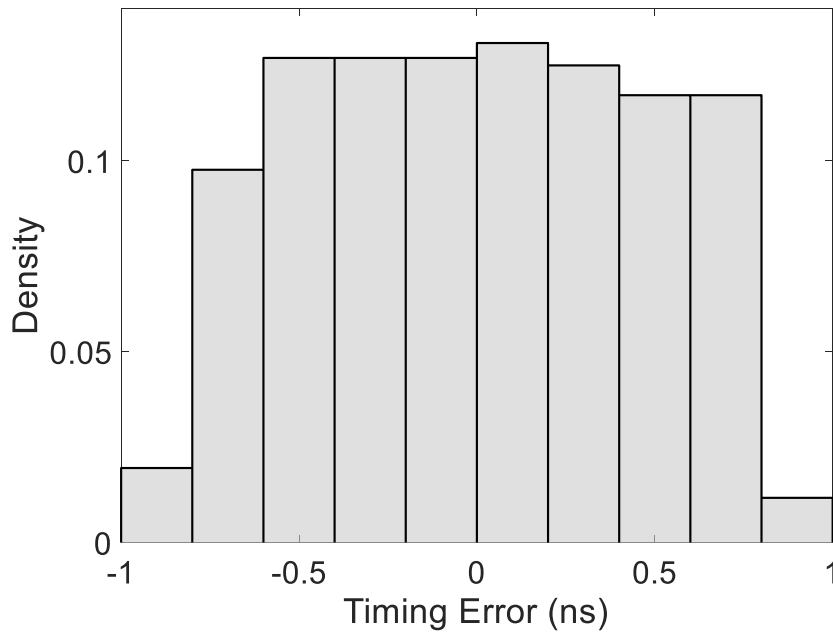
Fig 3.9 A sample timing error distribution for the receive beamformer.

The transmit timing accuracy was evaluated similarly to that of the receive timing accuracy. The transmit times were measured by connecting the output of the analog front end to the oscilloscope through a 20-dB attenuator. The oscilloscope was synchronized to a reference trigger generated by the receive beamformer. A Python

script was used to automate the acquisition of transmission times while simultaneously storing the data into memory and comparing them to the ideal theoretical transmission times. This process was repeated for each of the 64 channels. Post-processing shows that the transmit timing errors follow a uniform distribution ranging between ±800 ns see Fig 3.10 for details.
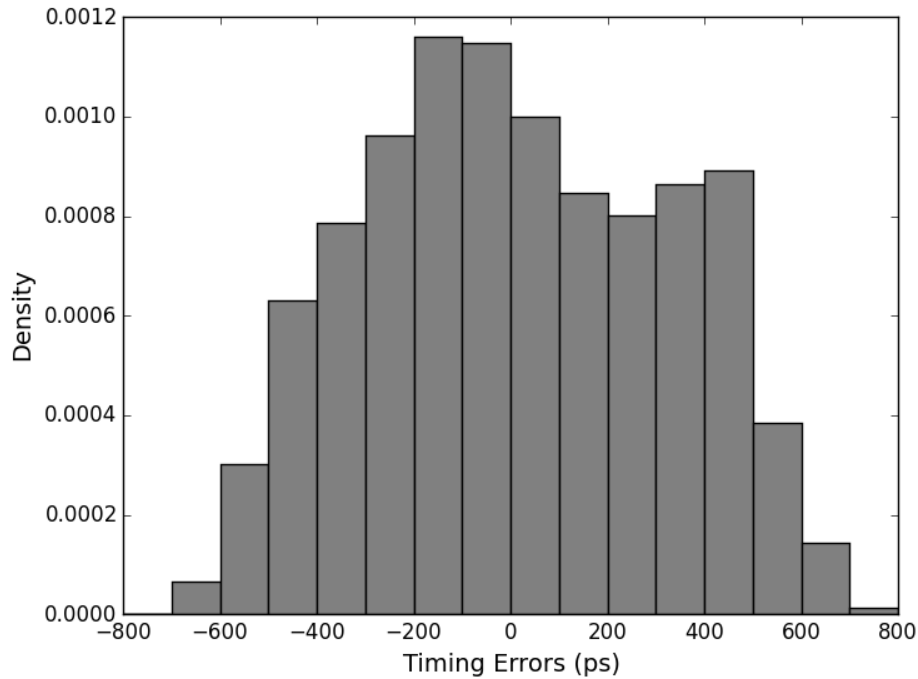
Fig 3.10 A sample timing error distribution for the transmit beamformer.

Two-way radiation patterns were collected in real-time on the host computer while imaging an 18 µm aluminum wire target submerged in a water bath. The wire target was aligned along the elevation plane of the imaging window to approximate a point target within the image. Translating the wire target laterally enables the collection of radiation patterns at various angles. The wire target was situated at a depth of 6.2 mm (F ~ 2.5). Two-way radiation patterns were collected at steering

83

angles of 0, 15, and 25°, illustrated in Fig 3.11. Approximately 55 dB of dynamic range was experimentally measured at both shallow and wide angles. The simulated radiation patterns were generated in Field II and the distributions of beamforming errors were also inserted directly into the model. The beamforming errors inserted for receive were uniformly distributed between ±1.0 ns to match the system measurements and the transmit errors were uniformly distributed between ±0.8 ns to match the experimental transmit delay measurements of Fig 3.10.
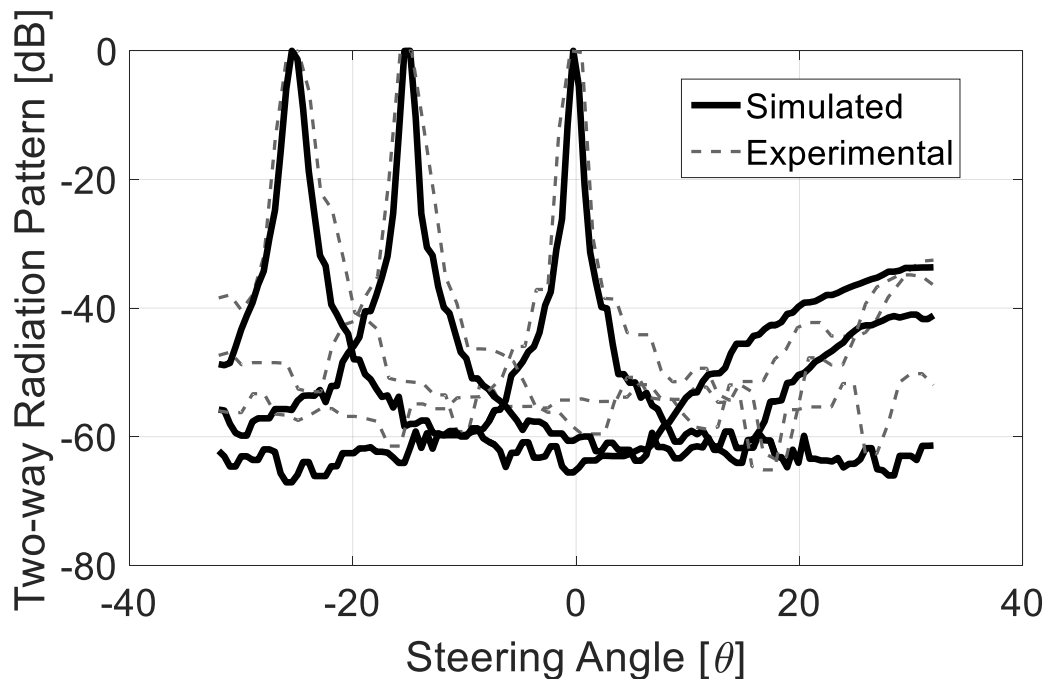
Fig 3.11 Comparison of experimental radiation patterns with simulated radiation patterns generated in Field II. The simulated radiation patterns are modeled with inserted beamforming errors, mimicking experimental error data.

The lateral resolutions at various angles were calculated by measuring the -6 and -10 dB points of the two-way radiation patterns at 0, 15, and 25°. The theoretical -6 dB lateral resolutions for these angles are simulated to be 92, 114, and 146μm.

The simulated -10 dB lateral resolutions are 119, 137, 180µm. In comparison, the experimental -6 dB measurements were 136, 186, and 205 µm at the respective angles. Whereas the -10 dB lateral resolutions were measured to be 170, 239, and 288 µm respectively. The axial resolution was measured by calculating the -6 dB width of a beamformed envelope from a pulse-echo returning from the wire target and then dividing this by two to compensate for the two-way TOF. This was calculated to be approximately 40 µm at a wide range of steering angles. Lastly, the grating lobes inherent to the 1 λ pitch phased array are accurately positioned compared to the simulated data.

3.6   Imaging Examples

The imaging performance was evaluated when imaging a tissue phantom with five 18 µm aluminum wire targets (ALW-29S, Heraeus), see Fig 3.12. The wire targets are aligned parallel to one another and spaced by approximately 1 mm in both the lateral and depth planes. The targets are suspended in a tissue phantom made from a gelatin mixture. The % by mass mixture is comprised of 6% gelatin (Porcine skin, G2500-1KG, Sigma-Aldrich, St. Louis, MO), 4% silicon dioxide (S5631-500G, Sigma-Aldrich, St. Louis, MO), and 90% deionized degassed water [149]. The image was generated using 128 lines with 512 pixels sampled for each line. Each of the image lines is split with two transmit focal zones positioned at radial distances of 5 and 7 mm from the center of the array. The entire image spans an axial depth of 3 to 10 mm and sweeps between ±32°. The image exhibits over 30 dB of reflector-to-speckle contrast between the wire targets and average tissue speckle.
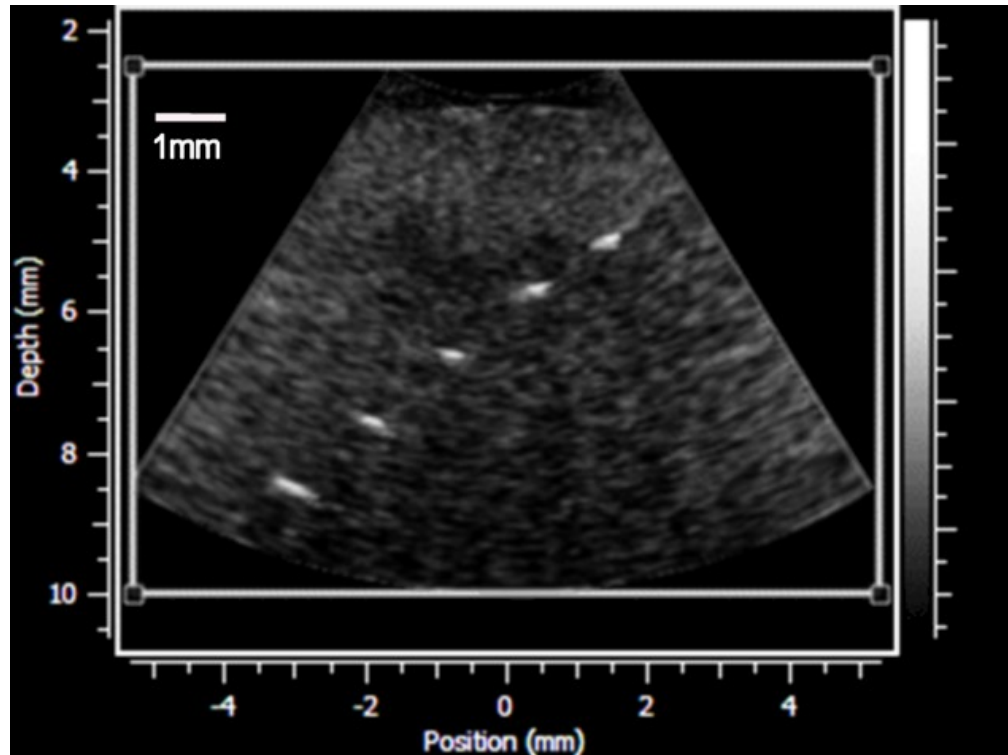
Fig 3.12 Image of five 18 μm aluminum wire targets embedded in a tissue phantom. The wire targets are separated by approximately 1mm in both the lateral and depth directions.

Fig 3.13 shows an in-vivo image of a rat brain. The image is of the midbrain on the sagittal plane behind the midline. The image was collected in real-time using 128 lines with 512 pixels sampled for each line. Each of the image lines is split with four transmit focal zones positioned at radial distances of 3.8, 4.7, 6.3, and 7.8 mm from the center of the array. The entire image spans an axial depth of 3 to 10 mm and sweeps between ±32°. The image was displayed with approximately 55 dB of dynamic range and clearly displays a large artery near the surface and an aqueduct at the bottom of the image is visualized with excellent contrast and good tissue penetration. In real-time, the specular motion of the blood flow through the artery and other, much smaller vessels, can also be visualized.

86

Fig 3.13 A real-time in-vivo image of a rat midbrain from the sagittal plane view from the midline.

3.7 Discussion

Overall, the performance of the beamformer was very good. The timing accuracy of the variable sampling receive delays were adequate for high-quality beamforming, and the envelope estimation using the one-sample per pixel ¾ λ demodulation was almost indistinguishable from traditional ¼ λ demodulation.

The largest discrepancies between the theoretical simulated performance of the imaging system and the experimental measurements were in two results: 1) The experimentally measured lateral resolution was worse than the theoretical, and 2)

The level of sidelobes relative to the main lobe was approximately 10 dB higher than the theoretical impulse response simulations.

The most likely discriminating factors between the experimental and simulated radiation patterns from Fig 3.11 are: 1) the use of an imaging array that is not traditionally kerfed, and 2) the use of a wire target in place of a point target. Comparisons between finite element modeling of kerfless arrays and ideal impulse responses have previously shown that kerfless arrays may exhibit a slight increase in sidelobe levels relative to the main lobe [15]. The experiments exhibit similar degradation in the sidelobe level compared to the theoretical model. Lastly, the impulse response simulation models a point spread function (PSF), whereas the actual experimental measurements are of a line spread function (LSF). Signals reflecting off-axis from a line target in the elevation plane overlap and tend to slightly degrade the quality of beamforming. Implementing sub-wavelength point reflectors for the experimental measurements would be extremely difficult to fabricate for an ultrasound wavelength of 33 µm.

Although using a kerfless phased array transducer instead of a perfectly kerfed array, and approximating the PSF with an LSF will contribute to a decreased lateral resolution and increased level of sidelobes, there is still a relatively good match between the impulse response modeling and the experimental measurements. The lateral resolution was measured to be on average 52% larger than the theoretical diffraction limit over a range of angles and the sidelobes are approximately 10 dB higher than the impulse response model. It should be noted that when comparing the simulated beam widths with additive delay errors to ideal simulated beam widths, the lateral resolution is left relatively unchanged whereas the sidelobes rise considerably. Under this notion, it can be presumed that most of the discrepancies

in lateral resolution can be attributed to the nature of the kerfless array and the LSF approximation of the PSF.

3.8   Conclusions

High-frequency beamforming for phased array probes typically requires high sampling rates and many hardware resources to be achieved. The system and methods in this work have shown that the sampling and data capture rates can be reduced by a third and a half, respectively, in comparison to previous work on variable sampling. This method has been implemented on an FPGA platform with timing accuracy within $1/20^{th}$ of a wavelength. One drawback to this described technique is its inability to derive multiple lines of sight from one insonification, rendering it inapplicable to many ultrafast imaging modalities such as plane-wave imaging or multi-line acquisition. Despite this drawback, many studies have shown that for phased array imaging, single line transmission yields the best image quality [81],[82]. Therefore, the proposed technique is more than adequate for high-frequency medical imaging with significant technical simplifications.

4 ULTRAFAST PHASED-ARRAY IMAGING USING SPARSE ORTHOGONAL DIVERGING WAVES

4.1 Preamble

The following chapter presents a new transmit pulse encoding scheme for ultrafast phased array imaging called sparse orthogonal diverging-wave imaging (SODWI). In SODWI, Hadamard encoding is used to selectively invert array element transmit pulse phases while surfing this code on a diverging wave delay profile. This work has been published in the IEEE Transactions on Ultrasonics, Ferroelectrics, and Frequency Control as "Ultrafast Phased Array Imaging using Sparse Orthogonal Diverging Waves", © 2020 IEEE. Reprinted, with permission, from [36], its contents remain largely unchanged with minor modifications made throughout.

4.2 Introduction

Over the last decade, ultrafast ultrasound imaging has enabled large frame rate improvements and has made new imaging modes possible, such as shear-wave elastography [64], [150], ultrafast Doppler [109], functional ultrasound imaging [69], [71], and super-resolution imaging [78]. The most common approaches to ultrafast imaging are plane-wave imaging (PWI), diverging-wave imaging (DWI), synthetic aperture (SA), and multi-element synthetic transmit aperture imaging (MSTA), each

of which takes a different approach to the problem of insonifying a large field of view on each transmit event. Ultrafast images can be generated with as few as one insonification but using more insonifications improves SNR, dynamic range, and resolution. Resolution improvements are achieved by synthesizing a transmit focus from multiple transmit events, each with a different angular spectrum, performing dynamic beamforming on receive, and compounding the resulting frames together [80], [81], [151]. PWI, however, cannot be used to uniformly insonify a sector larger than the aperture, limiting its usefulness in phased array applications. This limitation was addressed by the introduction of diverging wave imaging, in which the target is insonified by a set of diverging waves, allowing a phased array transducer to image a field of view wider than the transducer aperture. In diverging wave imaging, virtual point sources are synthetically created behind the array using a sub-aperture of the array. To generate transmit events with different angular spectra, the virtual point source is repositioned behind the array [81], [83], [84]. Successive insonifications are then coherently compounded together to improve image resolution. Another method of generating a wide-field transmit insonification is the SA approach in which individual elements are pulsed one at a time [152]. This approach suffers from reduced SNR since only one element is activated with each insonification. To rectify this problem various solutions have been proposed such as multi-element synthetic transmit aperture (MSTA) [87], [88] and Hadamard encoding [101], [104], [105], [153], [154]. Under the MSTA framework, groups of adjacent elements are simultaneously activated for each insonification, and the transmit delay is calculated as though it originated from the center of the group of elements [87], [88]. Hadamard encoded MSTA (HMSTA) has been used to activate the full aperture with each insonification to increase SNR [104], [105], [154]. A variation of HMSTA where overlapping sub-

91

apertures are Hadamard encoded and a diverging wave profile is applied to each sub-aperture has been investigated in [101]. Instead of encoding elements or sub-apertures, multiplane-wave compounding Hadamard encoded plane waves staggered in time [102], [103]. Hadamard techniques make use of the properties of the Hadamard basis, an orthogonal basis comprised of vectors of either +1 or -1. The Hadamard basis vectors are often called Hadamard codes. In the Hadamard encoding scheme proposed by Chia et al. [104], each element in an N-element array is coded with either a $\pm 90°$ phase shift during transmission. The transmission events cycle over the Hadamard codes in the Hadamard basis. On a given transmit event, each element is excited with a pulse phase-shifted by $\pm 90°$ according to whether the element of the Hadamard code corresponding to the array element is +1 or -1 in the current code. Conventional dynamic beamforming is applied on receive. After N transmits, the received dataset will consist of one frame of channel data for each Hadamard code. By constructing linear combinations of these data frames, N different synthetic transmit apertures in which only one element is excited can be generated and conventional synthetic aperture beamforming can be applied to generate images. As compared to performing synthetic aperture imaging by only transmitting from one element at a time, the effective echo signal amplitude is increased by a factor of N and the SNR by a factor of $\sqrt{N}$ due to the encoding gain. Ceroici et al. have shown that the number of Hadamard codes can be decreased by selecting codes in which pairs of adjacent elements have the same polarization [105]. This technique reduces the number of insonifications required to form an image, but at the expense of larger effective element size and a larger element pitch. The larger element size results in reduced directivity and the larger element pitch can introduce grating lobes into the field of view. Liu et. al have shown that compressed sensing

can be used on HMSTA beamforming to reconstruct the full dataset at the expense of SNR for both linear arrays [155], and phased arrays [153]. In [153], Liu surfs HMSTA encoding on a diverging wave delay profile to improve directivity.

In this work, a new ultrafast imaging technique similar to that described in [153] is presented. This new method differs in that it does not require compressed sensing algorithms for decoding and a new method for inserting beamforming delays is introduced. Coined synthetic transmit-element delay insertion (STEDI), transmit delays are inserted from each transmit element instead of the center of the effective transmit aperture following Hadamard decoding. When less than a complete set of Hadamard codes are used, beamforming using STEDI improves SNR, grating lobe levels, and resolution compared to the conventional method. In this approach, the phases of array elements during excitation are quantized to $\pm 90°$ in the form of orthogonal Hadamard codes, while simultaneously being surfed on top of a diverging wavefront created by using the full aperture of the array from a single virtual point source. The sparse orthogonal diverging wave imaging (SODWI) method's suitability for phased array applications was evaluated by using it to generate tissue phantom images with a high-frequency 64-element phased array transducer. The array had a 40 MHz center frequency, 1 λ pitch, and was constructed using the procedure outlined in [12]. The results are compared to the imaging performance of other phased array imaging techniques including DWI, SA, HMSTA, and focused imaging. Other high frame rate imaging techniques such as single focal zone beamforming with multi-line acquisition (MLA) [156] were considered, but were ultimately excluded from this study since they do not produce transmit focusing at all depths.

4.3 Beamforming methodologies

In this chapter, common ultrafast imaging methods are described in more detail than chapter 2, and later compared to the SODWI method.

4.3.1 Synthetic Aperture Imaging

In SA imaging, each of the array elements is pulsed individually and the full aperture is used to receive. The transmit beamforming process can be modeled using equation (4.1), where T is the transmit matrix containing the transmit pulse and time delay applied to each element, Ψ, is the field transfer function from each transmit element to every location in the field of view and back to the receive elements, and R_S is a matrix containing the received channel data for each transmit event. Since SA only transmits with one element for each insonification, the transmit matrix, T is a diagonal matrix and each entry is identical, since no delays are applied.

$$T\Psi = R_S \tag{4.1}$$

$$\begin{bmatrix} T_1 & \cdots & 0 \\ \vdots & \ddots & \vdots \\ 0 & \cdots & T_N \end{bmatrix} \begin{bmatrix} \Psi_{11} & \cdots & \Psi_{1N} \\ \vdots & \ddots & \vdots \\ \Psi_{N1} & \cdots & \Psi_{NN} \end{bmatrix} = \begin{bmatrix} R_{S_{11}} & \cdots & R_{S_{1N}} \\ \vdots & \ddots & \vdots \\ R_{S_{N_1}} & \cdots & R_{S_{NN}} \end{bmatrix} \tag{4.2}$$

$R_{S_{ij}}$ is the receive data when transmitting on element i and receiving on element j. Two-way beamforming delays are applied to the vectors in the receive matrix R_S and then summed together for image reconstruction.

4.3.2 Hadamard Encoded Multi-Element Synthetic Transmit Aperture

When trying to improve frame rates by using fewer pulses than there are elements in the aperture, MSTA produces improved SNR over conventional SA by activating multiple adjacent elements simultaneously, instead of activating one element for each insonification. This method increases the size of the active array aperture for each pulse, increasing the transmitted pressure into the field. Many configurations are possible, but in this work, there is no overlap between successive transmit apertures and elements are grouped into sets of 1, 2, 4, 8, and 16 elements, resulting in 64, 32, 16, 8, and 4 transmit pulses respectively.

To further improve SNR, the groupings of elements can be Hadamard encoded so that the entire array is activated simultaneously. HMSTA requires that a full set of Hadamard encoded pulses are transmitted across successive insonifications. A complete set of orthogonal basis codes is defined by N Hadamard codes where N is the number of array elements. To achieve a sparser set of transmit events, the number of Hadamard codes used can be reduced by a factor of two by only keeping those codes in which adjacent pairs of elements have the same sign. For example, in the set of codes for N=4, [1,1,1,1], [1,1,-1,-1], [1,-1,-1,1], [1,-1,1,-1], a sparse set of two codes can be obtained by only taking the first two codes in which neighboring pairs of elements share the same sign. This reduction amounts to pairing adjacent elements which effectively produces larger elements on transmit. Importantly, though, both the beamforming delays used for transmit and receive beamforming are applied separately to each element. The reduction process can be repeated to further reduce the number of codes used, effectively doubling the element size and pitch and

95

halving the number of insonifications with each factor of two reduction in the number of codes.

A complete set of Hadamard codes is represented by a $N \times N$ matrix H containing a Hadamard code on each row. A sparse set of codes will contain $N/2^m$ codes where m is the number of times the codes have been reduced by a factor of two by pairing adjacent elements. As in equation (4.1) for SA, the receive data R can be represented by

$$HT\Psi = R \qquad\qquad (\,4.3\,)$$

where H is the $N \times N$ Hadamard encoding matrix, T is the diagonal transmit pulse matrix from equation (4.1), and Φ is the two-way field transfer function from each transmit element through the field and back to each receive element. Decoding is performed by multiplying the received data by H^T as shown in (4.4). After decoding, the receive dataset used for beamforming can be obtained from (4.5). The decoded receive data, R', is arranged such that its ith and j^{th} entries, R'_{ij}, correspond to the decoded receive data when transmitting from element i and receiving on element j. Two-way beamforming delays are then applied to the decoded receive matrix R' for image reconstruction.

$$NIT\Psi = H^T R \qquad\qquad (\,4.4\,)$$

$$H^T R = R' = \begin{bmatrix} R'_{11} & \cdots & R'_{1N} \\ \vdots & \ddots & \vdots \\ R'_{N1} & \cdots & R'_{NN} \end{bmatrix} \qquad\qquad (\,4.5\,)$$

After decoding, the dataset is identical to the dataset one obtains from SA imaging except that the signal strength is increased by a factor of N. Alternatively if the number of codes is reduced to $N/2^m$, the decoded data is representative of

having excited adjacent elements together, as in MSTA, yielding a signal gain of $N/2^m$ over MSTA. Let H_s denote a sparsely selected Hadamard matrix. The decoding process is now defined by (4.6). $H_s{}^T H_s$ produces a block diagonal matrix instead of an identity matrix since adjacent elements are provided identical codes and are therefore encoded together. The decoded receive data is thus representative of having performed synthetic aperture transmit beamforming where adjacent elements are pulsed simultaneously instead of independently. SA beamforming delays can now be applied to this decoded receive dataset.

$$H_s{}^T H_s T\Psi = H_s{}^T R \qquad\qquad (\ 4.6\ )$$

4.3.3 Diverging Wave Imaging

Two variations of DWI are investigated. In the first approach (DWI (I)), each insonification is generated by applying delays to the array elements corresponding to emissions from a virtual point source located behind the array. Only a subset of array elements forming a sub-aperture insonify the target on any given transmit event. The point source location is translated laterally across different transmit events by changing the beamforming delays and the transmit sub-aperture. Each lateral translation of the point source is 1 λ or the element pitch. In comparing DWI (I) with SODWI, DWI (I) is considered while using 32, 16, 8, and 4 virtual point source locations. Using 64 virtual point sources is not considered since the aperture size for 64 virtual point sources is 1-element wide for this configuration, making it functionally equivalent to SA. In each DWI (I) configuration used for this investigation, the transmit aperture size, a, is maximized for each configuration to

97

deliver the highest possible DWI pressure. The transmit apertures are symmetric about the virtual point sources and run along the extent of the array. As the number of virtual point sources, n_{vp} decreases, the transmit aperture size a increases, and the distance between the virtual point source and the array increases so that the divergence angle is held constant. The relationship between the number of virtual point sources and the number of elements in the transmit aperture is described by (4.7), where N is the number of elements in the array. The relationship between the divergence angle, the virtual point sources, and the transmit aperture is described in [81] and is set to $90°$ for this investigation.

$$a_{ap} = N - n_{vp} + 1 \qquad\qquad (\ 4.7\ )$$

The second DWI technique, DWI (II), follows a similar approach to that taken in [84]. The virtual point source behind the array is rotated at various tilt angles, α. A maximum tilt angle of $25°$ is used and the radial distance between the point source and the center of the array, r_{vp}, is held constant. r_{vp} is calculated by setting the divergence angle between the full aperture and the virtual point source to be $90°$ for a tilt angle of $0°$. Similarly, to DWI (I), DWI (II) is compared to SODWI when using 4, 8, 16, and 32 diverging waves. For each scheme, the tilt angles are equally spaced between $\pm 25°$ and the full aperture is used with each pulse.

4.3.4 Sparse Orthogonal Diverging Wave Imaging (SODWI)

SODWI is a variation of HMSTA where a diverging wave beamforming delay profile is applied to the transmitted wavefront to distribute energy across a much wider field of view, as shown in Fig 4.1. When using a sparse Hadamard basis and a

diverging wave delay profile, the reduction of the set of codes used and the resulting effective increase in element pitch creates the possibility of introducing grating lobes into the image. To mitigate this effect, a method of receive beamforming that introduces a minimum in the receive point spread function at the same location as the transmit grating lobes is used, resulting in an acceptable two-way grating lobe level. Fig 4.2 (a) illustrates what we have termed the 'STEDI' method used for calculating and applying beamforming delays when neighboring elements are grouped during transmit. The shaded elements are those elements that are paired together during transmit. The beamforming delays are inserted separately for each element as though each element was pulsed independently as shown in Fig 4.2 a). Using this convention, even though the transmitted wave from each element is inseparable since they were encoded together, the RF data is reused so that the beamforming delays corresponding to each of the grouped elements are individually inserted. Normally the receive delays would be calculated based on the TOF from the center of the grouped elements as shown in (b) of Fig 4.2. The total TOF delay for this approach considers the delay from the center of the grouped element to a point in space and back to any other element on the array. However, using this approach, the element pitch of the transmit aperture is now twice that of the original pitch, which introduces grating lobes into the field of view.
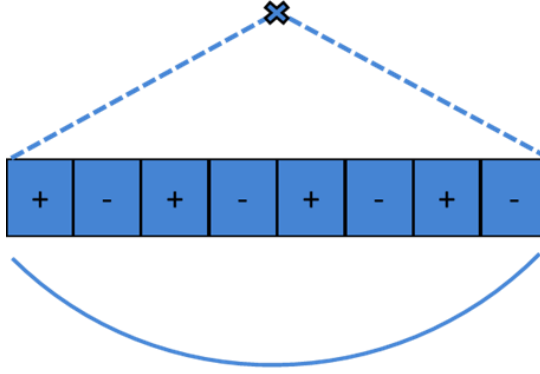
Fig 4.1 An insonification using Hadamard modulation of a diverging wave in SODWI. The beamforming delays focus to a virtual point source located behind the imaging aperture and each element has its phase adjusted according to the current Hadamard codes in a sequence.
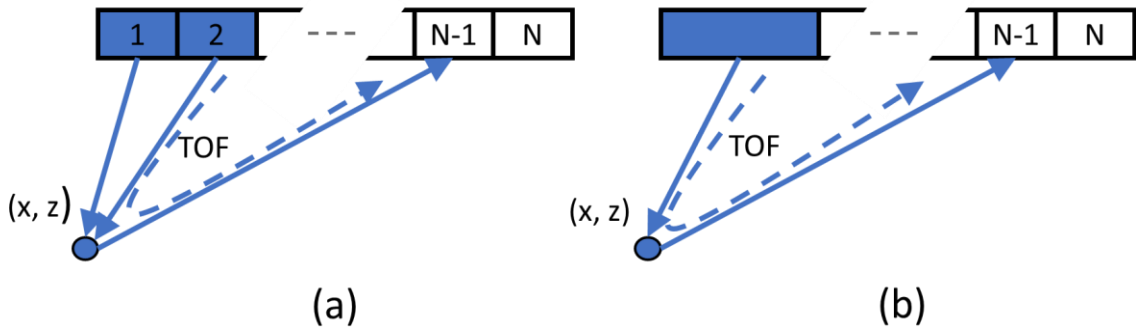
Fig 4.2 A comparison of two possible synthetic-aperture beamforming schemes: (a) STEDI - both elements are excited, and the beamforming delays are calculated from the center of each of the activated elements to a point in space and back to each receive element, (b) both elements are simultaneously excited and the beamforming delays are applied for the TOF from the midpoint between the active transmit elements back to each receive element.

A Field II simulation [46] of a 64-element 40 MHz phased array with a $\lambda/2$ element pitch illustrates the introduction of grating lobes when the effective transmit aperture pitch is increased by grouping adjacent elements into groups of two. In Fig

4.3 the beamforming delays for both STEDI and conventional beamforming are applied to RF data when: focusing on a point target, and the associated grating lobe region. The point target is placed at a 4 mm (f-number = 1.6) distance from the array and positioned at **35°** relative to the center of the aperture. When two-way beamforming delays are inserted into the RF data as in Fig 4.2 (b), with the effective transmit location being at the center of the grouped elements, focusing to the point target aligns the pulse echoes across various transmit events, but there is also constructive interference of the echo signals in the grating lobe region as shown in Fig 4.3 (a)-(b). Alternatively, when using the STEDI method, focusing at the point target is preserved, but the pulse-echoes destructively interfere in the grating lobe region, as shown in Fig 4.3 (c)-(d). As a result, grating lobes are suppressed in the two-way image and do not present an obstacle using this approach. To further illustrate this advantage, the lateral point spread functions for these methods are shown in Fig 4.4. The curves compare the two multi-element synthetic transmit aperture beamforming schemes, clearly illustrating that grating lobes degrade the beam profile when elements are beamformed conventionally as opposed to using STEDI beamforming. The same approach can be used in the more sparsely encoded Hadamard matrices where larger groupings of elements are used such as 4, 8, and 16 elements. For the remainder of this work, SODWI is only presented using STEDI beamforming since the aggravated grating lobes on the 1 λ pitch array used in this work render the image quality so poor that it is unusable without.
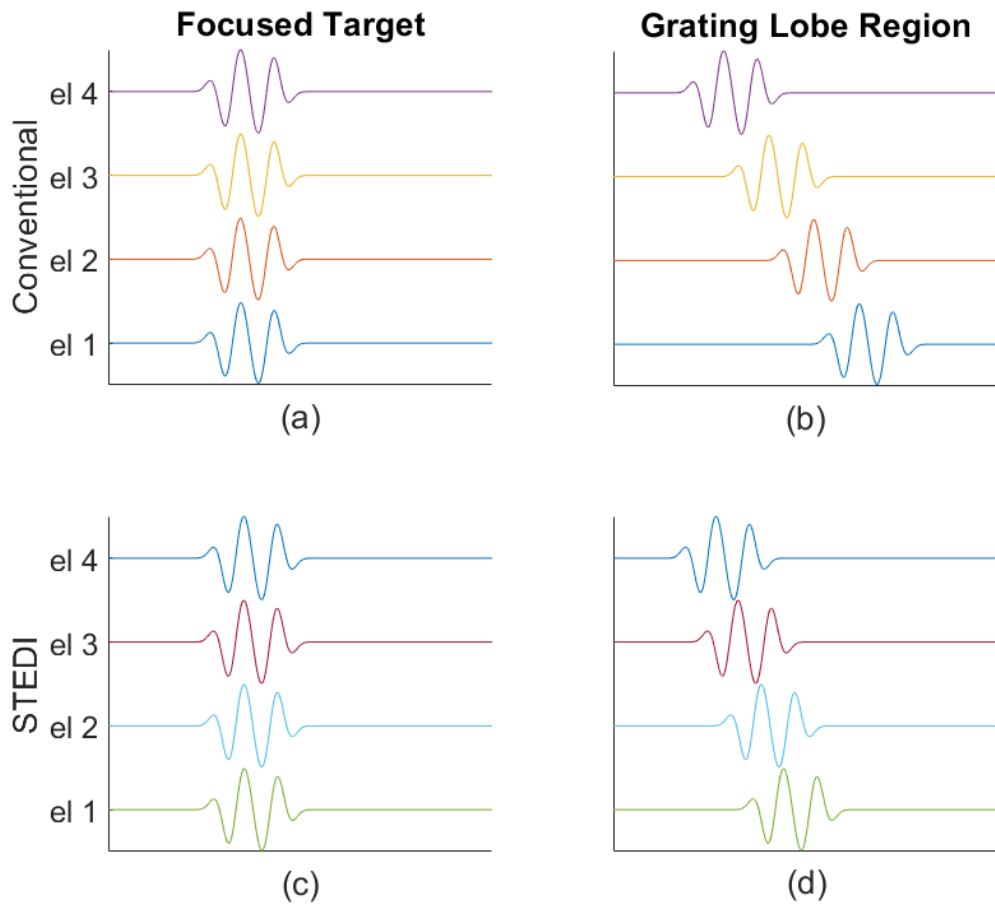
Fig 4.3 Beamforming delays applied to simulated RF using a conventional beamforming strategy where the delays are calculated from the center of grouped elements (a)-(b), and where beamforming delays are calculated from each of the individual elements grouped during encoding using STEDI (c)-(d). (a) and (c) are zoomed in on point target signals. (b) and (d) are zoomed in on the associated grating lobe region. Constructive interference occurs at the focus for both methods, however (b) exhibits constructive interference in the grating lobe region, whereas (d) exhibits predominantly destructive interference in the grating lobe region.
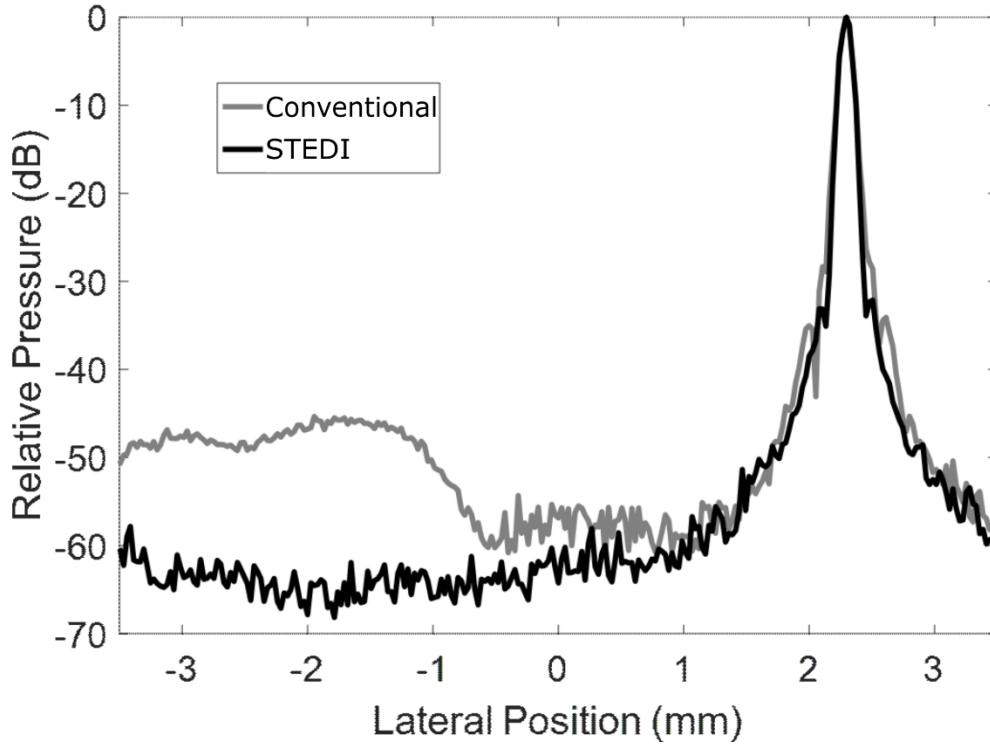
Fig 4.4 A comparison of the synthetic beamforming schemes used on sparsely encoded datasets.

Field II simulations were conducted for $\frac{N}{2^m} = 64, 32, 16, 8,$ and 4 Hadamard codes where a point target was positioned at 4 mm (f-number = 1.6) for each image line. The peak beamformed receive signal for each line was recorded when imaging a point target positioned on the same image line. This was used to generate two-way directivity plots as shown in Fig 4.5 (c). Similarly, the directivity plots for HMSTA and STEDI-HMSTA are plotted in Fig 4.5 (a)-(b). This plot illustrates the need for applying a diverging wave transmit delay profile for phased array applications, as the energy transmitted to wide angles is severely diminished when fewer than 64 transmissions are used. It also shows the power of STEDI to improve the beamformed signal level over conventional beamforming delays.
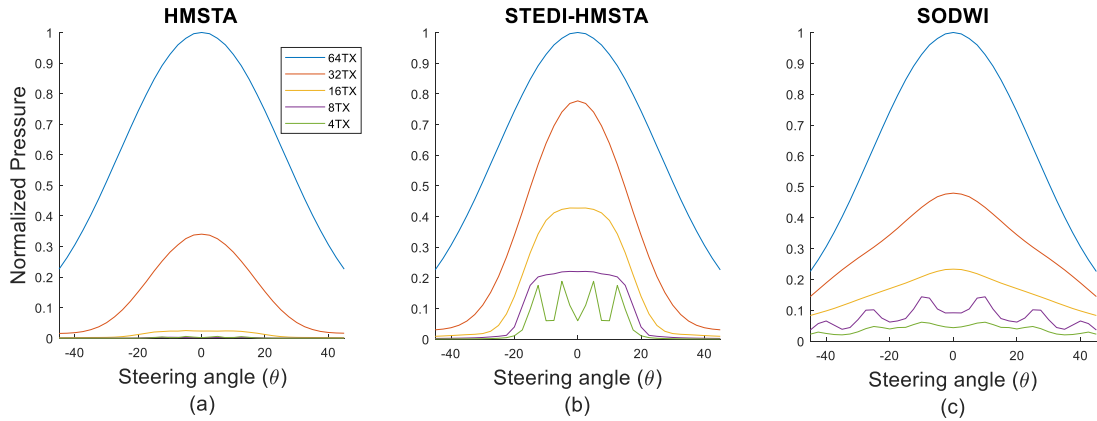
Fig 4.5 Normalized two-way directivity plots showing the peak beamformed receive signal when imaging a point target swept across imaging lines. The two-way directivity for HMSTA is shown in (a), STEDI-HMSTA is shown in (b), and SODWI is shown in (c).

4.3.5 Focused Beamforming

A focused transmission scheme with 4 transmit focal zones centered at 3.8, 4.7, 6.4, and 7.8 mm (f-numbers: 1.5, 1.9, 2.6, and 3.2) depths plus dynamic receive beamforming was used between 3 and 10 mm (f-number 1.2 to 4). This was repeated at 128 steering angles totaling 512 transmission events. This provides a conventional gold standard imaging benchmark to assess the beam profiles, contrast, and SNR obtained with SODWI, HMSTA, and DWI.

4.4 Theoretical Simulations

Field II simulations [46] were used to model the point spread-functions for a 64-element 40 MHz phased array with 1 λ element pitch, matching the parameters for the imaging array used in the verification experiments.

4.4.1 Point Spread-Functions

For high-quality imaging, axial resolution, lateral resolution, grating-lobe levels, and sidelobe levels are all useful metrics in evaluating the focusing capabilities of different beamforming strategies. Point spread functions for SODWI, STEDI-HMSTA, HMSTA, DWI (I), DWI (II), SA, and focused imaging were modeled by placing a point target at a 6 mm depth (f-number = 2.5) and steered to **25°** in front of the imaging array. Focused imaging provides a gold standard beam profile which helps illustrate the focusing trade-off when unfocused transmit imaging is used. Fig 4.6 and Fig 4.7 show the 2-D point spread functions for the Hadamard encoded schemes (SODWI, STEDI-HMSTA, and HMSTA), and the DWI schemes respectively. All images are plotted with 60 dB of dynamic range. For the Hadamard encoded schemes, 4, 8, 16, 32, and 64 insonifications are plotted for SODWI, STEDI-HMSTA, and HMSTA. This illustrates the difference when a complete set of Hadamard codes is used, compared to higher frame rate strategies where a reduced number of codes are used. For DWI, 4, 8, 16, and 32 insonifications are plotted to show the imaging performance of these approaches at the same frame rates used for the Hadamard encoded schemes.
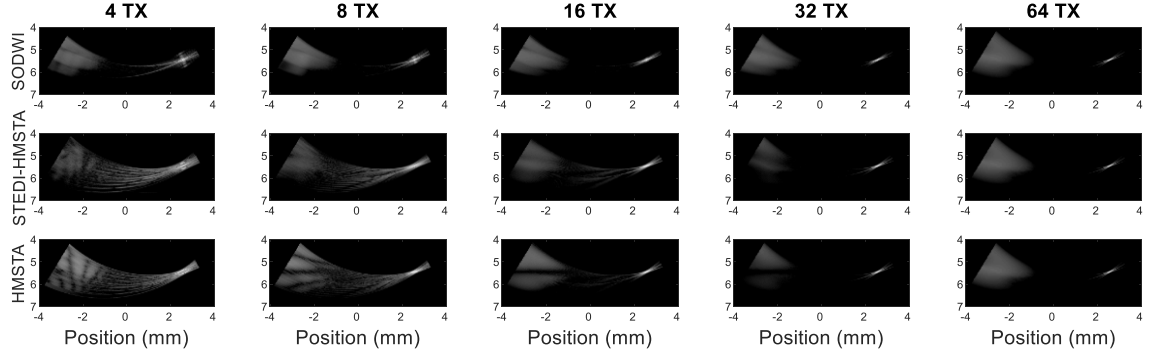
Fig 4.6 Point spread functions of SODWI, STEDI-HMSTA, and HMSTA. A point target is placed at a **25°** steering angle at a 6mm depth.
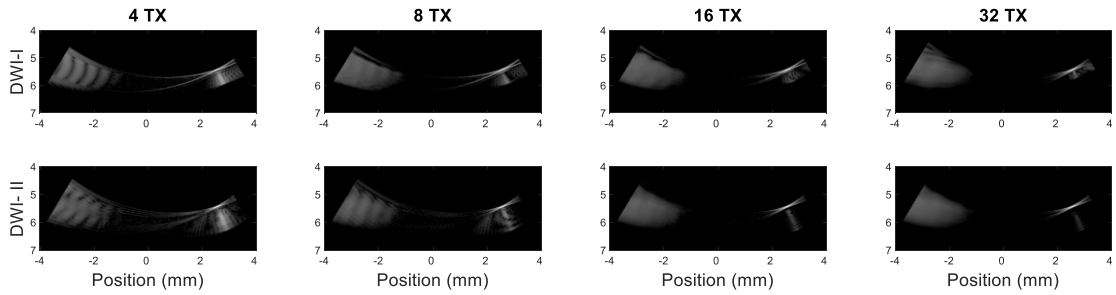
Fig 4.7 Point spread functions for diverging wave imaging using scheme (I) and (II). A point target is placed at a **25°** steering angle at a 6mm depth.

The -6 dB axial and lateral resolutions, as well as the grating lobe and sidelobe levels for all methods, are summarized in Table 4.1. SODWI exhibits improved resolution and sidelobe levels compared to STEDI-HMSTA and HMSTA. The grating lobes levels for SODWI are slightly higher than STEDI-HMSTA and HMSTA when 64 insonifications are used. Otherwise, STEDI-HMSTA produces the lowest grating lobe levels of these 3 methods and SODWI has superior grating lobe performance over HMSTA for 4, 8, and 16 insonifications, with HMSTA having the edge with 32 insonifications. The DWI methods exhibit similar sidelobe and grating

lobe levels to SODWI, with DWI taking a slight edge in most instances, but SODWI produces much better axial and lateral resolution in almost all instances (see Table 4.1 for specific details). It should be pointed out that when implemented in a practical system, a grating lobe suppression algorithms such as sign coherence imaging could easily be implemented [38], [62], [91], [92].

Table 4.1 Simulated Point Spread Function Measurements

Scheme	Axial Resolution (μm)	Lateral Resolution (μm)	Grating Lobe Level (-dB)	Sidelobe Level (-dB)
SODWI 4	60.1	120.5	34.9	47.9
SODWI 8	59.4	123.5	34.2	58.4
SODWI 16	62.5	120.5	35.5	58.9
SODWI 32	59.4	117.4	36.2	63.7
SODWI 64	52.7	115.3	36.4	68.3
STEDI-HMSTA 4	66.5	161.2	37.1	31.5
STEDI-HMSTA 8	69.4	170.1	40.0	39.2
STEDI-HMSTA 16	81.6	191.2	40.3	48.1
STEDI-HMSTA 32	61.1	147.8	41.9	61.0
STEDI-HMSTA 64	52.7	115.4	36.3	67.0
HMSTA 4	120.3	126.6	26.6	35.0
HMSTA 8	74.7	269.6	29.7	41.7
HMSTA 16	76.6	211.0	34.7	50.8
HMSTA 32	56.1	138.5	39.9	61.8
HMSTA 64	52.7	115.4	36.3	67.0
DWI 4 (I)	64.6	153.3	30.3	50.4
DWI 8 (I)	64.7	153.1	35.2	54.8
DWI 16 (I)	64.8	151.6	36.5	60.1
DWI 32 (I)	63.6	144.1	35.7	63.8
DWI 4 (II)	60.3	144.3	32.8	49.0
DWI 8 (II)	61.3	146.2	35.8	52.9
DWI 16 (II)	61.5	146.8	36.7	57.7
DWI 32 (II)	61.7	147.2	37.0	64.5
SA	52.7	115.4	36.3	67.0
Focused	51.3	112.8	36.6	72.0

In the axial dimension, Fig 4.6 shows that as the number of insonifications or Hadamard codes is reduced to 4 and 8, the pedestal levels for SODWI increase to a higher level on both the proximal and distal sides of the point source, whereas a complete set of codes produces an axial beam profile without pedestals. Fig 4.7 shows a similar pedestal increase for the axial beam profile for DWI (I) and (II). For DWI the pedestal is only increased on the distal side of the point target. The increased pedestal level for SODWI is caused by the inter-signal interference that is captured when beamforming data containing the transmitted wavefronts from adjacent elements that were encoded together. For DWI, previous work from [157] suggests the 'ghosting' effect is associated with signals emitted from elements that do not perfectly overlap with the overall wavefront used to calculate the beamforming delays.

4.4.2 Signal-to-Noise Ratio

SNR is another important metric for evaluating ultrafast imaging performance. SODWI, STEDI-HMSTA, HMSTA, DWI (I), DWI (II), SA, and focused imaging were simulated by imaging a random distribution of point targets (modeling a tissue phantom). The simulated region was limited to between 5 and 7 mm (f-number: 2.1 to 2.9) of imaging depth and steering angles ranged over $\pm 32°$. 128 lines were used, and 200 axial pixels were used for each angle. The imaging window was populated with 5000 randomly placed targets with random scattering amplitudes. Images were generated using each imaging technique to estimate the receive signal amplitude obtained from the method. The receive signal amplitude was then averaged across all depths and image lines to simplify the comparison between each method. To

estimate the beamformed noise, 1mV RMS of noise was injected into the simulated RF data before beamforming.

Fig 4.8 compares the average simulated SNR throughout the image window for each method. SNR drops with increasing depth, but the relative differences between imaging techniques in decibels remain constant with depth. Since the number of insonifications for SA and focused imaging are fixed, their SNR levels appear as horizontal lines on the plot to help illustrate the relative differences between the techniques. The SA method requires 64 insonifications and is equivalent to DWI (I) with 64 transmissions. For the DWI methods, in addition to simulating with $n = 4, 8, 16$ and 32 transmit events, an additional simulation was performed with 48 transmit events to demonstrate that as the number of transmit events increases past 32, the SNR drops for DWI (I) due to the decreasing utilization of the transmit aperture. In the limit of 64 transmit events, DWI (I) is equivalent to SA with each virtual point source corresponding to an array element. In this case, only $1/64^{th}$ of the aperture is used on each transmit event, and the SNR is the lowest of any of the methods studied. The SNR of SODWI, STEDI-HMSTA, HMSTA, DWI (I), DWI (II) and focused methods are expressed in dB relative to this minimal SNR level achieved by SA. The simulation results from Fig 4.8 show that the higher transmit aperture utilization creates a 2.5 and 5.7 dB improvement in SNR for DWI (II) compared to DWI (I) when 32 and 48 insonifications are compounded. The Hadamard encoded schemes also utilize the full aperture, and display SNR improvements over both DWI schemes, but more substantially so for DWI (I). When comparing the Hadamard encoded schemes, despite the poor directivity of STEDI-HMSTA, it yields the highest SNR when the signal across all lines are averaged together. The increased pressure delivered to the center of the field of view

compensates for the absence of energy delivered to wide angles. STEDI-HMSTA provides improved SNR over HMSTA when less than N codes are used, and SODWI provides an SNR improvement over HMSTA when 4, 8, and 16 codes are used.
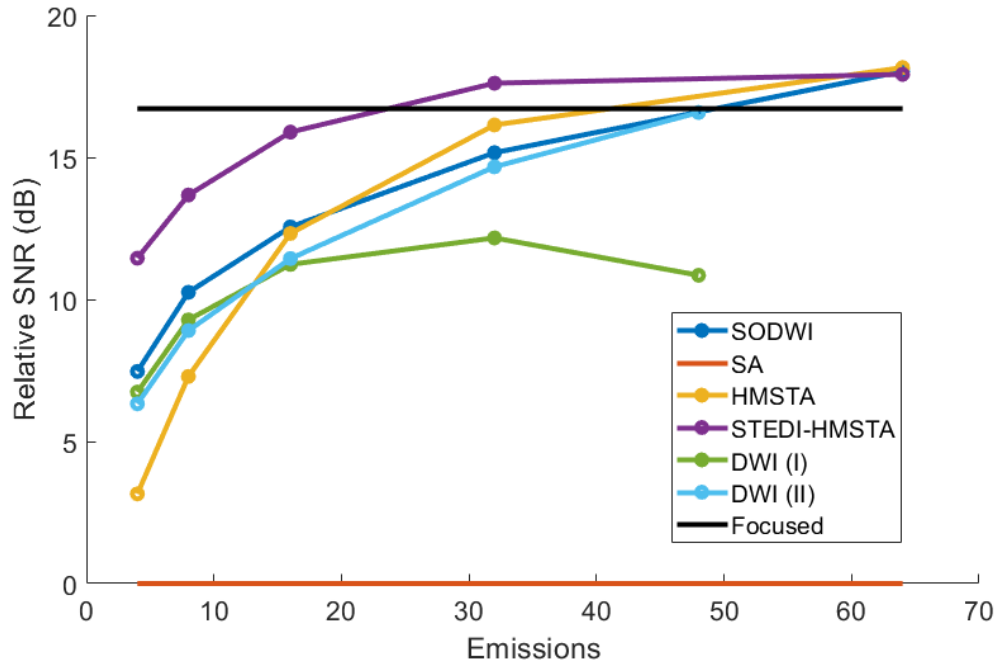
Fig 4.8 Simulated relative SNR comparison between SODWI, SA, HMSTA, STEDI-HMSTA, DWI-I, DWI-II, and focused imaging.

4.5 Experimental Setup

4.5.1 Hardware Setup

To evaluate their performance in a practical implementation, the SODWI, HMSTA, STEDI-HMSTA, DWI (I), DWI (II), SA, and focused beamforming methods were implemented on the beamforming platform described in Chapter 3 which was reconfigured to capture channel data. All 64 RF channels are captured in

parallel with 12 bits of resolution. Data from all of the acquisition cards are then transferred to a motherboard and then to a PC through a USB-3.0 interface. The motherboard synchronizes the acquisition across all boards and controls the pulse repetition interval by triggering the transmit beamforming module. Channel data for 64 insonifications can be stored on the hardware at once. The transmit pulse interval is **25 μs** so that when insonifying with 64, 32, 16, 8, and 4 waves, the system's frame rate is 0.625, 1.25, 2.5, 5, and 10 kHz respectively. Receive beamforming and image reconstruction was performed in post-processing in MATLAB. No apodization was applied to any of the beamforming strategies examined except for DWI (I), where a sub-aperture is used for each insonification as described by equation (4.7).

4.5.2 Imaging Array

A 64-element 40 MHz phased array built onto a high-dielectric PZT substrate (3257HD, CTS, Illinois, US) was used for the experiments. The array is similar in construction and performance to the one described in [10]. Three elements on the array were found to have open-circuit connections from imperfect manufacturing. To miniaturize the probe packaging, the 40 MHz array used in this study has a 1λ element pitch and 64 elements. Any decrease in pitch would increase the number of elements and in turn the size of the interconnect/packaging. Grating lobes are therefore present at wide viewing angles. For this reason, the imaging field of view is limited to **±32°** so that grating lobe artifacts are limited. This field of view is narrower than most conventional phased arrays but still provides a wide field of view suitable for many endoscopic imaging applications.

4.5.3 SNR Measurements

Average depth-dependent signal strength was measured from a homogeneous gelatin tissue phantom constructed according to the procedure outlined in [149]. The depth-dependent signal was calculated by averaging the RF data across all image lines from the sector scan and averaging across 20 frames to remove motion artifacts caused by vibration of the imaging fixture. Similarly, the noise floor for each imaging technique was calculated on a depth-dependent basis in the absence of scatterers. As described in equation (4.8), SNR is the ratio between the depth-dependent signal amplitude, S_{sig}, and the depth-dependent noise amplitude, S_n, expressed in decibels.

$$SNR = 20 \log_{10} \frac{S_{sig}}{S_n} \qquad (4.8)$$

4.5.4 Contrast Measurements

To evaluate the imaging performance of the various beamforming methods, the contrast between an anechoic void and surrounding homogeneous tissue-mimicking phantom was measured. A silica/gelatin phantom was prepared following the procedure outlined in [149]. A custom 3D printed mold was used to position 18-gauge hypodermic needles (305196, BD, Franklin Lakes, New Jersey, US) in the phantom during curing. The needles were removed after the phantom was cured to create the anechoic voids. Contrast is calculated by comparing the signal amplitude in two circular regions, each with a radius of 0.5mm, one located inside the anechoic void, and the second positioned directly adjacent to the anechoic void in the surrounding scattering medium. The position of the probe and tissue phantom was

112

fixed in place for all measurements. Contrast is defined by equation (4.9) where *env* is the beamformed envelope amplitude of the image, and S_a and S_t denote the circular area inside the anechoic void and in the tissue phantom respectively.

$$C = 20 \log_{10} \frac{\int_{S_t} env \cdot dS}{\int_{S_a} env \cdot dS} \qquad (\ 4.9\ )$$

4.6 Experimental Results

4.6.1 Signal-to-Noise

Fig 4.9 shows the SNR as a function of depth in a tissue-mimicking phantom for DWI (I), and DWI (II) for 4, 8, 16, and 32 virtual point source locations. Fig 4.10 shows the SNR in the same phantom for SODWI, STEDI-HMSTA, and HMSTA for 4, 8, 16, 32, and 64 Hadamard codes.
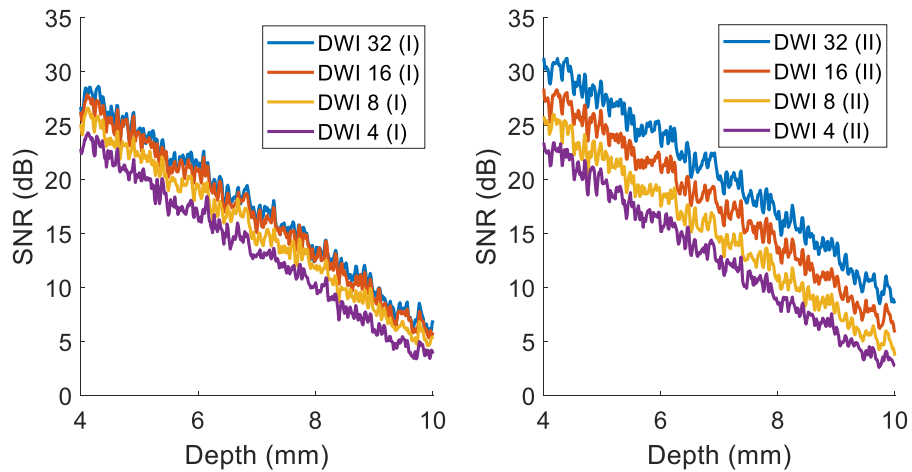
Fig 4.9 Measured SNR for DWI (I) and DWI (II) as a function of depth.
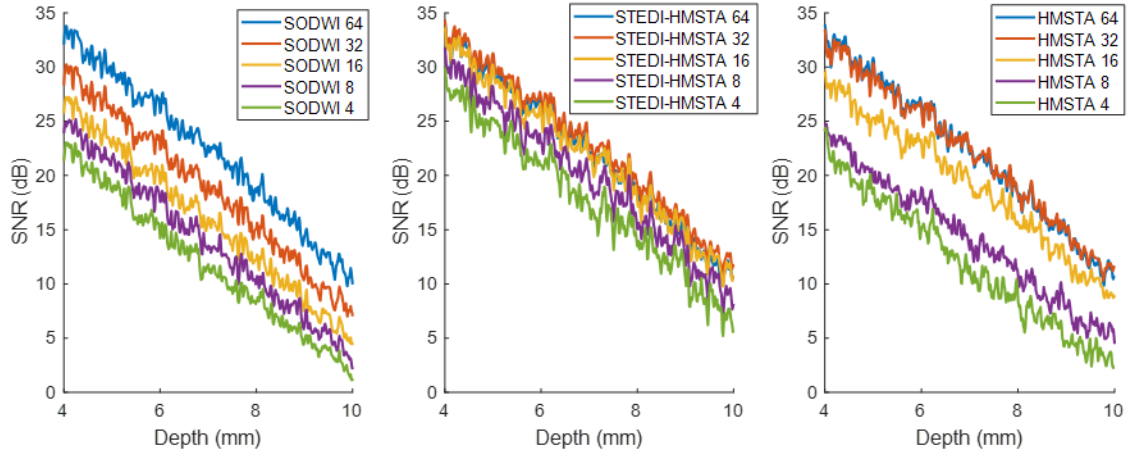
Fig 4.10 Measured SODWI, STEDI-HMSTA, and HMSTA SNR as a function of depth.

The SNR for DWI (I) depends on both the number of insonifications and the utilization of the available transmit aperture across the insonifications. In Fig 4.9, a doubling in the number of insonifications does not produce a $\sqrt{2} = 3dB$ improvement in SNR because of the decreased utilization of the transmit aperture associated with having more virtual point sources. For DWI (I), the SNR improves with increasing the number of insonifications up to a point and then begins to decrease toward the SNR level obtained with SA. Unlike DWI (I), DWI (II) shows a relatively constant improvement in SNR each time the number of virtual point sources used is doubled.

Similarly, for SODWI, increasing the number of insonifications increases the SNR as can be seen in Fig 4.10. For 64 codes SODWI yields identical SNR levels as STEDI-HMSTA and HMSTA, but SODWI produces lower SNR than these alternatives otherwise, except for 4 and 8 codes, where SODWI slightly outperforms HMSTA.

114

Fig 4.11 shows the average SNR across all depths for each beamforming method relative to the SNR level achieved with SA. Impressively, SODWI with 64 codes produces the highest overall average SNR at +16.6dB (relative to SA), marginally outperforming the focused case which achieves +14.8dB. SODWI also outperforms DWI (I) by +1.7dB when 32 pulses are used but performs worse than DWI (I) when fewer pulses are used. DWI (II), which takes advantage of the full transmit aperture outperforms SODWI with respect to SNR for all number of insonifications tested. The relative SNR data points from Fig 4.11 are listed in Table 4.2 for the reader's convenience.
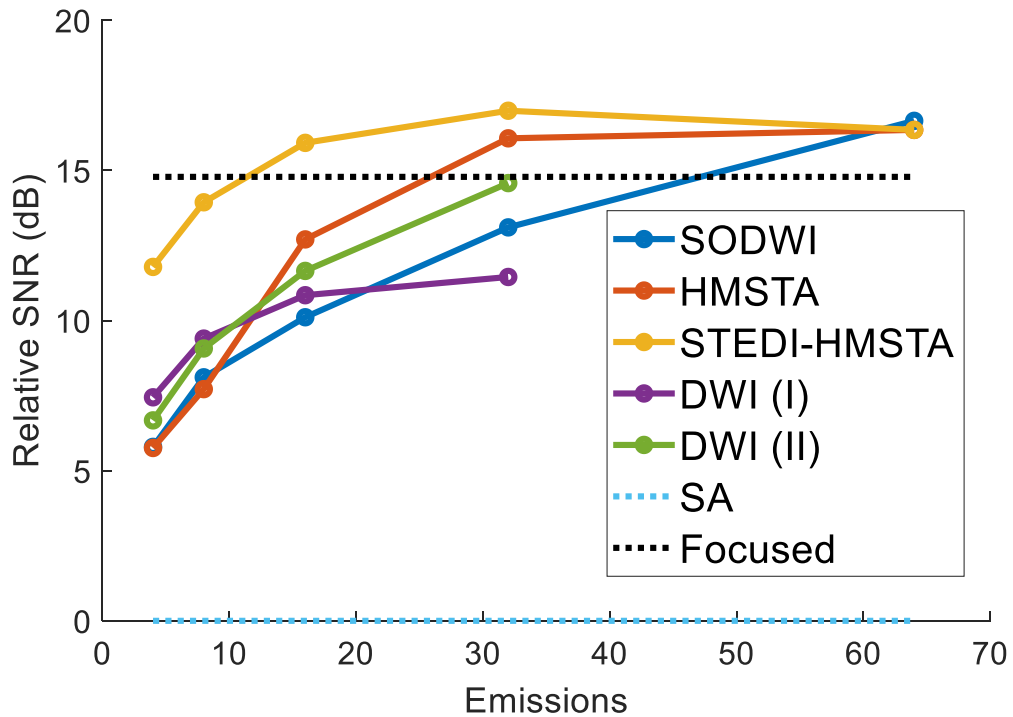
Fig 4.11 Measured relative SNR of SODWI, HMSTA, STEDI-HMSTA, DWI (I), DWI (II), SA, and focused imaging.

Table 4.2 Experimental SNR Relative to SA (dB)

# Transmits	4	8	16	32	64
SODWI	5.8	8.1	10.1	13.1	16.6
STEDI-HMSTA	11.8	13.9	15.9	17.0	16.3
HMSTA	5.8	7.7	12.7	16.1	16.3
DWI (I)	7.4	9.4	10.8	11.4	N/A
DWI (II)	6.7	9.0	11.7	14.6	N/A
SA			0		
Focused			14.8		

4.6.2 Contrast

It was found in the simulations of Chapter 4.4.1 that the point spread function improves with an increasing number of insonifications. The improved point spread function generally leads to higher contrast between the tissue and anechoic void regions of the phantom when the effects of SNR do not outweigh the focusing improvements. This trend is shown in the images in Fig 4.12, all of which are plotted with a 60dB dynamic range. Fig 4.12 (p) shows the focused case which has a contrast of 16.6dB. The focused image was generated with 128 focused lines and 4 transmit focal zones (512 insonifications). Fig 4.12 (a)-(e) shows the degradation in contrast for SODWI as the number of insonifications is reduced. When 8 and 4 insonifications are used, as shown in Fig 4.12 (d) and (e), the variations in directivity predicted by the simulation results of Fig 4.5 are apparent in the image. Fig 4.12 (u) shows the phantom imaged with SA. The well-defined boundary of the anechoic void demonstrates the high quality focusing achieved with this approach. However, despite its good focusing, SA produces only 8.3dB of contrast due to its poor SNR. Fig 4.12 (f)-(j) and (k)-(o) show STEDI-HMSTA and HMSTA. The image similarly falls off as the number of transmits is decreased, but more notably, the field of view

quickly deteriorates with almost no energy being delivered to wide angles. As a result of this narrowing field of view, the contrast measurements fall off dramatically for these approaches compared to SODWI. While the images of Fig 4.12 provide a qualitative comparison of the various imaging methods, Fig 4.13 provides a quantitative comparison. The SA and focused contrast values are plotted as horizontal lines to help benchmark the other curves. The Hadamard encoded techniques all produce 19.3dB of contrast for 64 transmits, but SODWI produces 18.1dB of contrast for 32 transmits, compared to 17.0 and 13.8dB for STEDI-HMSTA and HMSTA respectively. When only 4 transmits are used the contrast spread increases, with SODWI producing 11.2dB of contrast compared to -4.7 and -8.4dB for STEDI-HMSTA and HMSTA. Fig 4.12 (q)-(t) and (v)-(y) show the DWI (I) and DWI (II) contrast performance respectively. DWI (I) provides improved contrast compared to DWI (II), and yields similar contrast measurements to SODWI, with SODWI producing higher contrast than DWI (I) for 4 and 32 transmits, whereas DWI (I) produces higher contrast for 8 and 16 transmits. The data points from Fig 4.13 are presented in Table 4.3 to help the reader interpret the data.
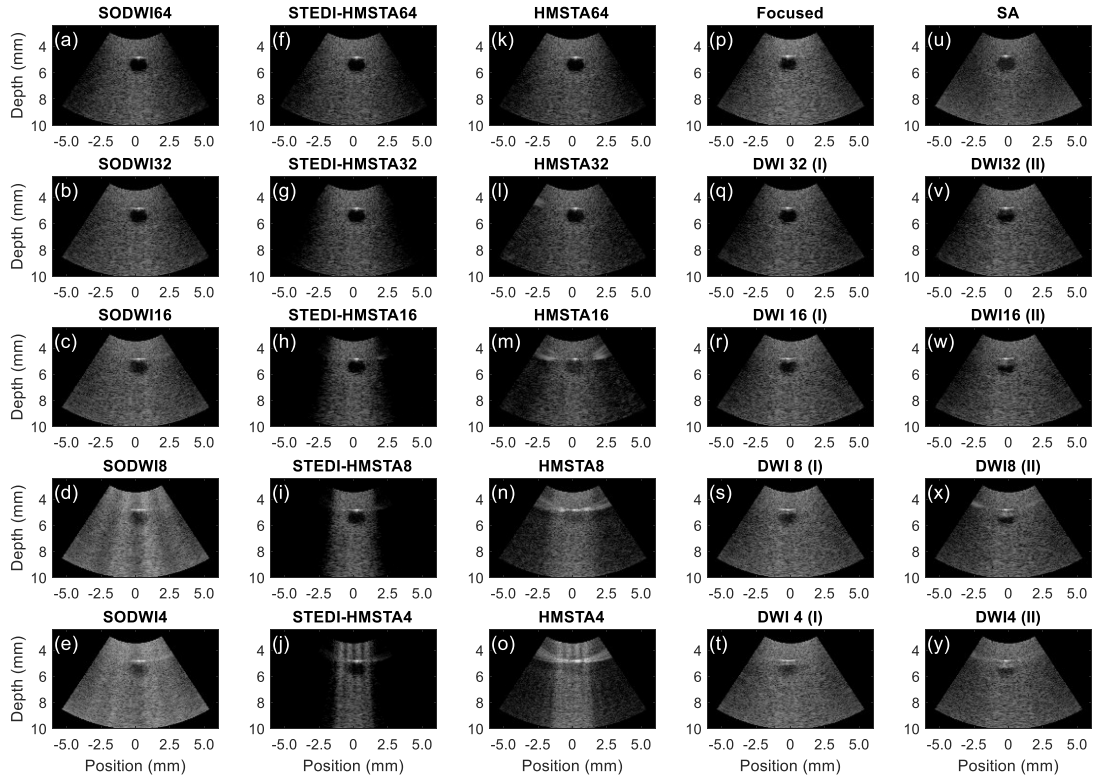
Fig 4.12 Experimental images of an anechoic void embedded in a tissue-mimicking phantom for various beamforming methods: (a)-(e) SODWI, (f)-(j) STEDI-HMSTA, (k)-(o) HMSTA, (p) focused imaging, (q)-(t) DWI (I), (u) SA, and (v)-(y) DWI (II). The subtitle for each subplot indicates the number of insonifications used to generate each image, the focused and SA cases required 512 and 64 insonifications respectively.
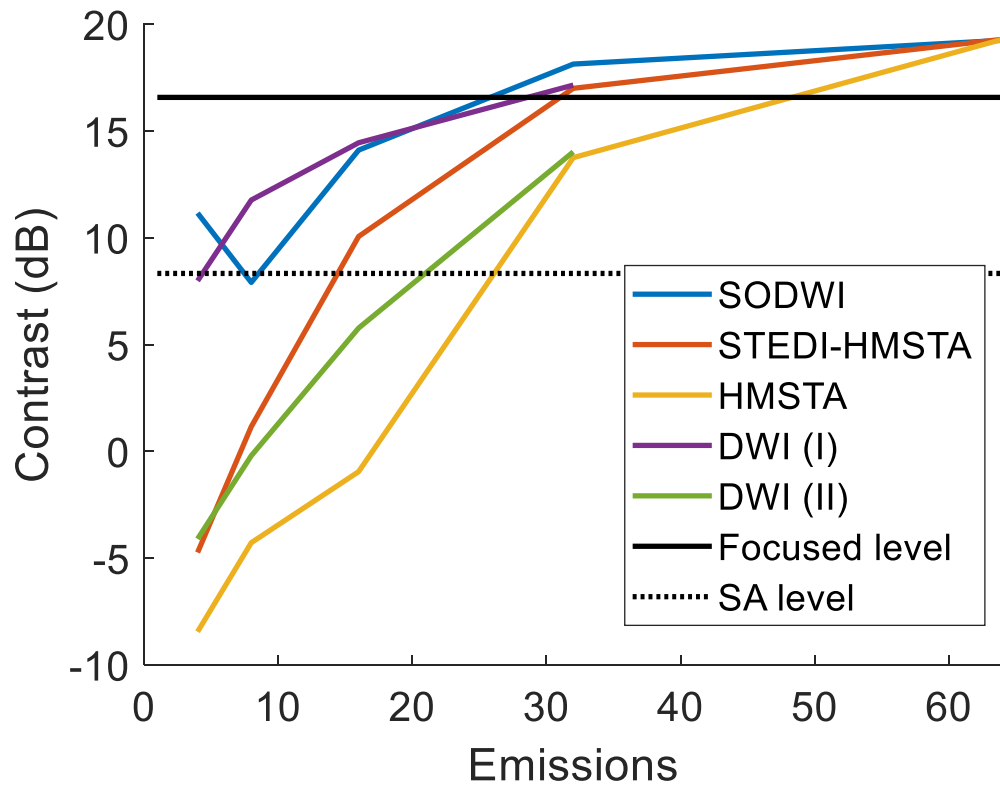
Fig 4.13 Contrast achieved during experimental imaging of an anechoic phantom for focused imaging, SODWI, STEDI-HMSTA, HMSTA, DWI (I), DWI (II), focused imaging, and SA.

Table 4.3. Contrast Measurements

# Transmits	4	8	16	32	64
SODWI	11.2	7.9	14.1	18.1	19.3
STEDI-HMSTA	-4.7	1.2	10.1	17.0	19.3
HMSTA	-8.4	-4.3	-1.0	13.8	19.3
DWI (I)	8.0	11.8	14.5	17.2	N/A
DWI (II)	-4.1	-0.2	5.8	14.0	N/A
SA			8.3		
Focused			16.6		

4.7 Discussion

Based on this study, it can generally be concluded that based on directivity, SODWI and DWI are the only serious candidates for phased array imaging to wide steering angles, where the other techniques have a prohibitive lack of sensitivity. The results also demonstrate the potential of SODWI to outperform conventional DWI for high frame rate phased array imaging under certain conditions. The experimental data shows that for a 64-element array with 32 and 64 insonifications SODWI outperforms DWI (I) with respect to SNR and contrast. When 16 or 8 insonifications are used, DWI (I) outperforms SODWI with respect to SNR and contrast. When 4 insonifications are used, SODWI yielded better contrast than DWI, but slightly lower SNR. When comparing SODWI to DWI (II) which uses the full transmit aperture, unlike DWI (I), DWI (II) yielded higher SNR than SODWI, but SODWI yielded higher contrast in all cases. This indicates that over a useful range of frame rates SODWI offers a substantial improvement over previously proposed ultrafast phased array imaging methods depending on the imaging application. In applications where SNR is of utmost importance, DWI (II) yields the best experimental results but does not produce the best contrast which is problematic for image quality. SODWI alternatively provides good contrast compared to DWI (II) and yields higher SNR than DWI (I) when a higher number of insonifications are used (32 and 64). The simulated point spread functions also show that SODWI exhibits improved lateral and axial resolution compared to DWI (I) and DWI (II), with the exception of SODWI 16, which exhibits worse axial resolution than DWI 16 (I) and DWI 16 (II). The improved axial resolution at the -6 dB point is only a few microns, between 0.2

to 9 μm. Concerning lateral resolution, SODWI provides 23.8 to 32.8 μm of improvement over DWI (I) and DWI (II).

While the experimental relative SNR curves from Fig 4.11 are generally well matched to the theoretical relative SNR curves from Fig 4.8, the improvement in SNR of SODWI over DWI (I) and DWI (II) expected from the simulations was not fully realized in the experiments. For SODWI 4, 8, 16, 32, and 64 the experimental SNR was 1.4, 2.0, 2.4, 2.1, and 1.6dB lower than the theoretical predictions. At the same time, the SNR performance of DWI (I) exceeded the theoretical prediction by 0.5 dB for DW (I) 4 but was 0.1, 0.5, and 0.9 dB lower than theoretical expectations when 8, 16, and 32 insonifications were used. DWI (II) matched the theoretical expectations with the experimental SNR discrepancies between simulated and experimental results being within 0.2dB of each other. Differences of -0.2, +0.0, -0.2, and 0.1 dB were measured between the theoretical and experimental results for DW (II) 4, 8, 16, and 32 respectively, whereby negative values indicate that the experimental SNR was lower than simulation, and positive values exhibited higher SNR than simulation. As a result of these discrepancies, the theoretical prediction that SODWI would exhibit better SNR than DWI (I) was only found experimentally for 32 insonifications, for which the expected improvement was largest.

There are a few possible reasons for this discrepancy between the simulations and the experiment. The array used in the experiments exhibited high mechanical crosstalk. The crosstalk was not captured by the Field II simulation which assumed acoustically isolated elements. Crosstalk could have a larger adverse effect on SODWI beamforming than on DWI because of the need to achieve good cancellation of signals across Hadamard codes in SODWI. Another possibility is that the

experimental data was affected by an inability to generate exactly inverted pulses in the Hadamard encoding process. This has been previously noted in the literature as a limitation of spatial Hadamard encoding [158] and would adversely affect SODWI and not DWI. Finally, 3 of the 64 elements in the array were open-circuited due to manufacturing defects. The Hadamard encoding/decoding process may be more sensitive to missing elements than DWI or focused ultrasound. The sum of these effects could easily explain the observed small discrepancies between experimental measurements and theoretical predictions. All these effects could potentially be remedied through improvements to the manufacturing process and to the system design in which case the experiments might agree more closely with the simulation results.

Regarding contrast, focusing performance and point spread functions play a much larger role than for SNR. When focusing deteriorates, the pulse energy is spread into a wider range of angles, causing more signal to appear in the anechoic regions of the image. This effect can be observed in the SODWI and DWI images of Fig 4.13. As fewer insonifications are used the pedestal levels in the axial and lateral planes increase and contrast decreases. From the simulated point spread functions in Fig 4.6, and Fig 4.7, it is expected that the deterioration of the axial point spread function when the number of insonifications is reduced will play a larger role in limiting contrast since the axial pedestal levels are higher than the lateral levels. Since contrast for SODWI 64 outperforms SA by 19.3dB, SODWI is the obvious choice for imaging schemes when frame rate requirements permit 64 insonifications per image frame. SODWI 32 also slightly outperforms DWI (I) 32 by 0.9dB and DWI (II) 32 by 4.1 dB. As the number of insonifications decreases and the pedestal level increases, DWI (I) begins to outperform SODWI with regards to contrast by

0.4 and 3.9dB for 8 and 16 insonifications respectively. When 4 insonifications are used, SODWI produces 3.2 dB better contrast. This reversing trend is likely an artifact of the variation in the directivity curve for SODWI 4, shown in Fig 4.6. Less signal energy is recovered from the center of the image which coincides with the position of the anechoic void. This results in an apparent improvement in contrast that would not persist if the void were located elsewhere in the image.

Comparing SODWI to STEDI-HMSTA and HMSTA provides valuable insight into the performance gains associated with using the STEDI method. Due to the lack of transmit energy to wide angles, STEDI-HMSTA and HMSTA are not good candidates for phased-array applications. These techniques produces very poor contrast measurements compared to the other techniques, except for DWI (II), where STEDI-HMSTA yields improved contrast. Despite the lack of energy delivered to wide angles, they yielded higher SNR results than the other imaging techniques when 16, 32, and 64 insonifications were used, and HMSTA performed poorly for 4 and 8 insonifications, however, STEDI-HMSTA produced the highest SNR of any technique irrespective of the number of insonifications used. Since the SNR measurements were averaged across image lines, the central image lines for STEDI-HMSTA and HMSTA were strong enough to raise the experimental curves above those of SODWI, DWI (I), DWI (II), and SA. Despite their lack of suitability for phased array applications, these results show that implementing STEDI significantly improves SNR for HMSTA imaging. STEDI-HMSTA produces a 6.0, 6.2, 3.2, and 0.9 dB improvement in SNR compared to HMSTA for 4, 8, 16, and 32 insonifications. Concerning resolution, SODWI yields superior axial resolution, lateral resolution, grating lobe levels, and sidelobe levels compared to HMSTA. The only exceptions

being that HMSTA 32 has slightly better axial resolution and a lower grating lobe level. For a detailed comparison refer to Table 4.1.

Ultrafast imaging applications exploit high frame rates to visualize or detect various phenomena such as shear wave propagation in elastography and blood volume changes in functional ultrasound. For the system used in this study, the PRF was 40 kHz. This high PRF is only possible at high frequencies where limited penetration keeps the imaging window depth short. The high PRF available in high-frequency imaging allows significant improvements in image quality through averaging and allows even higher frame rates than what can be achieved in ultrafast imaging at conventional lower frequencies. Using 64, 32, 16, 8, and 4 insonifications on the system yields frames rates of 625 Hz, 1.25 kHz, 2.5 kHz, 5 kHz, and 10 kHz respectively. A general rule of thumb for elastographic applications is to use rates >1 kHz [159], meaning that for this system, SODWI 32 can be used for elastography. The 625 Hz framerate achievable with SODWI 64 is also suitable for many dynamic imaging applications where it can yield high-resolution, contrast, and SNR. For lower frequency systems these PRFs are not possible due to the increased time-of-flight associated with increased tissue penetration. Low-frequency phased arrays often also have more elements and so a complete set of Hadamard codes will require more insonifications. As the time between codes and the number of codes increases, motion artifacts may begin to place limits on the ability to coherently decode the Hadamard encoded frames. For these reasons, SODWI will perform best in high-frequency ultrafast imaging applications, but may, nevertheless, find application in low-frequency systems as well. It is also of interest to compare the results herein to the work from [153] where compressed sensing was used to reconstruct the synthetic transmit aperture data (CS-STA). SODWI exhibits ripples in the transmitted

directivity when 4 or 8 transmits are used, whereas CS-STA does not exhibit this effect. However, when compared to STA, SODWI yields higher relative SNR than CS-STA. SODWI produced a 2.8, 1.5, 0.3, 0.3, and 1.3 dB higher SNR for 4, 8, 16, 32, and 64 transmits. Although these studies were done separately and many system factors could influence the results, this suggests that the SNR gain from STEDI exceeds that of reconstructing the RF data using compressed sensing. A future study directly comparing SODWI to CS-STA would shine further light on the trade-offs between these methods.

Nevertheless, the image quality obtained with SODWI 64 outperforms conventional focused imaging with regards to both SNR and contrast. The advantage is clearly visible when comparing the rat brain images captured using focused imaging (Fig 4.14), and SODWI 64 (Fig 4.15). The images show a coronal view of the right side of the midbrain with the cortex in view. Fig 4.14 is displayed with 40dB of dynamic range and contrast between the brain tissue the cerebral spinal fluid aqueduct is not nearly as pronounced as in Fig 4.15, despite this image being displayed with 60dB of dynamic range. No image processing was applied to either image.
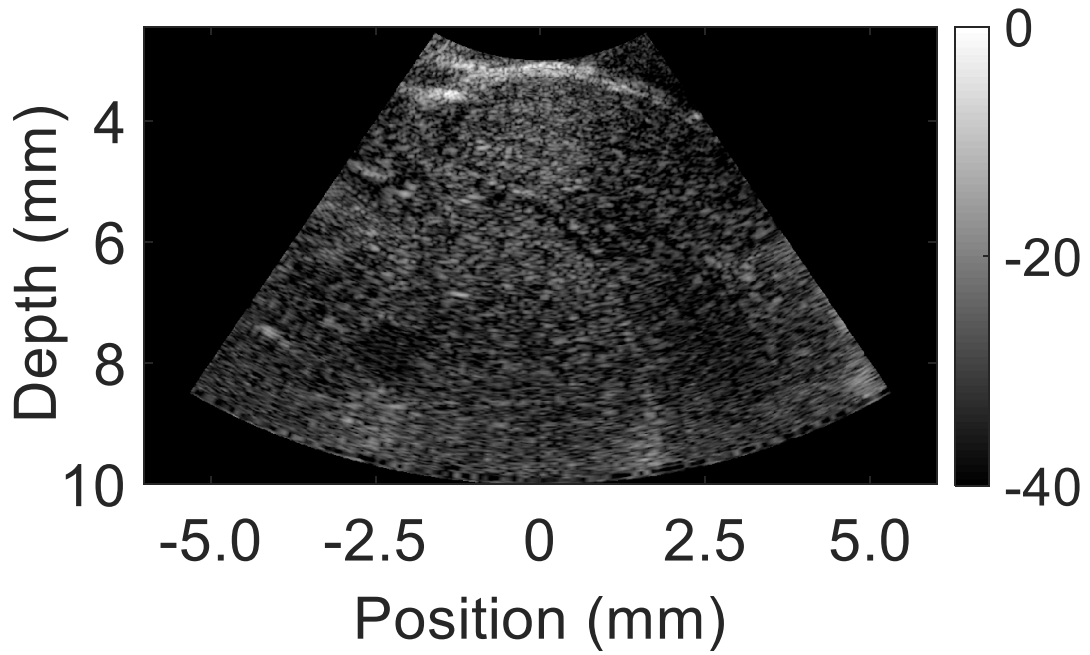
Fig 4.14 An in-vivo rat brain image captured using a focused imaging scheme.
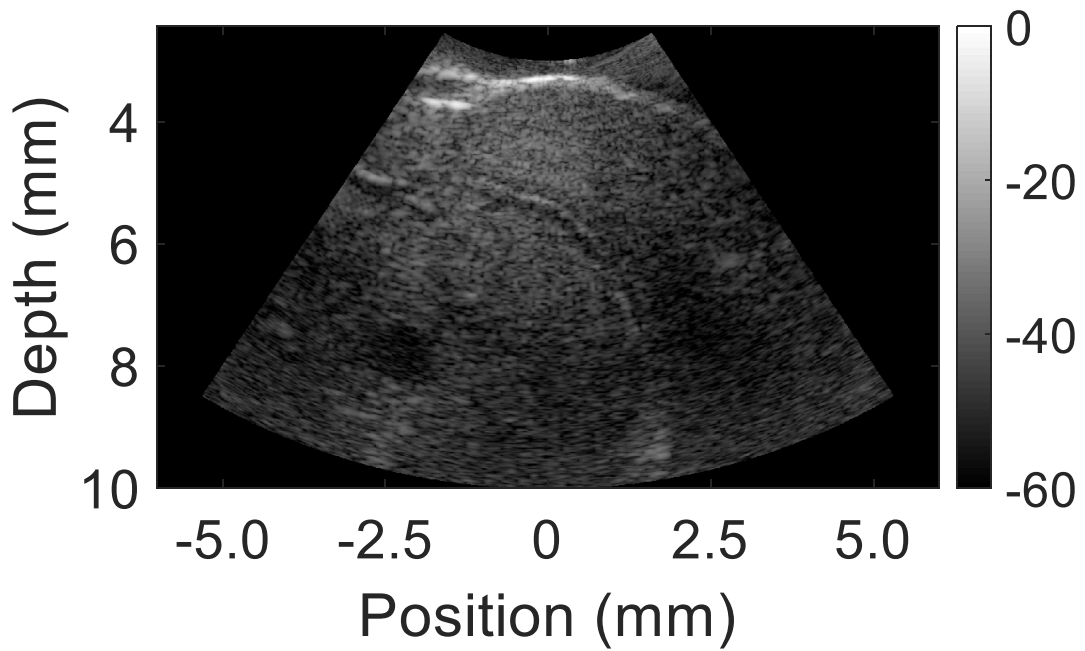
Fig 4.15 An in-vivo rat brain image captured using SODWI.

4.8 Conclusion

It has been shown that for a 64-element high-frequency phased array, SODWI beamforming produces improved contrast when compared to DWI imaging when 32 or 64 insonifications are used. SODWI also produces better SNR than DWI (I) for 32 and 64 insonifications but DWI (II) 32 yields better SNR than SODWI 32. When the number of insonifications is reduced, the encoding and decoding process is not as effective at increasing SNR and yields comparable SNR and contrast to conventional DWI imaging. Otherwise, SODWI yields better resolution than the DWI techniques and is much more suitable for phased array imaging that HMSTA and STEDI-HMSTA. When SODWI was implemented on a high-frequency system with a 40 kHz PRF, the 32 and 64 insonification schemes produce frame rates of 0.625 and 1.25 kHz respectively, which could be suitable for elastographic or functional imaging applications. The image quality achieved with this technique is very good, yielding high contrast and high SNR, superior to focused imaging with 512 insonifications. While SODWI works best for high-frequency imaging, it has the potential to replace focused B-mode imaging at both high and low operating frequencies while providing better image quality and significantly higher frame rates in phased-array imaging applications.

5 MINIMALLY INVASIVE IN-VIVO FUNCTIONAL ULTRASOUND IMAGING USING A 40 MHZ PHASED-ARRAY ENDOSCOPE: MAPPING THE AUDITORY RESPONSE IN RATS

5.1 Preamble

The following chapter presents preliminary experiments that exploit the beamforming platform and ultrafast imaging techniques implemented in Chapters 3 and 4 for functional ultrasound imaging of the rodent brain. Having established a strong beamforming platform with capabilities for ultrafast imaging, and having a research focus on neurosurgical applications, functional ultrasound imaging is an application with a high likelihood of having an immediate clinical impact. This work is an extension of the conference proceeding published for the 2019 IEEE International Ultrasonics Symposium in Glasgow, Scotland. The work titled "Minimally Invasive In Vivo Functional Ultrasound Imaging Using a 40 MHz Phased Array Endoscope: Mapping the Auditory Response in Rats", © 2019 IEEE. Reprinted, with permission, from [37], many additions were made that were not possible in the short conference proceedings format. It was intended to expand the proceedings and gather many more functional datasets for a full journal publication,

however, due to the Covid-19 pandemic, ability to access the lab or perform any additional small animal experiments was prohibited.

5.2 Introduction

The emergence of ultrafast beamforming strategies based on coherent compounding has dramatically improved Doppler capabilities for ultrasound imaging [109]. Exploiting the high temporal resolution of ultrafast ultrasound techniques such as plane-wave imaging and diverging-wave imaging has improved the signal-to-noise ratio and sensitivity of Doppler measurements, and has led to the development of functional ultrasound imaging [67]–[76]. By closely monitoring the power Doppler signal, changes in cerebral blood volume can be used as a surrogate for neural activity [67]–[70], [72]–[76]. The combination of high spatiotemporal resolution of ultrasound imaging, as well as the low cost and portability of ultrasound imaging systems, relative to more commonly used functional imaging modalities such as functional magnetic resonance imaging (fMRI), and positron emission tomography (PET), position functional ultrasound as a potentially ground-breaking tool for both preclinical and clinical applications.

For clinical neurosurgical applications, intraoperative functional mapping of the brain is critical for preserving healthy brain tissue [160]. Electrocortical stimulation mapping (ESM) is the primary intraoperative mapping tool used by neurosurgeons. An electrode is placed onto the surface of the brain and the patient is asked to perform multiple tasks related to speech [161]–[163], somatosensory processes [162], or motor movements [161]. If the patient exhibits an inability to perform any of these tasks with the electrode applied, this area of the brain is labelled with the associated

129

functional task. This process is repeated over what can sometimes be a relatively large area of the brain before tumor resection is performed. It is also iteratively redone as tumor tissue is removed and new brain tissue becomes exposed. Clinical data suggests that this process improves successful tumor resection rates from 58.1% without ESM mapping to 74.9% of cases when ESM is issued before resection [164], [165]. Functional mapping is therefore of paramount importance in improving a neurosurgeon's confidence in segmenting healthy functional tissue from tumors. Despite being the gold standard for functional mapping, ESM presents a risk of inducing seizures [164], [166], and is limited to topical mapping. Previous work by Imbault et al. has shown that functional ultrasound is capable of functional cortical mapping, matching the results of ESM in both the motor and somatosensory cortices in humans [69]. Therefore, functional ultrasound provides surgeons with similar surface-level mapping as ESM but adds depth-resolved functional information not previously available to clinicians. The clinical potential of this technology to improve surgical outcomes is evident and warrants further study. The study undertaken by Imbault et al. was performed with a large craniotomy, allowing for the topical application of a large linear array [69]. Despite the impressive potential of this technology, many neurosurgeries are performed through small burr-holes [167], [168] which do not allow the topical application of conventional linear arrays used in previous functional ultrasound imaging studies [67]–[76]. The 64-element 40 MHz phased array [12] used throughout this dissertation provides an elegant solution to the surgical size limitation given its endoscopic form factor. Leveraging this technology dramatically reduces the minimum allowable craniotomy size so that functional ultrasound can be used as a guidance tool during small burr-hole surgeries.

This chapter presents a preliminary preclinical study where an endoscopic probe with a 2.5 × 3.1 mm area was inserted inside a 3.0 × 6.5 mm craniotomy of an anaesthetized rat, visualizing the inferior colliculus (IC) under ultrasound guidance. Functional mapping of auditory neural activation was successfully measured in the IC with the application of auditory stimuli at various tones.

5.3 Methods

5.3.1 Imaging Configuration

Imaging was performed using a 64-element 40 MHz phased array. The array is tightly packaged into a 2.5 × 3.1 mm form factor manufactured per [12] and provides roughly 40 and 136 µm of axial and lateral resolution respectively. The imaging window ranges from 3 to 10 mm depths at viewing angles ranging from ±32°. Given a 1λ element-to-element pitch, this relatively narrow field of view is used to mitigate grating lobe artifacts. Beamforming is performed on the custom 64-channel high-frequency beamforming platform described in Chapter 3. The beamforming strategy selected was diverging wave imaging where 16 waves are coherently compounded whereby 49 elements are active for each diverging wave, and the angular aperture for each diverging wave is set to 90° following the diverging wave beamforming strategy, DW (I), described in Chapter 4. Each insonification is performed with a 3-cycle pulse, and the full aperture is used to receive with no apodization. This beamforming scheme was selected because when using 16 pulses, DW (I) provides 0.7dB higher SNR and 0.4dB higher contrast than SODWI. DW (I) yields 0.9dB lower SNR than DW (II) but was ultimately selected because it produces 8.7dB

higher contrast than DW (II). STEDI-HMSTA and HMSTA were not considered because of their narrowed fields of view. 16 pulses were used to meet the Nyquist criteria for the maximum Doppler frequency for rat brain blood velocities with some margin. Work by Unekawa et al. has shown rat and mouse blood velocity in single capillaries to be as high as 8.6mm/s [113]. Using this velocity and (2.29), the maximum Doppler frequency is estimated to be 450 Hz using a 40 MHz probe, requiring a frame rate of at least 900 Hz to meet the Nyquist sampling criterion for the Doppler signal. From the previous imaging schemes presented in Chapter 4, the 32 pulse methods would meet the sampling criterion for this application (1250 Hz), however other system limitations make this selection undesirable for this study. The beamforming platform has limited memory, with only enough FPGA memory to store the receive data for 64 insonifications. This combined with the relatively slow data transfer speed of 3.2Gbps creates a data transfer bottleneck. The experimentally achievable data transfer rate is 960 insonifications per second. With so few insonifications available, 16 pulses per frame were ultimately selected instead of 32 to increase the total number of frames used for post-processing and to allow for more frames to be rapidly captured fast enough to meet the Nyquist criterion. Despite the low average capture rate, the system's PRF is 40 kHz for the 64 insonifications that are stored in the system memory; therefore 4 image frames are captured at 2.5 kHz when using 16 compounded pulses per frame. The improvement in SNR by averaging across double the frames, 3dB, is larger than the loss of SNR from using half the number of pulses for DWI (I), 0.6 dB. Reducing the number of pulses per frame below 16 was not performed to further improved the SNR gain from averaging because the focusing quality and overall contrast when using fewer pulses begin to drop off rather rapidly, ~3dB when dropping from 16 to 8 compounded waves.

132

5.3.2 Animal Preparation

The experimental procedures were approved by the Dalhousie University Committee on Laboratory Animals. The rats were anesthetized using isoflurane during the investigation. A small craniotomy, 3.5×6 mm, was drilled through each rat's skull, exposing the brain. Hollow metal ear bars were inserted into the ear canals, serving both the purpose of positioning the rat into a stereotactic positioning stage and to provide a controlled pathway for closed auditory stimulation. An auditory brainstem response (ABR) test was then performed, ensuring that each rat's hearing was normal and auditory stimuli were being effectively delivered before conducting a functional ultrasound investigation. Fig 5.1 a) shows the surgical preparation, and Fig 5.1 b) highlights the particularly small size of the craniotomy by placing a 2 x 5 mm reference grid in the field of view.
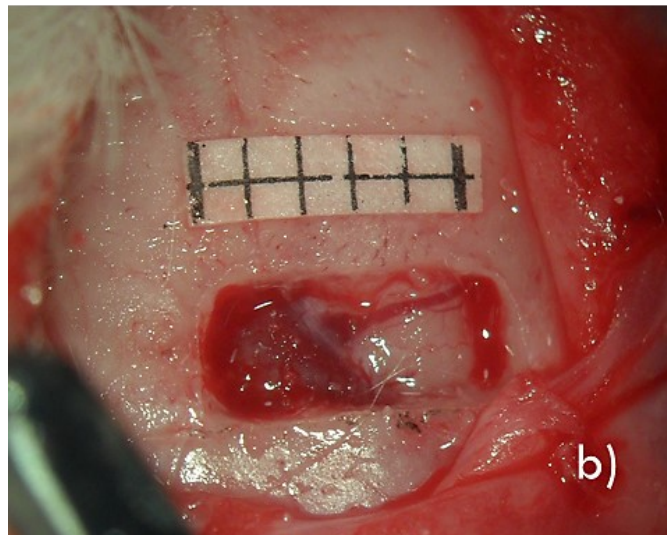
Fig 5.1 (a) Surgical craniotomy with an endoscopic probe inserted. The rat's head is securely positioned using metal ear bars and a vaporizer that delivers isoflurane. Electrodes are inserted into the skin for ABR measurements. (b) A close-up view of the craniotomy with a 2 x 5 mm grid reference.

5.3.3 Experimental Setup

With the animal situated under anesthesia, the imaging probe was mounted using a stereotactic 3-axis mechanical translation stage. A tweeter speaker (Tymphany XT25TG30-04, San Rafael, California) was connected to the left metal

134

ear bar using rubber tubing. The sound intensity is held constant across the frequencies and is delivered to the ear canal via the ear bars (4, 8, and 15 kHz). These tones were selected as they fall in the audible range for rats, which is typically between 250 Hz to 70 kHz [169]. The speaker was driven using a function generator with continuous-wave tones (Tektronics AFG3101C, Beaverton, Oregon) at intensities calibrated to give 97 dB SPL at each tone frequency. The sound level was calibrated using a microphone inserted into the ear bars. The function generator was turned on and off by a custom Python 2.7 software interface that synchronized auditory stimulus with an ultrafast imaging sequence. Imaging was also gated by the rat's breathing cycle which was monitored using a piezoelectric bimorph placed under its chest. Under flection, the bimorph outputs an analog signal which was used to trigger an oscilloscope (Keysight MSO-X 2024A, Santa Rosa, California), which provided an external trigger to a second function generator (Tektronics AFG3101C, Beaverton, Oregon), which provided a level-shifted acquisition gating signal to the beamforming system. This reduced motion artifacts that would otherwise be introduced by pulmonary inhalation and exhalation. A block diagram of the experimental setup is provided in Fig 5.2.
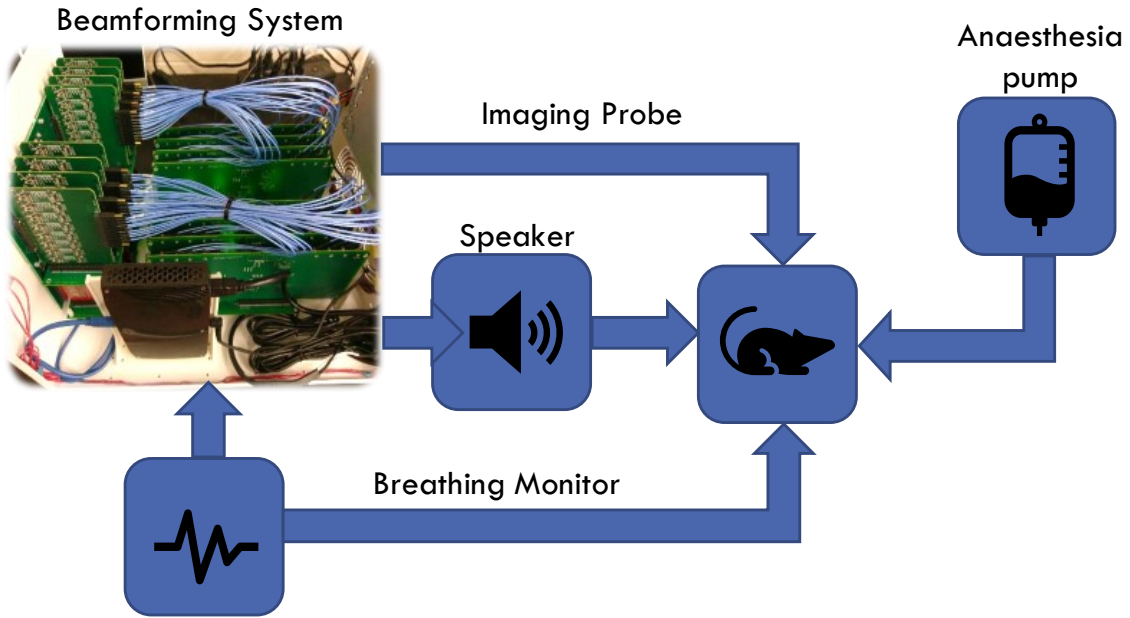
Fig 5.2 Experimental setup for mapping auditory responses to stimuli using functional ultrasound.

5.3.4 Functional Ultrasound Imaging

Baseline measurements were acquired for 2 s followed by 2 s of acquisitions with auditory stimulus applied. These measurements were repeated across 10 iterations for each tone. Fig 5.3 shows the sequence of events where 120 B-mode images are captured in succession for each 2 s window. An ensemble of 60 B-mode images was used for each power Doppler frame. The peak imaging rate was 2.5 kHz for 16 diverging waves. Channel data for 60 frames were transferred to the PC every second. All beamforming and signal processing was performed in MATLAB (Mathworks, Natick, Massachusetts). A singular value decomposition filter was applied to the B-mode frames to separate the blood signal from the brain parenchyma [112]. The Doppler ensemble was spatially separated into two equal sectors, one at the top of the image and the second at the bottom of the image. Each sector was converted

into a Casorati matrix for singular value decomposition. Note that the filtering was performed on each segment individually due to RAM limitations on the CPU. The first 35 singular values were filtered out. This threshold was determined experimentally and was found to provide excellent clutter rejection for these datasets.
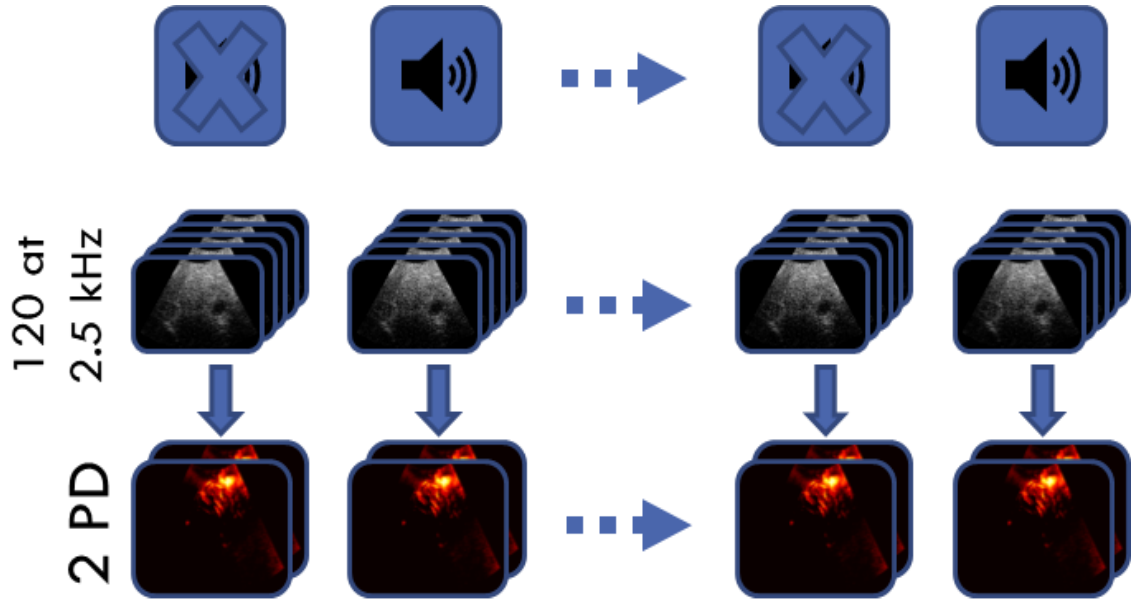
Fig 5.3 Functional ultrasound imaging sequencing. Baseline and stimulus power Doppler images are acquired alternatively. Each acquisition yields 2 power Doppler images derived from 120 B-mode images captured at 2.5 kHz.

5.4 Experimental Results and Discussion

Functional activation was successfully recorded in the IC using a minimally invasive craniotomy. Fig 5.4 a) shows the Pearson correlation coefficient mapping of the IC using a threshold at r = 0.26 (p-value = 0.05). The functional activation was anatomically confined to the IC, with no neighboring tissue showing signs of

functional activation. In Fig 5.4 b) the changes in cerebral blood volume in response to a 4 kHz tone are shown. Changes in blood volume greater than 20% are shown. The variance of the baseline measurements was determined to be at 20% therefore measurements below this value were deemed to be unreliable and were a threshold was used to filter out data below this range. The peak changes detected in this study were 85% before spatial filtering was applied and plotted as is shown in Fig 5.4 b).
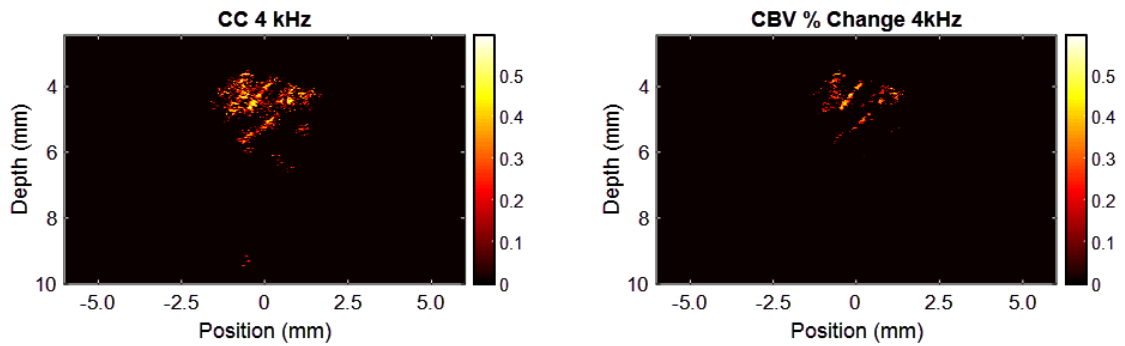
Fig 5.4 Functional activation in response to a 97 dB 4 kHz tone. (a) shows the Pearson correlation coefficient mapping with a threshold of r = 0.26 (p-value = 0.05). (b) % change in CBV processed with a simple spatial filter.

Fig 5.5 (a)-(c) overlays the functional activation in response to 4, 8, and 15 kHz tones on top of high-quality B-mode images. The spatial resolution of the functional mapping is remarkable, with roughly 40 and 136 µm of axial and lateral resolution respectively. Fig 5.5 shows correlations greater than **r = 0.26** (overlaid onto B-Mode images where 4, 8, and 15 kHz tone functional maps are shown respectively). The position of functional activation is in excellent agreement with the anatomical position of the IC which falls between 3 to 6 mm from the surface of the rat brain. The strongest activation was recorded at 4 kHz, with reduced activation intensity at 8 and 15 kHz.
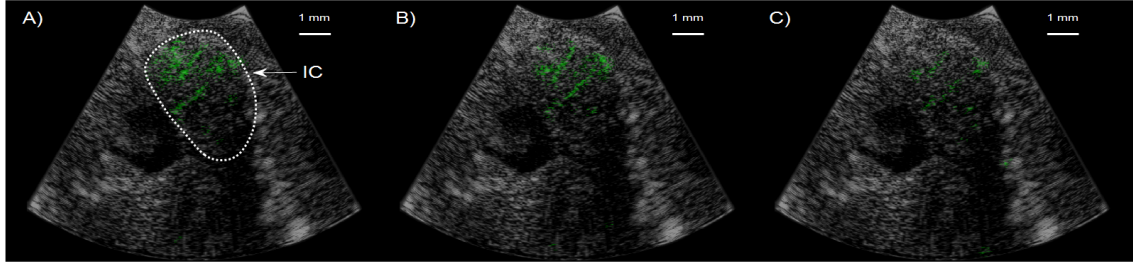
Fig 5.5 Functional activation in response to auditory stimuli is overlaid onto B-mode images. Activation is localized in the IC with parts (a)-(c) showing the change in activation in response to 4, 8, and 15 kHz tones, respectively.

The data collection for this study was done at much slower rates than conventional methods that capture hundreds of frames per second [67]–[74], [170] due to the bottleneck of transferring data from the beamforming platform to the PC. This created a significant gap between groups of B-mode images used to process the power Doppler frames. Since the system can acquire and store 64 insonifications worth of channel data, 4 frames can be generated from 16 diverging waves at an effective frame rate of 2.5 kHz. However, data transfer to the PC limits the acquisition rate of successive groups of 4 frames since all data needs to be transferred to the PC before collecting 64 subsequent insonification, or 4 new B-mode frames compounded from 16 diverging waves. This limited the acquisition to 60 B-mode frames per second, but amazingly, functional data was still extractable, mostly due to the powerful suppression of the parenchyma from the SVD filter. Another favorable condition is that the power Doppler signal is used instead of blood velocity. Power Doppler is less susceptible to aliasing since the measured change in signal will be mirrored into the Doppler spectrogram and its energy will still contribute to the power Doppler signal. This aliasing would be problematic when analyzing the blood

velocity since the perceived signal frequency may not be representative of the true Doppler shift from the actual blood velocity.

5.5 Conclusion and Future Work

This study shows that functional mapping through small burr hole surgeries is possible, vastly increasing the number of potential use-cases for functional ultrasound imaging. Functional mapping of the auditory response in the inferior colliculus was successfully performed using 4, 8, and 15 kHz tones. This technology has the potential for reducing post-operative neurological deficits by providing functional mapping that would otherwise not be possible in burr hole surgeries using state-of-the-art ESM mapping, especially in cases where ESM mapping within the sulci is not possible.

In future work, the system limitations must be addressed. Hardware-based beamforming implemented on this system by Campbell et al. have produced frames rates of 500 Hz from the system described throughout this document [45]. With a few firmware improvements, this approach can reach the Nyquist rate for rat and mouse velocities (~900 Hz). Otherwise, hardware improvements will yield massive improvements to the system's capabilities. Increasing the bandwidth between the FPGAs on the system, replacing the USB interface with a PCIe express bus, and adding on-board memory, can eliminate the limitations endured with this study. Both approaches, individually or combined, will dramatically improve system SNR and sensitivity to small changes in cerebral blood volume.

Despite the data transfer limitations, this pilot study shows the potential for functional mapping through minimally invasive craniotomies. Functional activation was detected at depth and the endoscopic nature of this imaging probe would allow neurosurgeons to push the endoscope down brain sulci for improved image guidance and functional mapping. As further experiments are conducted, the confidence interval that can be used for thresholding is also expected to improve, reflecting the natural increases in SNR and sensitivity expected with improved beamforming hardware.

6 DISCUSSION AND CONCLUSION

6.1 Preamble

This chapter provides a general discussion on the limitations of the described studies and suggested future work for each topic area. This chapter ends with a general summary of the work completed throughout this dissertation and closing remarks are provided.

6.2 Limitations and Future Work

Limitations will be discussed first. The primary limitation of this work was that early on, it was primarily focused on reducing the amount of data collected to reduce cost and complexity, which is described extensively in Chapter 3. This approach ultimately led to the design of a system that was not optimally designed for the subsequent studies on ultrafast imaging and its applications. These were the central concepts for Chapters 4 and 5, where the need to capture vast amounts of data is critical, particularly in Chapter 5. A course of action to rectify this problem is detailed in Chapter 6.2.1 by redesigning the system hardware. Advancing the system will enable more comprehensive imaging studies with less effort.

The development of the SODWI approach and the STEDI technique for phased array applications has the potential to be useful for 3D imaging. Additionally, STEDI may prove to be more powerful for linear array imaging where the directivity

drawbacks that arise when larger effective apertures are used is much less of a concern. Discussions around these topics are described in Chapter 6.2.2.

Next, improvements for the functional ultrasound experiments are outlined. These improvements are dependent on eliminating the current system data transfer bottlenecks. Once those limitations are addressed, the main objectives would be to verify the functional ultrasound processes in 2D using an updated system, extend the functionality to 3D imaging, and move from preclinical to clinical applications. Chapter 6.2.3 provides a discussion regarding these topics.

6.2.1 System Improvements

The receive data pipeline for the current system uses 9 FPGAs (XC7K160TFBG484-2, Xilinx, San Jose, CA) where 8 FPGAs are located on daughterboards which manage data before transferring data to the receive motherboard FPGA, which ultimately manages data transfer to a PC. This configuration is illustrated in Fig 6.1 (a). There are 4 data buses between the receive daughterboard FPGAs and the receive motherboard FPGA which are shared between adjacent daughterboards. Each bus has a maximum data transfer rate of 2.4 Gbps, producing a total transfer rate of 9.6 Gbps between the daughterboard FPGAs and the receive motherboard. Transferring data from the receive motherboard to the PC is done through a USB 3.0 interface at 3.2 Gbps. These rates are far below the data acquisition rate of the system which uses 12-bit ADCs with a maximum sampling rate of 150 MHz, producing a maximum data acquisition rate of

115.2 Gbps. The system is not capable of transferring data to a PC at this rate, but with a few modifications, these limitations can be resolved.
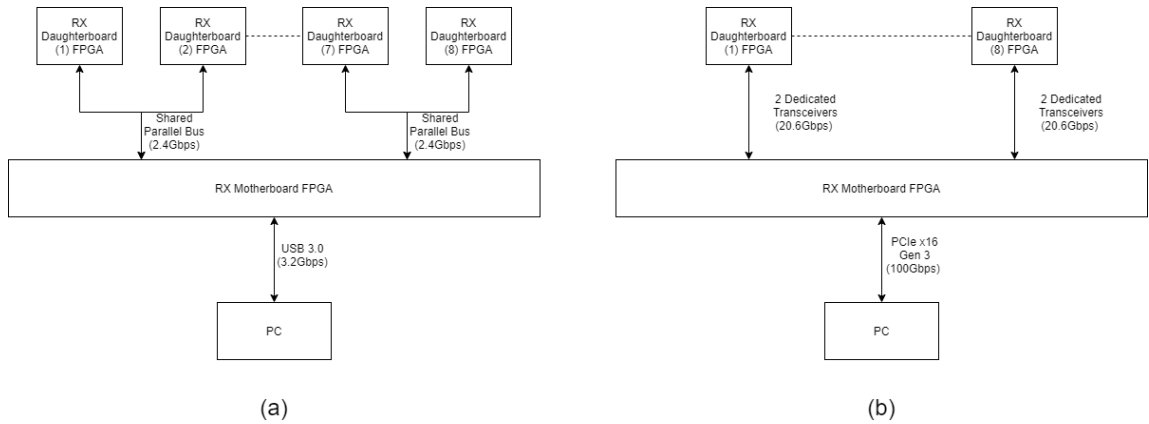
Fig 6.1 System-level data transfer pipeline for the current system configuration (a), and a proposed update with improved bandwidth (b).

The data transfer rates between the daughterboard FPGAs and the motherboard FPGA as well as the data transfer between the motherboard FPGA and PC can be dramatically improved using Xilinx transceiver technology. The receive daughterboard FPGAs have eight 10.3 Gbps transceivers that are currently unused. By simply routing 2 of these to the PCIe connector between the daughterboard FPGAs to the motherboard FPGA the 9.6Gbps data bus between the system FPGAs can be increased to 164.8Gbps as shown in Fig 6.1 (b) where each daughterboard FPGA has a dedicated 20.6Gbps transceiver link to the motherboard FPGA. This exceeds the maximum data acquisition rate of the system. The hardware changes to use the transceivers are minimal. The transceiver banks require dedicated power supplies and careful routing is needed for the differential transceiver signals.

Changes to the motherboard FPGA are more involved since the number of transceivers needed to support the proposed change in topology exceeds what is

144

available on the current FPGA (8). This FPGA would need to be replaced with a larger FPGA with more transceivers. Upgrading to an FPGA family such as the Xilinx KU060 provides 32 transceivers, which would support the 16 transceivers needed for communication between the daughterboard FPGAs and the receive motherboard FPGA, and the remaining 16 can be used for PCIe 3.0 x16. It should be noted that PCIe 4 is not supported directly by Xilinx. Third-party vendors provide purchasable intellectual property (IP) cores capable of PCIe 4. It is for this reason that this suggested topology would use generation 3 PCIe technology. With this approach, a data link of approximately 100 Gbps can be achieved between the receive motherboard FPGA and a PC. This is slightly below the system's acquisition rate of 115.2 Gbps, however, the ultrasound system will not be capturing continuously since there is time during an imaging sequence where the system waits for ultrasound energy to dissipate between transmissions. For instance, the current configuration captures data for approximately 10.24 μs but its pulse repetition interval is 25 μs. Provided there is enough memory for buffering the data captured for each transmission, the data transfer rate to the PC only needs to be 48 Gbps. This is feasible since the system currently captures 96 kBits per channel for every pulse and the FPGAs memory capacity is in the 10s of Mbits without using off-board memory.

This new topology would therefore easily exceed the data transfer requirements with plenty of overhead. This overheard could then be used in the future to support additional channels on the receive daughterboards, without needing to change the receive motherboard. More importantly, this type of topology allows for the rapid development of beamforming algorithms by making the raw channel data easily accessible in software. Software development has a much faster development cycle

than FPGA firmware, increasing the research output from this system, and it would eliminate trade-offs between data storage and frame rates that have been made previously.

6.2.2 STEDI Applications

A natural first step forward for STEDI is to apply this concept to linear array imaging. From the experimental contrast plots from Fig 4.12, the advantage of using STEDI-HMSTA over HMSTA is obvious. There are SNR, contrast, and lateral resolution advantages to using this approach when the field of view is limited to in front of the array, and directivity is not concerning. A similar imaging study to that conducted in Chapter 4 would compare STEDI-HMSTA, HMSTA, STEDI-MSTA, MSTA, plane-wave imaging, SA, and focused imaging.

Another application meriting investigation is the use of STEDI directly on DWI and plane-wave imaging. Previous work investigating axial lobes in coherent plane-wave compounding has suggested that the axial lobe artifact is attributed to the contribution of the transmitted wave from certain elements reaching a point in space before the contribution of other elements [157]. This clutter manifests into an axial lobe and it is found in both plane-wave imaging [80], [157], and DWI [81], [83]. This artifact is found throughout the literature but not very well understood or investigated. The work by Rodriguez-Morales et al. [157] is focused on using apodization to suppress this axial lobe artifact, whereas the application of the STEDI technique to these imaging techniques will exploit the undesirable characteristic leading to lobe artifacts to improve SNR. The spirit of the idea is to apply

146

beamforming delays according to the times at which contributions from different elements of each transmitted wave be applied individually, instead of applying a single transmit delay for the entire wavefront at every point in space.

In the interest of supporting this notion, a small simulation study was performed where STEDI was applied to a 40 MHz 64-element linear array with a 1 λ element pitch. The simulation was performed using Field II [46]. The simulations that were performed used the following beamforming techniques: plane-wave imaging (PWI), PWI-STEDI, MSTA, and MSTA-STEDI. These techniques were evaluated on their SNR performance using the same approach described in Chapter 4.4.2. The plane wave tilt angles spanned between $\pm 10°$. MSTA was implemented without overlapping sub-apertures. The simulated data shown in Fig 6.2 highlights the SNR advantage that can be had by implementing a STEDI beamforming strategy on these techniques. A 2-3 dB SNR improvement is achieved over PW imaging and a 2.0-8.6 dB improvement for MSTA when the number of emissions is between 4 and 32. When 64 emissions are used the beamforming strategies for MSTA and MSTA-STEDI are identical, so no advantage exists. This data is not intended to be an exhaustive analysis of STEDI for linear array applications, but rather, this preliminary data is included to show that further investigation into this technique is warranted and that it can be applied outside of the scope described in Chapter 4. Future simulations would include contrast and resolution data so that a more complete understanding of the trade-offs can be reported.
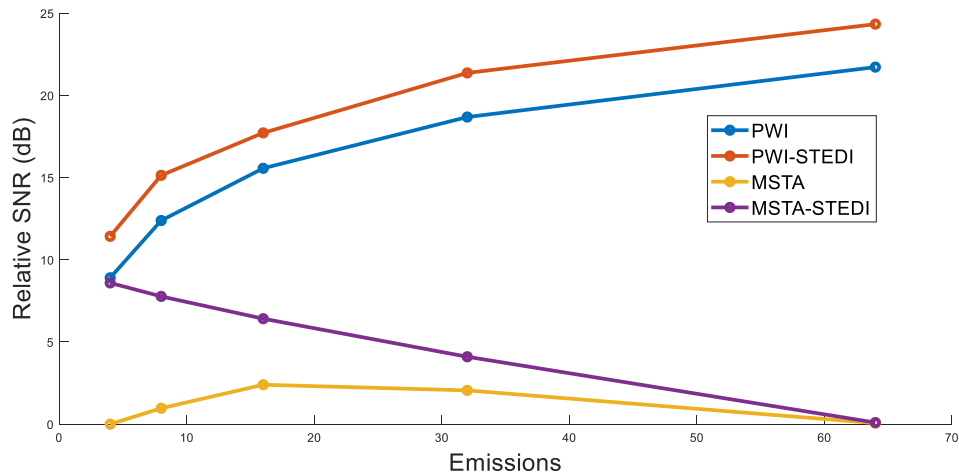
Fig 6.2 A relative SNR comparison of PWI, PWI-STEDI, MSTA, and MSTA-STEDI across a various number of compounded emissions.

Another obvious new application of STEDI and SODWI would be their application to 3D imaging. First STEDI can be used to increase the active transmit aperture in 3D imaging dramatically while preserving resolution for SA based beamforming strategies. SA for 3D imaging with sparse transmit apertures have been used extensively [171]–[173] and could significantly benefit from SNR improvements. It is common for trade-offs to be made between frame rates and active apertures and using a STEDI approach would reduce the extent of that trade-off. Applications for both 2D matrix arrays and crossed-electrode arrays are possible. For 2D matrix arrays, the increase in transmit aperture would be equal to the square of the number of adjacent elements used since the expansion of the transmit aperture occurs in two dimensions. For electrostrictive crossed-electrode arrays similar to that presented in [40]–[43], [105], [174], the elements become piezoelectric when a biasing voltage is applied to the transducer elements. For these arrays, many studies have used SA based beamforming strategies for building a synthetic focus for 3D imaging [40], [41],

[105], [174]. For these systems, group delays can only be applied to the azimuthal plane, since the elevation aperture is generally only provided a bias and no RF data is collected from these elements. As such, SODWI can be applied to the azimuthal plane since it is possible to apply transmit delays to these electrodes. STEDI can otherwise be applied to both planes, but since group delays cannot be applied to the elevation electrodes, reducing the number of transmit pulses in elevation below the total number of elevation elements will theoretically lead to a deterioration of directivity in this dimension. As such there will be limitations for 3D phased-array applications with crossed electrodes using this technique. Alternatively, for conventional 2D linear arrays, this penalty will not exist.

6.2.3 Functional Ultrasound

The functional ultrasound experiments in this work are preliminary and warrant future work to rectify their shortcomings. By leveraging hardware changes such as those described in Chapter 6.2.1 or by improving on the frame rates of the hardware-based beamformer configuration presented in [45], the experimental trade-offs made in Chapter 5 can be eliminated. It is best to meet the Doppler Nyquist criterion and to have the ensemble of B-mode frames used for Doppler processing captured at a constant rate, instead of fluctuating to accommodate data transfer to the PC as described in Chapter 5.3.1. This should bring immediate improvements to the blood flow characterization by meeting both the Nyquist criterion for the Doppler measurements and by providing additional frames to average the power Doppler signal.

149

Once the hardware problems are solved, the functional auditory experiments in rats should be repeated so that new experimental results can be compared to that presented in Chapter 5. Additionally, lowering the center frequency of the imaging array would be immediately beneficial. This would improve SNR at depth and increase the imaging field of view. For rat brain imaging, the maximum vertical depth of the deepest neurological structures is approximately 11 mm [175]. This is just beyond the limits of the 40 MHz probe used in Chapter 5. This increased depth is not critical, but an enlarged image window would be much more useful for clinical applications where the scale of neurological structures is much larger than that of a rat. The size difference is considerable. A rat brain weighs roughly 2g [176] whereas a human brain weighs roughly 1350g [177]. Dropping the center frequency of the endoscope to 20 MHz from 40 MHz while preserving the element spacing would yield a $\lambda/2$ element pitch, pushing the grating lobes to much wider angles which would allow for the field of view to be widened from $\pm32°$ to a more conventional $\pm45°$. The lower frequency also provides better SNR at depth and would more than double the useable imaging depth compared to a 40 MHz counterpart. This would come at the cost of resolution, but previous clinical functional ultrasound experiments have been conducted using probes with a center frequency of 6 MHz [69], [75], [76], it is therefore unlikely that the resolution trade-off would be detrimental, whereas the enlarged field of view would be highly desirable.

Keeping the long-term goal of translating this technology to clinical applications in mind, extending these capabilities to 3D would significantly improve the utility of this tool in the context of burr-hole surgeries. These procedures typically use openings of approximately 14-16 mm in diameter [178], [179], which limits the extent to which a surgeon would be able to manipulate and manoeuvre the imaging probe.

150

Having the ability to extract volumetric functional information could potentially improve procedure speeds by removing the need to translate or rotate the imaging array inside the burr hole while simultaneously repeating a functional imaging sequence for each position. Endoscopic 3D probes such as that presented by Latham et al [39] show that 3D volumetric imaging from tightly packaged arrays is possible. As this technology matures and ultrafast frame rates are exploited using this type of probe, it will be possible to extract 3D functional brain measurements through a small burr hole without the need to collect each slice individually.

6.3 Final Conclusions

The studies conducted in this thesis were designed to help support a minimally invasive high-frequency endoscopic array by developing a custom beamforming platform and developing new state-of-the-art beamforming techniques so that the array's capabilities can be leverage for specialized applications such as functional ultrasound imaging.

The first study presented in Chapter 3 produced a custom 64-channel high-frequency beamforming platform capable of real-time imaging. This work resulted in the implementation of a novel variable sampling beamforming scheme which reduced the sampling rate to be ¾ λ of the central frequency. ¾ λ demodulation had to the best of my knowledge, not previously been presented in the ultrasound research community, marking the first time that this demodulation scheme had been presented as an alternative to the conventional ¼ λ demodulation. The data acquisition for this approach is also minimal. For each pixel in the image only one

sample is acquired per element, which relaxed the system's data throughput considerably. By leveraging this approach and the hardware that was developed to implement this approach, it marked the first time that a dedicated high-frequency ultrasound system was capable of real-time imaging on a high-frequency phased array. Previous works and systems had supported linear array imaging strategies but were incapable of supporting phased array imaging due to the added complexity of steering the ultrasound beam across a sector of angles. This work yielded excellent results, producing high-quality images in real-time.

In the second study detailed in Chapter 4, a new ultrafast beamforming scheme, SODWI, was modeled and compared to various other ultrafast beamforming techniques. These approaches were implemented and experimentally evaluated using the beamforming platform. SODWI was shown to be suitable for phased array applications and generated images of higher quality than focused imaging. It provided improved resolution over DWI techniques and under the correct configuration, when 16 or more pulses were possible, produced higher SNR and contrast. This study also shows that the use of STEDI can provide SNR, grating lobe, and resolution improvements over conventional delay insertion techniques with minimal complexity.

In the third study described in Chapter 5, the system configuration and ultrafast capabilities developed in Chapter 4 were leveraged for functional ultrasound imaging of rat brains. This study showed that it was possible to exploit the minimally invasive form factor of the 2.5 x 3.0 mm endoscopic probe for procedures requiring only a small craniotomy (3.5×6.0 mm). To the best of my knowledge, this is the smallest opening that functional ultrasound experiments have been performed through.

Further improvements and studies building on this work will allow for research not possible with pre-existing technology.

The sum of this work has provided a research platform highly suited for high-frequency phased array beamforming. In developing this beamforming platform, innovations were created to reduce the necessary sampling rates, and a new ultrafast beamforming technique has been developed. The tools and methods developed throughout this work have been applied to functional ultrasound imaging. This work provides some first steps in broadening the scope of applications for high-frequency phased array endoscopes.

BIBLIOGRAPHY

[1] C. J. Pavlin, M. D. Sherar, and F. S. Foster, "Subsurface ultrasound microscopic imaging of the intact eye," *Ophthalmology*, vol. 97, no. 2, pp. 244–250, 1990.

[2] R. H. Silverman, "High-resolution ultrasound imaging of the eye-a review," *Clinical \& experimental ophthalmology*, vol. 37, no. 1, pp. 54–67, 2009.

[3] C. J. Pavlin, K. Harasiewicz, and F. S. Foster, "Ultrasound biomicroscopy of anterior segment structures in normal and glaucomatous eyes," *American journal of ophthalmology*, vol. 113, no. 4, pp. 381–389, 1992.

[4] D. H. Turnbull, B. G. Starkoski, K. A. Harasiewicz, J. L. Semple, L. From, A. K. Gupta, D. N. Sauder, and F. S. Foster, "A 40-100 MHz B-scan ultrasound backscatter microscope for skin imaging," *Ultrasound in medicine \& biology*, vol. 21, no. 1, pp. 79–88, 1995.

[5] M. Vogt and H. Ermert, "In vivo ultrasound biomicroscopy of skin: Spectral system characteristics and inverse filtering optimization," *IEEE transactions on ultrasonics, ferroelectrics, and frequency control*, vol. 54, no. 8, pp. 1551–1559, 2007.

[6] L. Machet, V. Belot, M. Naouri, M. Boka, Y. Mourtada, B. Giraudeau, B. Laure, A. Perrinaud, M.-C. Machet, and L. Vaillant, "Preoperative measurement of thickness of cutaneous melanoma using high-resolution 20 MHz ultrasound imaging: A monocenter prospective study and systematic review of the literature," *Ultrasound in medicine \& biology*, vol. 35, no. 9, pp. 1411–1420, 2009.

[7] D. E. Dausch, K. H. Gilchrist, J. B. Carlson, S. D. Hall, J. B. Castellucci, and O. T. von Ramm, "In vivo real-time 3-D intracardiac echo using PMUT arrays," *IEEE Transactions on Ultrasonics, Ferroelectrics, and Frequency Control*, vol. 61, no. 10, pp. 1754–1764, 2014.

[8] E. J. Gussenhoven, C. E. Essed, C. T. Lancée, F. Mastik, P. Frietman, F. C. van Egmond, J. Reiber, H. Bosch, H. van Urk, J. Roelandt, and others, "Arterial wall characteristics determined by intravascular ultrasound imaging: an in vitro study," *Journal of the American College of Cardiology*, vol. 14, no. 4, pp. 947–952, 1989.

[9] G. Lockwood, L. Ryan, and F. Foster, "A 45 to 55 MHz needle-based ultrasound system for invasive imaging," *Ultrasonic imaging*, vol. 15, no. 1, pp. 1–13, 1993.

[10] A. Bezanson, P. Garland, R. Adamson, and J. Brown, "Fabrication of a miniaturized 64-element high-frequency phased array," in *Ultrasonics Symposium*

(IUS), 2012 IEEE International, 2012, pp. 2114–2117.

[11]   J. M. Cannata and K. K. Shung, "Development of a high frequency (35-MHz) linear ultrasonic array," in *Medical Imaging 2004: Ultrasonic Imaging and Signal Processing*, 2004, vol. 5373, pp. 18–23.

[12]   A. Bezanson, R. Adamson, and J. Brown, "Fabrication and performance of a miniaturized 64-element high-frequency endoscopic phased array.," *IEEE Trans Ultrason Ferroelectr Freq Control*, vol. 61, no. 1, pp. 33–43, 2014.

[13]   C. Hu, L. Zhang, J. M. Cannata, and K. K. Shung, "Development of a digital high frequency ultrasound array imaging system," in *Ultrasonics Symposium (IUS), 2010 IEEE*, 2010, pp. 1972–1975.

[14]   J. M. Cannata, J. A. Williams, L. Zhang, C.-H. Hu, and K. K. Shung, "A high-frequency linear ultrasonic array utilizing an interdigitally bonded 2-2 piezo-composite," *IEEE transactions on ultrasonics, ferroelectrics, and frequency control*, vol. 58, no. 10, pp. 2202–2212, 2011.

[15]   C. Morton and G. Lockwood, "Design of a 40 MHz annular array," in *2001 IEEE Ultrasonics Symposium. Proceedings. An International Symposium (Cat. No. 01CH37263)*, 2001, vol. 2, pp. 1135–1138.

[16]   C. Morton and G. Lockwood, "Evaluation of kerfless linear arrays," in *Ultrasonics Symposium, 2002. Proceedings. 2002 IEEE*, 2002, vol. 2, pp. 1257–1260.

[17]   J. A. Brown, C. E. M. Démoré, and G. R. Lockwood, "Design and fabrication of annular arrays for high-frequency ultrasound.," *IEEE Trans Ultrason Ferroelectr Freq Control*, vol. 51, no. 8, pp. 1010–7, 2004.

[18]   J. Brown, F. Foster, and G. Lockwood, "A 40 MHz linear array based on a 1-3 composite with geometric elevation focusing," in *IEEE Ultrason Symp Proc*, 2006, pp. 256–259.

[19]   M. Lukacs, J. Yin, G. Pang, R. C. Garcia, E. Cherin, R. Williams, J. Mehi, and F. S. Foster, "Performance and characterization of new micromachined high-frequency linear arrays," *IEEE transactions on ultrasonics, ferroelectrics, and frequency control*, vol. 53, no. 10, pp. 1719–1729, 2006.

[20]   T. A. Ritter, T. R. Shrout, R. Tutwiler, and K. K. Shung, "A 30-MHz piezo-composite ultrasound array for medical imaging applications," *IEEE transactions on ultrasonics, ferroelectrics, and frequency control*, vol. 49, no. 2, pp. 217–230, 2002.

[21]   J. A. Ketterling, O. Aristizabal, D. H. Turnbull, and F. L. Lizzi, "Design and fabrication of a 40-MHz annular array transducer," *IEEE transactions on*

ultrasonics, ferroelectrics, and frequency control, vol. 52, no. 4, pp. 672–681, 2005.

[22] H. Himal, "Minimally invasive (laparoscopic) surgery," *Surgical Endoscopy And Other Interventional Techniques*, vol. 16, no. 12, pp. 1647–1652, 2002.

[23] M. Jacobs, J. Verdeja, and H. Goldstein, "Minimally invasive colon resection (laparoscopic colectomy)," 1991.

[24] S. Mahboob, R. McPhillips, Z. Qiu, Y. Jiang, C. Meggs, G. Schiavone, T. Button, M. Desmulliez, C. Demore, S. Cochran, and others, "Intraoperative ultrasound-guided resection of gliomas: a meta-analysis and review of the literature," *World neurosurgery*, vol. 92, pp. 255–263, 2016.

[25] R. Firsching, N. Klug, U. Börner, and P. Sanker, "Lesions of the sensorimotor region: somatosensory evoked potentials and ultrasound guided surgery.," *Acta Neurochir (Wien)*, vol. 118, no. 3–4, pp. 87–90, 1992.

[26] J. Regelsberger, F. Lohmann, K. Helmke, and M. Westphal, "Ultrasound-guided surgery of deep seated brain lesions," *European journal of ultrasound*, vol. 12, no. 2, pp. 115–121, 2000.

[27] L. Dell'Atti, "Efficacy of ultrasound-guided testicle-sparing surgery for small testicular masses," *Journal of ultrasound*, vol. 19, no. 1, pp. 29–33, 2016.

[28] J. H. Volders, M. H. Haloua, N. M. Krekel, S. Meijer, and P. M. van den Tol, "Current status of ultrasound-guided surgery in the treatment of breast cancer," *World journal of clinical oncology*, vol. 7, no. 1, p. 44, 2016.

[29] N. M. Krekel, B. M. Zonderhuis, H. W. Schreurs, A. M. L. Cardozo, H. Rijna, H. Van Der Veen, S. Muller, P. Poortman, L. De Widt, W. K. De Roos, and others, "Ultrasound-guided breast-sparing surgery to improve cosmetic outcomes and quality of life. A prospective multicentre randomised controlled clinical trial comparing ultrasound-guided surgery to traditional palpation-guided surgery (COBALT trial)," *BMC surgery*, vol. 11, no. 1, p. 8, 2011.

[30] T. K. Chen, P. Abolmaesumi, D. R. Pichora, and R. E. Ellis, "A system for ultrasound-guided computer-assisted orthopaedic surgery," *Computer Aided Surgery*, vol. 10, no. 5–6, pp. 281–292, 2005.

[31] L. Phee, D. Xiao, J. Yuen, C. F. Chan, H. Ho, C. H. Thng, C. Cheng, and W. S. Ng, "Ultrasound guided robotic system for transperineal biopsy of the prostate," in *Proceedings of the 2005 IEEE international conference on robotics and automation*, 2005, pp. 1315–1320.

[32] P. Bao, T. K. Sinha, C.-C. R. Chen, J. R. Warmath, R. L. Galloway, and A. J. Herline, "A prototype ultrasound-guided laparoscopic radiofrequency ablation system.," *Surg Endosc*, vol. 21, no. 1, pp. 74–9, 2007.

[33] C. A. Samson, J. Leadbetter, and J. A. Brown, "A 50 MHz phased array beamformer using a novel 'one sample per pixel'variable sampling technique," in *Ultrasonics Symposium (IUS), 2015 IEEE International*, 2015, pp. 1–4.

[34] C. A. Samson, A. Bezanson, and J. A. Brown, "A sub-nyquist, variable sampling, high-frequency phased array beamformer," *IEEE transactions on ultrasonics, ferroelectrics, and frequency control*, vol. 64, no. 3, pp. 568–576, 2016.

[35] C. Samson, E. Simpson, R. Adamson, and J. A. Brown, "Sparse Orthogonal Diverging Wave Imaging on a High-Frequency Phased Array," in *2018 IEEE International Ultrasonics Symposium (IUS)*, 2018, pp. 1–4.

[36] C. Samson, R. Adamson, and J. A. Brown, "Ultrafast Phased Array Imaging using Sparse Orthogonal Diverging Waves," *IEEE Transactions on Ultrasonics, Ferroelectrics, and Frequency Control*, 2020.

[37] C. Samson, T. Landry, and J. A. Brown, "Minimally Invasive InVivo Functional Ultrasound Imaging Using a 40 MHz Phased Array Endoscope: Mapping the Auditory Response in Rats," in *2019 IEEE International Ultrasonics Symposium (IUS)*, 2019, pp. 2141–2144.

[38] C. A. Samson, K. Latham, and J. A. Brown, *Real-time, 45 MHz, split-aperture phased array beamformer with efficient sign coherence grating lobe suppression*. 2016 IEEE International Ultrasonics Symposium (IUS), 2016.

[39] K. Latham, C. Samson, E. Simpson, R. Zemp, and J. A. Brown, "A 30 MHz, 3D Imaging, Forward Looking Miniature Endoscope Based on a 128-Element Relaxor Array," in *2018 IEEE International Ultrasonics Symposium (IUS)*, 2018, pp. 1–4.

[40] K. Latham, C. Samson, C. Ceroici, R. J. Zemp, and J. A. Brown, "Fabrication and performance of a 128-element crossed-electrode relaxor array, for a novel 3D imaging approach," in *2017 IEEE International Ultrasonics Symposium (IUS)*, 2017, pp. 1–4.

[41] K. Latham, C. Samson, J. Woodacre, E. Simpson, R. Zemp, and J. A. Brown, "A New 3D Imaging Technique Integrating Ultrafast Compounding, Hadamard Encoding, and Reconfigurable Fresnel Lensing, demonstrated on a 128-Element, Crossed Electrode Endoscope," in *2019 IEEE International Ultrasonics Symposium (IUS)*, 2019, pp. 2052–2055.

[42] K. Latham, C. A. Samson, A. Bezanson, R. Adamson, and J. A. Brown, "Design and preliminary experimental results for a high-frequency crossed electrode

phased array, based on a reconfigurable Fresnel lens," in *2016 IEEE International Ultrasonics Symposium (IUS)*, 2016, pp. 1–4.

[43] K. Latham, C. Ceroici, C. A. Samson, R. J. Zemp, and J. A. Brown, "Simultaneous azimuth and fresnel elevation compounding: A fast 3-d imaging technique for crossed-electrode arrays," *IEEE transactions on ultrasonics, ferroelectrics, and frequency control*, vol. 65, no. 9, pp. 1657–1668, 2018.

[44] E. Simpson, K. Latham, C. Samson, J. Woodacre, T. Aguinaga, and J. A. Brown, "Single-Channel Hadamard Encoded Endoscope for High-Frequency IVUS Imaging," in *2019 IEEE International Ultrasonics Symposium (IUS)*, 2019, pp. 1801–1804.

[45] N. A. Campbell, C. A. Samson, and J. A. Brown, "An Ultrafast High-Frequency Hardware Beamformer for a Phased Array Endoscope," in *2019 IEEE International Ultrasonics Symposium (IUS)*, 2019, pp. 1505–1508.

[46] J. A. Jensen, "Field: A program for simulating ultrasound systems," in *10TH NORDICBALTIC CONFERENCE ON BIOMEDICAL IMAGING, VOL. 4, SUPPLEMENT 1, PART 1: 351-353*, 1996.

[47] P. Langevin, "Oeuvres scientifiques," 1950.

[48] Lord Rayleigh, "XXXVII. On the passage of waves through apertures in Plane screens, and allied problems," *The London, Edinburgh, and Dublin Philosophical Magazine and Journal of Science*, vol. 43, no. 263, pp. 259–272, 1897.

[49] J. Lockwood and J. Willette, "High-speed method for computing the exact solution for the pressure variations in the nearfield of a baffled piston," *The Journal of the Acoustical Society of America*, vol. 53, no. 3, pp. 735–741, 1973.

[50] P. R. Stepanishen, "The time-dependent force and radiation impedance on a piston in a rigid infinite planar baffle," *The Journal of the Acoustical Society of America*, vol. 49, no. 3B, pp. 841–849, 1971.

[51] J.-F. Theumann, M. Arditi, J.-J. Meister, and E. Jaques, "Acoustic fields of concave cylindrical transducers," *The Journal of the Acoustical Society of America*, vol. 88, no. 2, pp. 1160–1169, 1990.

[52] A. Penttinen and M. Luukkala, "The impulse response and pressure nearfield of a curved ultrasonic radiator," *Journal of Physics D: Applied Physics*, vol. 9, no. 10, p. 1547, 1976.

[53] J. A. Jensen, "Ultrasound fields from triangular apertures," *The Journal of the Acoustical Society of America*, vol. 100, no. 4, pp. 2049–2056, 1996.

[54] P. R. Stepanishen, "Pulsed transmit/receive response of ultrasonic piezoelectric transducers," *The Journal of the Acoustical Society of America*, vol. 69, no. 6, pp. 1815–1827, 1981.

[55] J. A. Jensen, "A model for the propagation and scattering of ultrasound in tissue.," *J. Acoust. Soc. Am.*, vol. 89, no. 1, pp. 182–90, 1991.

[56] T. L. Szabo, *Diagnostic ultrasound imaging: inside out*. Academic Press, 2004.

[57] C. L. Dolph, "A current distribution for broadside arrays which optimizes the relationship between beam width and side-lobe level," *Proceedings of the IRE*, vol. 34, no. 6, pp. 335–348, 1946.

[58] A. Nuttall, "Some windows with very good sidelobe behavior," *IEEE Transactions on Acoustics, Speech, and Signal Processing*, vol. 29, no. 1, pp. 84–91, 1981.

[59] D. A. Guenther and W. F. Walker, "Optimal apodization design for medical ultrasound using constrained least squares part I: theory," *IEEE transactions on ultrasonics, ferroelectrics, and frequency control*, vol. 54, no. 2, pp. 332–342, 2007.

[60] J.-F. Synnevag, A. Austeng, and S. Holm, "Benefits of minimum-variance beamforming in medical ultrasound imaging," *IEEE transactions on ultrasonics, ferroelectrics, and frequency control*, vol. 56, no. 9, pp. 1868–1879, 2009.

[61] J. Camacho, M. Parrilla, and C. Fritsch, "Phase coherence imaging.," *IEEE transactions on ultrasonics, ferroelectrics, and frequency control*, vol. 56, no. 5, pp. 958–974, 2009.

[62] J. Camacho, M. Parrilla, and C. Fritsch, "Grating-lobes reduction by application of Phase Coherence Factors," in *2009 IEEE International Ultrasonics Symposium*, 2009, pp. 341–344.

[63] P.-C. Li and M.-L. Li, "Adaptive imaging using the generalized coherence factor.," *IEEE Trans Ultrason Ferroelectr Freq Control*, vol. 50, no. 2, pp. 128–41, 2003.

[64] D. Chauvet, M. Imbault, L. Capelle, C. Demene, M. Mossad, C. Karachi, A.-L. Boch, J.-L. Gennisson, and M. Tanter, "In vivo measurement of brain tumor elasticity using intraoperative shear wave elastography," *Ultraschall in der Medizin-European Journal of Ultrasound*, vol. 37, no. 06, pp. 584–590, 2016.

[65] R. G. Barr, K. Nakashima, D. Amy, D. Cosgrove, A. Farrokh, F. Schafer, J. C. Bamber, L. Castera, B. I. Choi, Y.-H. Chou, and others, "WFUMB guidelines and recommendations for clinical use of ultrasound elastography: Part 2: breast,"

Ultrasound in medicine \& biology, vol. 41, no. 5, pp. 1148–1160, 2015.

[66] P. Song, H. Zhao, M. W. Urban, A. Manduca, S. V. Pislaru, R. R. Kinnick, C. Pislaru, J. F. Greenleaf, and S. Chen, "Improved shear wave motion detection using pulse-inversion harmonic imaging with a phased array transducer," *IEEE transactions on medical imaging*, vol. 32, no. 12, pp. 2299–2310, 2013.

[67] C. Errico, B.-F. Osmanski, S. Pezet, O. Couture, Z. Lenkei, and M. Tanter, "Transcranial functional ultrasound imaging of the brain using microbubble-enhanced ultrasensitive Doppler," *NeuroImage*, vol. 124, pp. 752–761, 2016.

[68] E. Macé, G. Montaldo, I. Cohen, M. Baulac, M. Fink, and M. Tanter, "Functional ultrasound imaging of the brain," *Nature methods*, vol. 8, no. 8, p. 662, 2011.

[69] M. Imbault, D. Chauvet, J.-L. Gennisson, L. Capelle, and M. Tanter, "Intraoperative functional ultrasound imaging of human brain activity," *Scientific reports*, vol. 7, no. 1, p. 7304, 2017.

[70] É. Macé, G. Montaldo, S. Trenholm, C. Cowan, A. Brignall, A. Urban, and B. Roska, "Whole-brain functional ultrasound imaging reveals brain modules for visuomotor integration," *Neuron*, vol. 100, no. 5, pp. 1241–1251, 2018.

[71] E. Mace, G. Montaldo, B.-F. Osmanski, I. Cohen, M. Fink, and M. Tanter, "Functional ultrasound imaging of the brain: theory and basic principles," *IEEE transactions on ultrasonics, ferroelectrics, and frequency control*, vol. 60, no. 3, pp. 492–506, 2013.

[72] M. Gesnik, K. Blaize, T. Deffieux, J.-L. Gennisson, J.-A. Sahel, M. Fink, S. Picaud, and M. Tanter, "3D functional ultrasound imaging of the cerebral visual system in rodents," *NeuroImage*, vol. 149, pp. 267–274, 2017.

[73] B.-F. Osmanski, C. Martin, G. Montaldo, P. Lanièce, F. Pain, M. Tanter, and H. Gurden, "Functional ultrasound imaging reveals different odor-evoked patterns of vascular activity in the main olfactory bulb and the anterior piriform cortex," *Neuroimage*, vol. 95, pp. 176–184, 2014.

[74] C. Bimbard, C. Demene, C. Girard, S. Radtke-Schuller, S. Shamma, M. Tanter, and Y. Boubenec, "Multi-scale mapping along the auditory hierarchy using high-resolution functional UltraSound in the awake ferret," *Elife*, vol. 7, p. e35028, 2018.

[75] C. Demene, J. Baranger, M. Bernal, C. Delanoe, S. Auvin, V. Biran, M. Alison, J. Mairesse, E. Harribaud, M. Pernot, and others, "Functional ultrasound imaging of brain activity in human newborns," *Science translational medicine*, vol. 9, no. 411, p. eaah6756, 2017.

[76] C. Demené, J. Mairesse, J. Baranger, M. Tanter, and O. Baud, "Ultrafast Doppler for neonatal brain imaging," *NeuroImage*, vol. 185, pp. 851–856, 2019.

[77] K. Christensen-Jeffries, R. J. Browning, M.-X. Tang, C. Dunsby, and R. J. Eckersley, "In vivo acoustic super-resolution and super-resolved velocity mapping using microbubbles," *IEEE transactions on medical imaging*, vol. 34, no. 2, pp. 433–440, 2014.

[78] O. Couture, V. Hingot, B. Heiles, P. Muleki-Seya, and M. Tanter, "Ultrasound localization microscopy and super-resolution: A state of the art," *IEEE transactions on ultrasonics, ferroelectrics, and frequency control*, vol. 65, no. 8, pp. 1304–1320, 2018.

[79] O. Couture, B. Besson, G. Montaldo, M. Fink, and M. Tanter, "Microbubble ultrasound super-localization imaging (MUSLI)," in *2011 IEEE International Ultrasonics Symposium*, 2011, pp. 1285–1287.

[80] G. Montaldo, M. Tanter, J. Bercoff, N. Benech, and M. Fink, "Coherent plane-wave compounding for very high frame rate ultrasonography and transient elastography," *IEEE transactions on ultrasonics, ferroelectrics, and frequency control*, vol. 56, no. 3, pp. 489–506, 2009.

[81] C. Papadacci, M. Pernot, M. Couade, M. Fink, and M. Tanter, "High-contrast ultrafast imaging of the heart," *IEEE transactions on ultrasonics, ferroelectrics, and frequency control*, vol. 61, no. 2, pp. 288–301, 2014.

[82] L. Tong, H. Gao, H. F. Choi, and J. D'hooge, "Comparison of conventional parallel beamforming with plane wave and diverging wave imaging for cardiac applications: A simulation study," *IEEE transactions on ultrasonics, ferroelectrics, and frequency control*, vol. 59, no. 8, pp. 1654–1663, 2012.

[83] H. Hasegawa and H. Kanai, "High-frame-rate echocardiography using diverging transmit beams and parallel receive beamforming," *Journal of medical ultrasonics*, vol. 38, no. 3, pp. 129–140, 2011.

[84] J. Porée, D. Posada, A. Hodzic, F. Tournoux, G. Cloutier, and D. Garcia, "High-frame-rate echocardiography using coherent compounding with Doppler-based motion-compensation," *IEEE transactions on medical imaging*, vol. 35, no. 7, pp. 1647–1657, 2016.

[85] H. Hasegawa and H. Kanai, "High-frame-rate echocardiography with reduced sidelobe level," *IEEE transactions on ultrasonics, ferroelectrics, and frequency control*, vol. 59, no. 11, pp. 2569–2575, 2012.

[86] G. R. Lockwood, J. R. Talman, and S. S. Brunke, "Real-time 3-D ultrasound imaging using sparse synthetic aperture beamforming.," *IEEE Trans Ultrason*

Ferroelectr Freq Control, vol. 45, no. 4, pp. 980–8, 1998.

[87]   I. Trots, A. Nowicki, M. Lewandowski, and Y. Tasinkevych, "Multi-element synthetic transmit aperture in medical ultrasound imaging," *Archives of Acoustics*, vol. 35, no. 4, pp. 687–699, 2010.

[88]   Y. Tasinkevych, Z. Klimonda, M. Lewandowski, A. Nowicki, and P. Lewin, "Modified multi-element synthetic transmit aperture method for ultrasound imaging: A tissue phantom study," *Ultrasonics*, vol. 53, no. 2, pp. 570–579, 2013.

[89]   L. Ziomek, *Fundamentals of Acoustic Field Theory and Space-Time Signal Processing*. Taylor \& Francis, 1994.

[90]   L. R. Gavrilov, J. W. Hand, P. Abel, C. Cain, and others, "A method of reducing grating lobes associated with an ultrasound linear phased array intended for transrectal thermotherapy," *Ultrasonics, Ferroelectrics, and Frequency Control, IEEE Transactions on*, vol. 44, no. 5, pp. 1010–1017, 1997.

[91]   Z. Torbatian, R. Adamson, and J. A. Brown, "Experimental verification of pulse-probing technique for improving phase coherence grating lobe suppression," *Ultrasonics, Ferroelectrics, and Frequency Control, IEEE Transactions on*, vol. 60, no. 7, pp. 1324–1332, 2013.

[92]   Z. Torbatian, R. Adamson, M. Bance, and J. A. Brown, "A split-aperture transmit beamforming technique with phase coherence grating lobe suppression.," *IEEE Trans Ultrason Ferroelectr Freq Control*, vol. 57, no. 11, pp. 2588–95, 2010.

[93]   F. A. Duck, *Physical properties of tissues: a comprehensive reference book*. Academic press, 2013.

[94]   J. G. Abbott, "Rationale and derivation of MI and TI—a review," *Ultrasound in medicine \& biology*, vol. 25, no. 3, pp. 431–441, 1999.

[95]   "Guidelines for the Safe Use of Diagnostic Ultrasound ." [Online]. Available: https://www.canada.ca/en/health-canada/services/environmental-workplace-health/reports-publications/radiation/guidelines-safe-use-diagnostic-ultrasound.html#a23. [Accessed: 11-Apr-2020].

[96]   R. Y. Chiao and X. Hao, "Coded excitation for diagnostic ultrasound: A system developer's perspective," *IEEE transactions on ultrasonics, ferroelectrics, and frequency control*, vol. 52, no. 2, pp. 160–170, 2005.

[97]   Y. Takeuchi, "Chirped excitation for<-100 dB time sidelobe echo sounding," in *1995 IEEE Ultrasonics Symposium. Proceedings. An International Symposium*, 1995, vol. 2, pp. 1309–1314.

[98] T. X. Misaridis and J. A. Jensen, "An effective coded excitation scheme based on a predistorted FM signal and an optimized digital filter," in *1999 IEEE Ultrasonics Symposium. Proceedings. International Symposium (Cat. No. 99CH37027)*, 1999, vol. 2, pp. 1589–1593.

[99] M. I. Skolnik, *Introduction to Radar Systems*, 2nd ed. McGraw-Hill Book Company, 1981.

[100] M. Golay, "Complementary series," *IRE Transactions on Information Theory*, vol. 7, no. 2, pp. 82–87, 1961.

[101] P. Gong, P. Song, and S. Chen, "Ultrafast synthetic transmit aperture imaging using Hadamard-encoded virtual sources with overlapping sub-apertures," *IEEE transactions on medical imaging*, vol. 36, no. 6, pp. 1372–1381, 2017.

[102] E. Tiran, T. Deffieux, M. Correia, D. Maresca, B.-F. Osmanski, L.-A. Sieu, A. Bergel, I. Cohen, M. Pernot, and M. Tanter, "Multiplane wave imaging increases signal-to-noise ratio in ultrafast ultrasound imaging," *Physics in Medicine \& Biology*, vol. 60, no. 21, p. 8549, 2015.

[103] P. Gong, P. Song, and S. Chen, "Delay-encoded harmonic imaging (DE-HI) in multiplane-wave compounding," *IEEE transactions on medical imaging*, vol. 36, no. 4, pp. 952–959, 2016.

[104] R. Y. Chiao, L. J. Thomas, and S. D. Silverstein, "Sparse array imaging with spatially-encoded transmits," in *1997 IEEE Ultrasonics Symposium Proceedings. An International Symposium (Cat. No. 97CH36118)*, 1997, vol. 2, pp. 1679–1682.

[105] C. Ceroici, T. Harrison, and R. J. Zemp, "Fast orthogonal row-column electronic scanning with top-orthogonal-to-bottom electrode arrays," *IEEE transactions on ultrasonics, ferroelectrics, and frequency control*, vol. 64, no. 6, pp. 1009–1014, 2017.

[106] S. Satomura, "Ultrasonic Doppler method for the inspection of cardiac functions," *The Journal of the Acoustical Society of America*, vol. 29, no. 11, pp. 1181–1185, 1957.

[107] C. Kasai, K. Namekawa, A. Koyano, and R. Omoto, "Real-time two-dimensional blood flow imaging using an autocorrelation technique," *IEEE Transactions on sonics and ultrasonics*, vol. 32, no. 3, pp. 458–464, 1985.

[108] T. Loupas, R. Peterson, and R. W. Gill, "Experimental evaluation of velocity and power estimation for ultrasound blood flow imaging, by means of a two-dimensional autocorrelation approach," *IEEE transactions on ultrasonics, ferroelectrics, and frequency control*, vol. 42, no. 4, pp. 689–699, 1995.

[109] J. Bercoff, G. Montaldo, T. Loupas, D. Savery, F. Mézière, M. Fink, and M. Tanter, "Ultrafast compound Doppler imaging: Providing full blood flow characterization," *IEEE transactions on ultrasonics, ferroelectrics, and frequency control*, vol. 58, no. 1, pp. 134–147, 2011.

[110] K. K. Shung, G. Cloutier, and C. C. Lim, "The effects of hematocrit, shear rate, and turbulence on ultrasonic Doppler spectrum from blood," *IEEE transactions on biomedical engineering*, vol. 39, no. 5, pp. 462–469, 1992.

[111] C. Tysoe and D. H. Evans, "Bias in mean frequency estimation of Doppler signals due to wall clutter filters," *Ultrasound in medicine \& biology*, vol. 21, no. 5, pp. 671–677, 1995.

[112] C. Demené, T. Deffieux, M. Pernot, B.-F. Osmanski, V. Biran, J.-L. Gennisson, L.-A. Sieu, A. Bergel, S. Franqui, J.-M. Correas, and others, "Spatiotemporal clutter filtering of ultrafast ultrasound data highly increases Doppler and fUltrasound sensitivity," *IEEE transactions on medical imaging*, vol. 34, no. 11, pp. 2271–2285, 2015.

[113] M. Unekawa, M. Tomita, Y. Tomita, H. Toriumi, K. Miyaki, and N. Suzuki, "RBC velocities in single capillaries of mouse and rat brains are the same, despite 10-fold difference in body size," *Brain research*, vol. 1320, pp. 69–73, 2010.

[114] C. J. Pavlin, K. Harasiewicz, M. D. Sherar, and F. S. Foster, "Clinical use of ultrasound biomicroscopy," *Ophthalmology*, vol. 98, no. 3, pp. 287–295, 1991.

[115] D. J. Berkoff, L. E. Miller, and J. E. Block, "Clinical utility of ultrasound guidance for intra-articular knee injections: a review," *Clinical interventions in aging*, vol. 7, p. 89, 2012.

[116] K. Harasiewiczl, H. Kim, P. Babyn, K. Pritzker, and F. Foster, "Ultrasound backscatter microscopy of articular cartilage in vitro," in *1993 Proceedings IEEE Ultrasonics Symposium*, 1993, pp. 981–984.

[117] T. G. Landry, J. W. Rainsbury, R. B. Adamson, M. L. Bance, and J. A. Brown, "Real-time imaging of in-vitro human middle ear using high frequency ultrasound," *Hearing research*, vol. 326, pp. 1–7, 2015.

[118] J. A. Brown, Z. Torbatian, R. B. Adamson, R. Van Wijhe, R. J. Pennings, G. R. Lockwood, and M. L. Bance, "High-frequency ex vivo ultrasound imaging of the auditory system.," *Ultrasound Med Biol*, vol. 35, no. 11, pp. 1899–907, 2009.

[119] Z. Torbatian, R. Adamson, R. van Wijhe, R. Pennings, M. Bance, and J. Brown, "Imaging the auditory system: A new application of high-frequency ultrasound," in *2009 IEEE International Ultrasonics Symposium*, 2009, pp. 236–239.

[120] J.-M. Hyvelin, I. Tardy, C. Arbogast, M. Costa, P. Emmel, A. Helbert, M. Theraulaz, A. D. Nunn, and F. Tranquart, "Use of ultrasound contrast agent microbubbles in preclinical research: recommendations for small animal imaging," *Investigative radiology*, vol. 48, no. 8, pp. 570–583, 2013.

[121] L. A. Wirtzfeld, G. Wu, M. Bygrave, Y. Yamasaki, H. Sakai, M. Moussa, J. I. Izawa, D. B. Downey, N. M. Greenberg, A. Fenster, and others, "A new three-dimensional ultrasound microimaging technology for preclinical studies using a transgenic prostate cancer mouse model," *Cancer research*, vol. 65, no. 14, pp. 6337–6345, 2005.

[122] J. K. Willmann, R. H. Kimura, N. Deshpande, A. M. Lutz, J. R. Cochran, and S. S. Gambhir, "Targeted contrast-enhanced ultrasound imaging of tumor angiogenesis with contrast microbubbles conjugated to integrin-binding knottin peptides," *Journal of Nuclear Medicine*, vol. 51, no. 3, pp. 433–440, 2010.

[123] J. J. Rychak, J. Graba, A. M. Cheung, B. S. Mystry, J. R. Lindner, R. S. Kerbel, and F. S. Foster, "Microultrasound molecular imaging of vascular endothelial growth factor receptor 2 in a mouse model of tumor angiogenesis," *Molecular imaging*, vol. 6, no. 5, pp. 7290–2007, 2007.

[124] K. C. Graham, L. A. Wirtzfeld, L. T. MacKenzie, C. O. Postenka, A. C. Groom, I. C. MacDonald, A. Fenster, J. C. Lacefield, and A. F. Chambers, "Three-dimensional high-frequency ultrasound imaging for longitudinal evaluation of liver metastases in preclinical models," *Cancer Research*, vol. 65, no. 12, pp. 5231–5237, 2005.

[125] F. S. Foster, J. Mehi, M. Lukacs, D. Hirson, C. White, C. Chaggares, and A. Needles, "A new 15-50 MHz array-based micro-ultrasound scanner for preclinical imaging," *Ultrasound in medicine \& biology*, vol. 35, no. 10, pp. 1700–1708, 2009.

[126] F. S. Foster, J. Hossack, and S. L. Adamson, "Micro-ultrasound for preclinical imaging," *Interface focus*, vol. 1, no. 4, pp. 576–601, 2011.

[127] D. C. Levin and J. T. Fallon, "Significance of the angiographic morphology of localized coronary stenoses: histopathologic correlations.," *Circulation*, vol. 66, no. 2, pp. 316–320, 1982.

[128] S. G. Ellis, G. S. Roubin, S. B. King III, J. S. Douglas Jr, and W. R. Cox, "Importance of stenosis morphology in the estimation of restenosis risk after elective percutaneous transluminal coronary angioplasty," *The American journal of cardiology*, vol. 63, no. 1, pp. 30–34, 1989.

[129] M. W. Liu, G. Roubin, and S. King 3rd, "Restenosis after coronary angioplasty. Potential biologic determinants and role of intimal hyperplasia.," *Circulation*, vol.

79, no. 6, pp. 1374–1387, 1989.

[130] J. H. Chesebro, J. Y. Lam, L. Badimon, and V. Fuster, "Restenosis after arterial angioplasty: a hemorrheologic response to injury," *The American journal of cardiology*, vol. 60, no. 3, pp. 10–16, 1987.

[131] N. Sanghvi, A. Snoddy, S. Myers, K. Brandt, C. Reilly, and T. Franklin, "Characterization of normal and osteoarthritic cartilage using 25 MHz ultrasound," in *IEEE Symposium on Ultrasonics*, 1990, pp. 1413–1416.

[132] D. H. Turnbull, T. S. Bloomfield, H. S. Baldwin, F. S. Foster, and A. L. Joyner, "Ultrasound backscatter microscope analysis of early mouse embryonic brain development," *Proceedings of the National Academy of Sciences*, vol. 92, no. 6, pp. 2239–2243, 1995.

[133] M. Sherar and F. Foster, "The design and fabrication of high frequency poly (vinylidene fluoride) transducers," *Ultrasonic imaging*, vol. 11, no. 2, pp. 75–94, 1989.

[134] G. R. Lockwood, D. H. Turnbull, and F. S. Foster, "Fabrication of high frequency spherically shaped ceramic transducers," *IEEE transactions on ultrasonics, ferroelectrics, and frequency control*, vol. 41, no. 2, pp. 231–235, 1994.

[135] K. Snook, T. R. Shrout, and K. Shung, "Development of high frequency annular arrays for medical imaging," in *IEEE Symposium on Ultrasonics, 2003*, 2003, vol. 1, pp. 865–868.

[136] J. A. Brown, F. S. Foster, A. Needles, E. Cherin, and G. R. Lockwood, "Fabrication and performance of a 40-MHz linear array based on a 1-3 composite with geometric elevation focusing," *IEEE transactions on ultrasonics, ferroelectrics, and frequency control*, vol. 54, no. 9, pp. 1888–1894, 2007.

[137] M. Lukacs, J. Yin, G. Pang, R. Garcia, E. Cherin, R. Williams, F. S. Foster, and J. Mehi, "Performance and characterization of high frequency linear arrays," in *IEEE Ultrasonics Symposium, 2005.*, 2005, vol. 1, pp. 105–108.

[138] J. A. Brown and G. R. Lockwood, "A digital beamformer for high-frequency annular arrays.," *IEEE Trans Ultrason Ferroelectr Freq Control*, vol. 52, no. 8, pp. 1262–9, 2005.

[139] H. S. Lay and G. R. Lockwood, "A low cost receive beamformer for a high frequency annular array," in *2011 IEEE International Ultrasonics Symposium*, 2011, pp. 462–465.

[140] H. Lay and G. Lockwood, "2C-4 A 64-channel beamformer for 50 MHz linear arrays," in *Ultrasonics Symposium, 2007. IEEE*, 2007, pp. 29–32.

[141] P. Fusaroli, L. Ceroni, and G. Caletti, "Forward-view Endoscopic Ultrasound: A Systematic Review of Diagnostic and Therapeutic Applications.," *Endosc Ultrasound*, vol. 2, no. 2, pp. 64–70, 2013.

[142] J. Oertel, J. K. Krauss, and M. R. Gaab, "Ultrasonic aspiration in neuroendoscopy: first results with a new tool," 2008.

[143] B. D. Steinberg, "Digital beamforming in ultrasound.," *IEEE Trans Ultrason Ferroelectr Freq Control*, vol. 39, no. 6, pp. 716–21, 1992.

[144] M. G. Magrane, "Variable focusing in ultrasound imaging using non-uniform sampling," 1987.

[145] Y. C. Eldar and G. Kutyniok, *Compressed sensing: theory and applications*. Cambridge University Press, 2012.

[146] N. Wagner, Y. C. Eldar, and Z. Friedman, "Compressed beamforming in ultrasound imaging," *Signal Processing, IEEE Transactions on*, vol. 60, no. 9, pp. 4643–4657, 2012.

[147] T. Chernyakova and Y. C. Eldar, "Fourier domain beamforming: The path to compressed ultrasound imaging," *arXiv preprint arXiv:1307.6345*, 2013.

[148] J. Brown, J. Leadbetter, M. Leung, A. Bezanson, and R. Adamson, "A low cost open source high frame-rate high-frequency imaging system," in *2013 IEEE International Ultrasonics Symposium (IUS)*, 2013, pp. 549–552.

[149] L. K. Ryan and F. S. Foster, "Tissue equivalent vessel phantoms for intravascular ultrasound," *Ultrasound in medicine \& biology*, vol. 23, no. 2, pp. 261–273, 1997.

[150] T. Deffieux, J.-L. Gennisson, B. Larrat, M. Fink, and M. Tanter, "The variance of quantitative estimates in shear wave imaging: theory and experiments," *IEEE transactions on ultrasonics, ferroelectrics, and frequency control*, vol. 59, no. 11, pp. 2390–2410, 2012.

[151] J. Gennisson, J. Provost, T. Deffieux, C. Papadacci, M. Imbault, M. Pernot, and M. Tanter, "4-D ultrafast shear-wave imaging," *IEEE transactions on ultrasonics, ferroelectrics, and frequency control*, vol. 62, no. 6, pp. 1059–1065, 2015.

[152] G. R. Lockwood, J. R. Talman, and S. S. Brunke, "Real-time 3-D ultrasound imaging using sparse synthetic aperture beamforming," *IEEE transactions on ultrasonics, ferroelectrics, and frequency control*, vol. 45, no. 4, pp. 980–988,

1998.

[153] J. Liu and J. Luo, "Compressed sensing based synthetic transmit aperture for phased array using Hadamard encoded diverging wave transmissions," *IEEE transactions on ultrasonics, ferroelectrics, and frequency control*, vol. 65, no. 7, pp. 1141–1152, 2018.

[154] T. Harrison, A. Sampaleanu, and R. J. Zemp, "S-sequence spatially-encoded synthetic aperture ultrasound imaging [correspondence]," *IEEE transactions on ultrasonics, ferroelectrics, and frequency control*, vol. 61, no. 5, pp. 886–890, 2014.

[155] J. Liu, Q. He, and J. Luo, "A compressed sensing strategy for synthetic transmit aperture ultrasound imaging," *IEEE transactions on medical imaging*, vol. 36, no. 4, pp. 878–891, 2016.

[156] L. Tong, A. Ramalli, R. Jasaityte, P. Tortoli, and J. D'hooge, "Multi-transmit beam forming for fast cardiac imaging—Experimental validation and in vivo application," *IEEE transactions on medical imaging*, vol. 33, no. 6, pp. 1205–1219, 2014.

[157] A. Rodriguez-Molares, J. Avdal, H. Torp, and L. Løvstakken, "Axial lobes in coherent plane-wave compounding," in *2016 IEEE International Ultrasonics Symposium (IUS)*, 2016, pp. 1–4.

[158] S. Nikolov and J. A. Jensen, "Comparison between different encoding schemes for synthetic aperture imaging," in *Medical Imaging 2002: Ultrasonic Imaging and Signal Processing*, 2002, vol. 4687, pp. 1–12.

[159] T. Deffieux, G. Montaldo, M. Tanter, and M. Fink, "Shear wave spectroscopy for in vivo quantification of human soft tissues visco-elasticity," *IEEE transactions on medical imaging*, vol. 28, no. 3, pp. 313–322, 2008.

[160] M. S. Berger, J. Kincaid, G. A. Ojemann, and E. Lettich, "Brain mapping techniques to maximize resection, safety, and seizure control in children with brain tumors.," *Neurosurgery*, vol. 25, no. 5, pp. 786–92, 1989.

[161] J. Roland, P. Brunner, J. Johnston, G. Schalk, and E. C. Leuthardt, "Passive real-time identification of speech and motor cortex during an awake craniotomy.," *Epilepsy Behav*, vol. 18, no. 1–2, pp. 123–8, 2010.

[162] M. Genetti, R. Tyrand, F. Grouiller, A. M. Lascano, S. Vulliemoz, L. Spinelli, M. Seeck, K. Schaller, and C. Michel, "Comparison of high gamma electrocorticography and fMRI with electrocortical stimulation for localization of somatosensory and language cortex," *Clinical Neurophysiology*, vol. 126, no. 1,

pp. 121–130, 2015.

[163] S. Y. Bookheimer, T. A. Zeffiro, T. Blaxton, B. A. Malow, W. D. Gaillard, S. Sato, C. Kufta, P. Fedio, and W. H. Theodore, "A direct comparison of PET activation and electrocortical stimulation mapping for language localization.," *Neurology*, vol. 48, no. 4, pp. 1056–65, 1997.

[164] S. Ille, N. Sollmann, T. Hauck, S. Maurer, N. Tanigawa, T. Obermueller, C. Negwer, D. Droese, C. Zimmer, B. Meyer, and others, "Combined noninvasive language mapping by navigated transcranial magnetic stimulation and functional MRI and its comparison with direct cortical stimulation," *Journal of neurosurgery*, vol. 123, no. 1, pp. 212–225, 2015.

[165] E. F. Chang, A. Clark, J. S. Smith, M.-Y. Polley, S. M. Chang, N. M. Barbaro, A. T. Parsa, M. W. McDermott, and M. S. Berger, "Functional mapping-guided resection of low-grade gliomas in eloquent areas of the brain: improvement of long-term survival," *Journal of neurosurgery*, vol. 114, no. 3, pp. 566–573, 2011.

[166] F. Roser and M. Liebsch, "Closer to the Edge-The Value of Intraoperative Brain Mapping.," *World neurosurgery*, vol. 89, pp. 689–691, 2016.

[167] D. Zumofen, L. Regli, M. Levivier, and N. Krayenbühl, "Chronic subdural hematomas treated by burr hole trepanation and a subperiostal drainage system," *Neurosurgery*, vol. 64, no. 6, pp. 1116–1122, 2009.

[168] L. Auer, P. Holzer, P. Ascher, and F. Heppner, "Endoscopic neurosurgery," *Acta neurochirurgica*, vol. 90, no. 1–2, pp. 1–14, 1988.

[169] H. E. Heffner, R. S. Heffner, C. Contos, and T. Ott, "Audiogram of the hooded Norway rat," *Hearing research*, vol. 73, no. 2, pp. 244–248, 1994.

[170] T. Deffieux, C. Demene, M. Pernot, and M. Tanter, "Functional ultrasound neuroimaging: a review of the preclinical and clinical state of the art," *Current opinion in neurobiology*, vol. 50, pp. 128–135, 2018.

[171] C. R. Hazard and G. R. Lockwood, "Theoretical assessment of a synthetic aperture beamformer for real-time 3-D imaging.," *IEEE Trans Ultrason Ferroelectr Freq Control*, vol. 46, no. 4, pp. 972–80, 1999.

[172] M. F. Rasmussen and J. A. Jensen, "Comparison of 3-D synthetic aperture phased-array ultrasound imaging and parallel beamforming," *IEEE transactions on ultrasonics, ferroelectrics, and frequency control*, vol. 61, no. 10, pp. 1638–1650, 2014.

[173] J. A. Jensen, H. Holten-Lund, R. T. Nilsson, M. Hansen, U. D. Larsen, R. P. Domsten, B. G. Tomov, M. B. Stuart, S. I. Nikolov, M. J. Pihl, Y. Du, J. H.

Rasmussen, and M. F. Rasmussen, "SARUS: A Synthetic Aperture Real-time Ultrasound System.," *IEEE Trans Ultrason Ferroelectr Freq Control*, vol. 60, no. 9, pp. 1838–52, 2013.

[174] C. Ceroici, K. Latham, B. A. Greenlay, J. A. Brown, and R. J. Zemp, "Fast Orthogonal Row-Column Electronic Scanning Experiments and Comparisons," *IEEE Transactions on Ultrasonics, Ferroelectrics, and Frequency Control*, vol. 66, no. 6, pp. 1093–1101, 2019.

[175] G. Paxinos and C. Watson, *The rat brain in stereotaxic coordinates: hard cover edition*. Elsevier, 2006.

[176] P. Van Dongen, "Brain size in vertebrates," in *The central nervous system of vertebrates*, Springer, 1998, pp. 2099–2134.

[177] S. M. Blinkov, *The human brain in figures and tables: a quantitative handbook*.

[178] S. Low, Y. Ng, T. Yeo, and N. Chou, "Use of OsteoplugTM polycaprolactone implants as novel burr-hole covers," *Singapore Med J*, vol. 50, no. 8, pp. 777–780, 2009.

[179] J.-T. Schantz, T.-C. Lim, C. Ning, S. H. Teoh, K. C. Tan, S. C. Wang, and D. W. Hutmacher, "Cranioplasty after trephination using a novel biodegradable burr hole cover: technical case report.," *Neurosurgery*, vol. 58, no. 1 Suppl, p. ONS–E176; discussion ONS–E176, 2006.

APPENDIX A Copyright Permission Letters

A Sub-Nyquist, Variable Sampling, High-Frequency Phased Array Beamformer

IEEE
Requesting permission to reuse content from an IEEE publication

Author: Christopher A. Samson
Publication: Ultrasonics, Ferroelectrics and Frequency Control, IEEE Transactions on
Publisher: IEEE
Date: March 2017

Copyright © 2017, IEEE

Thesis / Dissertation Reuse

The IEEE does not require individuals working on a thesis to obtain a formal reuse license, however, you may print out this statement to be used as a permission grant:

Requirements to be followed when using any portion (e.g., figure, graph, table, or textual material) of an IEEE copyrighted paper in a thesis:

1) In the case of textual material (e.g., using short quotes or referring to the work within these papers) users must give full credit to the original source (author, paper, publication) followed by the IEEE copyright line © 2011 IEEE.
2) In the case of illustrations or tabular material, we require that the copyright line © [Year of original publication] IEEE appear prominently with each reprinted figure and/or table.
3) If a substantial portion of the original paper is to be used, and if you are not the senior author, also obtain the senior author's approval.

Requirements to be followed when using an entire IEEE copyrighted paper in a thesis:

1) The following IEEE copyright/ credit notice should be placed prominently in the references: © [year of original publication] IEEE. Reprinted, with permission, from [author names, paper title, IEEE publication title, and month/year of publication]
2) Only the accepted version of an IEEE copyrighted paper can be used when posting the paper or your thesis on-line.
3) In placing the thesis on the author's university website, please display the following message in a prominent place on the website: In reference to IEEE copyrighted material which is used with permission in this thesis, the IEEE does not endorse any of [university/educational entity's name goes here]'s products or services. Internal or personal use of this material is permitted. If interested in reprinting/republishing IEEE copyrighted material for advertising or promotional purposes or for creating new collective works for resale or redistribution, please go to http://www.ieee.org/publications_standards/publications/rights/rights_link.html to learn how to obtain a License from RightsLink.

If applicable, University Microfilms and/or ProQuest Library, or the Archives of Canada may supply single copies of the dissertation.

BACK   CLOSE WINDOW

Ultrafast Phased Array Imaging using Sparse Orthogonal Diverging Waves

Author: Christopher Samson

Publication: Ultrasonics, Ferroelectrics and Frequency Control, IEEE Transactions on

Publisher: IEEE

Date: Dec 31, 1969

Copyright © 1969, IEEE

IEEE Requesting permission to reuse content from an IEEE publication

Thesis / Dissertation Reuse

The IEEE does not require individuals working on a thesis to obtain a formal reuse license, however, you may print out this statement to be used as a permission grant:

Requirements to be followed when using any portion (e.g., figure, graph, table, or textual material) of an IEEE copyrighted paper in a thesis:

1) In the case of textual material (e.g., using short quotes or referring to the work within these papers) users must give full credit to the original source (author, paper, publication) followed by the IEEE copyright line © 2011 IEEE.
2) In the case of illustrations or tabular material, we require that the copyright line © [Year of original publication] IEEE appear prominently with each reprinted figure and/or table.
3) If a substantial portion of the original paper is to be used, and if you are not the senior author, also obtain the senior author's approval.

Requirements to be followed when using an entire IEEE copyrighted paper in a thesis:

1) The following IEEE copyright/ credit notice should be placed prominently in the references: © [year of original publication] IEEE. Reprinted, with permission, from [author names, paper title, IEEE publication title, and month/year of publication]
2) Only the accepted version of an IEEE copyrighted paper can be used when posting the paper or your thesis on-line.
3) In placing the thesis on the author's university website, please display the following message in a prominent place on the website: In reference to IEEE copyrighted material which is used with permission in this thesis, the IEEE does not endorse any of [university/educational entity's name goes here]'s products or services. Internal or personal use of this material is permitted. If interested in reprinting/republishing IEEE copyrighted material for advertising or promotional purposes or for creating new collective works for resale or redistribution, please go to http://www.ieee.org/publications_standards/publications/rights/rights_link.html to learn how to obtain a License from RightsLink.

If applicable, University Microfilms and/or ProQuest Library, or the Archives of Canada may supply single copies of the dissertation.

BACK   CLOSE WINDOW

IEEE

Requesting permission to reuse content from an IEEE publication

Minimally Invasive InVivo Functional Ultrasound Imaging Using a 40 MHz Phased Array Endoscope: Mapping the Auditory Response in Rats

Conference Proceedings: 2019 IEEE International Ultrasonics Symposium (IUS)
Author: Christopher Samson
Publisher: IEEE
Date: Oct. 2019

Copyright © 2019, IEEE

BACK   CLOSE WINDOW